Tese de Doutorado

Supervised Machine Learning Framework for the Analysis of Contacting Solids Under Inelastic Strains

Paulo Guilherme Marques Flávio

Brasília, Março de 2023

UNIVERSIDADE DE BRASÍLIA

FACULDADE DE TECNOLOGIA

UNIVERSIDADE DE BRASÍLIA
Faculdade de Tecnologia

Tese de Doutorado

Supervised Machine Learning Framework for the Analysis of Contacting Solids Under Inelastic Strains

Paulo Guilherme Marques Flávio

Relatório submetido ao Departamento de Engenharia Mecânica da Faculdade de Tecnologia da Universidade de Brasília como requisito parcial para obtenção do grau de Doutor em Ciências Mecânicas

Banca Examinadora

Prof. Dr. Thiago Doca, ENM/UnB
Orientador

Prof. Dr. Eder L. de Albuquerque, ENM/UnB
Examinador interno

Prof. Dr. Raimundo C. S. F. Júnior, PPGEM/UFRN
Examinador externo

Prof. Dr. Marcelo Greco, DEES/UFMG
Examinador externo

FICHA CATALOGRÁFICA

MARQUES FLÁVIO, PAULO GUILHERME

Supervised Machine Learning Framework for the Analysis of Contacting Solids Under Inelastic Strains

[Distrito Federal] 2023.

xii, NP., 210 x 297 mm (ENM/FT/UnB, Doutor, Ciências Mecânicas, 2023).

Tese de Doutorado - Universidade de Brasília. Faculdade de Tecnologia.

Departamento de Engenharia Mecánica.

1. Artificial Neural Network	2. Finite Element
3. Elastic-viscoplastic Model	4. Indentation
I. ENM/FT/UnB	

BIBLIOGRAPHY

MARQUES FLÁVIO, P. G. (2023). Supervised Machine Learning Framework for the Analysis of Contacting Solids Under Inelastic Strains , Tese de Doutorado em Ciências Mecânicas, Publicação ENM.DM-71A/14, Departamento de Engenharia Mecânica, Faculdade de Tecnologia, Universidade de Brasília, Brasília, DF, NP.

CESSÃO DE DIREITOS

AUTOR: Paulo Guilherme Marques Flávio

TÍTULO: Supervised Machine Learning Framework for the Analysis of Contacting Solids Under Inelastic Strains .

GRAU: Doutor   ANO: 2023

_____

Paulo Guilherme Marques Flávio

Brasília - DF - Brasil

ABSTRACT

Artificial Neural Networks (ANN) can be understood as a complex computing system made up of a series of interconnected processing elements inspired by the Biological Neural Networks that have the purpose of processing information aiming to generate a response. This study aims to combine the capabilities of ANN's, developed using a supervised learning algorithm for predicting the mechanical behavior and material properties of the respective rheological models adopted for metallic and polymeric materials. The evaluation of the polymers is restricted to thermoplastic polymers and a elastic-viscoplastic model based on the Mulliken-Boyce constitutive model is adopted. The implementation of the model is carried out via VUMAT subroutines (explicit integration) in the commercial software ABAQUS for the study of uniaxial compression in large deformations. The desired predictions for the study of the evaluated polymers are: (1) Prediction of the material parameters of the modified constitutive model of Mulliken-Boyce implemented from the experimental stress-strain curve and (2) prediction of the stress-strain curve from the material parameters. The study of metals is based on indentation tests at large deformations. Ludwik equation is adopted for the description of the mechanical behavior and is implemented via implicit integration in the same commercial software. The desired predictions for metals are: (1) prediction of the stress-strain curve from the displacement-force curve obtained through indentation test and (2) prediction of the displacement-force curve, residual indentation, and contact pressure from the main mechanical properties of metals. All predictions are performed through the implementation of deep neural networks and supervised training. The results achieved are satisfactory, the performance of the predictions made for all evaluated cases show good accuracy with a significant reduction in processing time compared to implementations via Finite Element.

Artificial Neural Network, Finite Element, Elastic-viscoplastic Model, Mulliken-Boyce, Indentation.

RESUMO

As Redes Neurais Artificiais (RNA) podem ser entendidas como um sistema computacional complexo formado por uma série de elementos de processamento interconectados inspirados nas Redes Neurais Biológicas, que têm como finalidade o processamento de informações com o objetivo de gerar uma resposta. Este estudo visa combinar as capacidades de RNA's e Elementos Finitos, desenvolvida por meio de algoritmos de aprendizado supervisionado para prever o comportamento mecânico e as propriedades materiais através de modelos constitutivos para metais e polímeros. A avaliação dos polímeros restringe-se a polímeros termoplásticos e adota-se um modelo elasto-viscoplástico baseado no modelo constitutivo de Mulliken-Boyce. A implementação do modelo é realizada via sub-rotinas VU-MAT (integração explícita) no software comercial ABAQUS® para o estudo de compressão uniaxial em grandes deformações. As previsões desejadas para o estudo dos polímeros avaliados são: (1) Previsão dos parâmetros materiais do modelo constitutivo modificado de Mulliken-Boyce implementado, a partir da curva tensão-deformação experimental e (2) previsão da curva tensão-deformação a partir das propriedades do material. O estudo dos metais é baseado em testes de indentação em grandes deformações. A equação de Ludwik é adotada para a descrição do comportamento mecânico e é implementada via integração implícita no mesmo software comercial. As predições almejadas para os metais são: (1) predição da curva tensão-deformação a partir da curva deslocamento-força obtida através do teste de indentação e (2) predição da curva deslocamento-força, indentação residual e pressão de contato a partir das principais propriedades mecânicas de metais. Todas as previsões são realizadas através da implementação de redes neurais via treinamento supervisionado. O desempenho das previsões feitas para todos os casos avaliados mostra boa acurácia com uma redução significativa no tempo de processamento em comparação com implementações via Elemento Finito.

Rede Neural Artificial, Elementos Finitos, Modelo elasto-viscoplástico, Mulliken-Boyce, Indentação.

:

Table of Contents

List of Figures

List of Tables

List of Symbols

$\boldsymbol{F}$	Gradient Tensor
$\boldsymbol{F}^p$	Plastic gradient Tensor
$\boldsymbol{R}$	Rigid body rotation tensor
$\boldsymbol{I}$	Identity tensor
$\boldsymbol{C}$	Right Cauchy-Green deformation tensor
$\boldsymbol{B}$	Left Cauchy-Green deformation tensor
$\boldsymbol{B}^e$	Elastic left Cauchy-Green deformation tensor
$\boldsymbol{B}^p$	Plastic left Cauchy-Green deformation tensor
$\boldsymbol{U}$	Left Cauchy-Green deformation tensor
$\boldsymbol{L}$	Velocity gradient
$\boldsymbol{L}^e$	Elastic velocity gradient
$\boldsymbol{L}^p$	Plastic velocity gradient
$\boldsymbol{W}$	Asymmetric tensor
$\boldsymbol{D}$	Strain rate tensor
$\boldsymbol{W}$	Rotation rate tensor
$\boldsymbol{D}^p$	Plastic strain rate tensor
$\boldsymbol{W}^p$	Plastic rotation rate tensor
$\boldsymbol{V}$	Stretch tensor in spatial configuration
$\boldsymbol{\epsilon}$	Infinitesimal strain tensor
$\boldsymbol{\epsilon}^e$	Elastic infinitesimal strain tensor
$\boldsymbol{\epsilon}^p$	Plastic infinitesimal strain tensor
$\boldsymbol{T}$	Kirchhoff tensor
$\boldsymbol{T}^e$	Elastic Kirchhoff tensor
$\boldsymbol{T}^p$	Plastic Kirchhoff tensor
$\boldsymbol{T}_b$	Backstress tensor
$\boldsymbol{T}^{vp}$	Viscoplastic Kirchhoff tensor
$\boldsymbol{E}$	Strain tensor
F	Force
F_s	Static friction force
F_R	Reaction force

F_N	Normal force
μ_S	Coefficient of static friction
μ_K	Coefficient of dynamic friction
F_a	Contribution of friction
τ	Shear Stress
δ	Penetration
u	Displacement
E	Young's modulus
E^*	Equivalent Young's modulus
ν	Poisson's ratio
k	bulk modulus
p_0	Maximum Hertz pressure
p_m	Average pressure
σ	Normal stress
$\vec{X}$	Position - Langrangean representation
$\vec{x}$	Position - Eulerian representation
$\vec{v}$	Velocity
$\vec{a}$	Acceleration
Λ	Lamé's elastic constant
G	Coulomb shear modulus of elasticity
μ^e	Elastic shear modulus
tr	Trace
W^e	Elastic energy
J	Jacobian
E_α	Young's modulus - alpha chain
E_β	Young's modulus - beta chain
ν	Poisson's ratio
$\dot{\gamma}_{0,\alpha}^p$	Pre-exponential factor - alpha chain
$\dot{\gamma}_{0,\beta}^p$	Pre-exponential factor - beta chain
$\alpha_{p,\alpha}$	Pressure coefficient - alpha chain
$\alpha_{p,\beta}$	Pressure coefficient - beta chain
ΔG_α	Activation energy - alpha chain
ΔG_β	Activation energy - beta chain
h_α	Softening slope - alpha chain
h_β	Softening slope - beta chain
s_{ss}	Preferred states of athermal shear strengths
C_r	Rubbery modulus
N	Limiting chain extensibility
K	Boltzmann Constant

Θ	Temperature
J_m	Dimensionless Parameter - Gent Model
M_i	Equivalent shear modulus
t	Time
V	Volume
$\vec{c}$	Rigid translation displacement
K	Strength coefficient
n	Hardening exponent
W	Weight matrix
b	bias term
ϕ_a	Activation function

Chapter 1

Introduction

1.1 Contextualization

Artificial neural networks (ANN) are being used in a variety of daily and industrial activities, including social engineering for bespoke advertising, disease and research, logistical improvement of transportation systems and the optimization of manufacturing processes. According to Zhong et al. [2021], its primary purpose is to simplify and hasten the characterization of complicated events found in a variety of scientific domains.

Studies employing Machine Learning (ML) strategies to evaluate mechanical behavior of materials are widely available. The determination of the stress-strain relationship, for instance, is one of the most important pieces of information when defining the mechanical behavior of engineering materials. To generate a complete stress-strain curve, a significant variety of conventional techniques such as tensile, compression, torsional, and flexural tests are required. Nevertheless, indentations tests are presented as a common alternative used to characterize the mechanical properties of materials, being used for both metallic and polymeric materials. In general, the main source of information for the inference of elastic and plastic properties comes from the behavior of the displacement-force curve.

Metallic materials are inorganic substances, preferably used as a composition of different elements in order to form an alloy, instead of being used in its pure form. Such materials are composed of metallic substances, such as: iron and aluminum, but also by small amounts of non-metallic such as: carbon, oxygen, and nitrogen. Regarding its mechanical properties, the microstructure of the metallic material, properties of the elements that compose it, and manufacturing process have a strong influence. Concerning its use, metallic materials are important to compose parts and structures due to their excellent mechanical properties (strength, for example), as well as their good formability. In general, steels represent approximately 80 % of all metallic materials used in different types of applications.

Polymers present themselves as a viable alternative for the replacement of parts or components that were formerly made up solely of metallic or ceramic materials, either by cost reduction, mechanical characteristics, or other properties intrinsic to the project or the material. Technological advancement in conjunction with the evolution of materials engineering has enabled polymers of greater strength, lower density, and lower cost to be obtained.

According to Canevarolo [2010], the mechanical properties of polymers can be defined from the response of this material under the application of external efforts. The nature of this response depends on several factors intrinsic to the polymer manufacturing process, such as: temperature, processing time and conditions, polymerization process controls, among others. Not least, the test conditions also have a great influence on the response of the material, such as: test temperature, loading/unloading and strain rate.

Unlike most metals, polymers have explicitly different characteristics between tensile and compression. In general, they usually have a fragile behavior in traction and ductile under compression. Such difference is due to the compression in polymers causing the reduction in the size of internal defects, such as microcracks, arising from the material manufacturing process that are accentuated in the tensile tests. Another important aspect that contributes to the compression behavior of polymers is crystallinity. According to Mccrum et al. [1988], amorphous polymers have a clearer yielding point, whereas semicrystalline polymers do not explicitly show such threshold.

The numerical study of the behavior of polymers represents an important branch of the study of computational methods in engineering materials, as well as an important alternative to experimental tests that, in certain circumstances, can be destructive and/or require too much time to achieve the desired result. Unlike metals, for which most commercial software has several libraries and models implemented to describe the behavior of either linear, plastic or viscoplastic, there are few models implemented for elastic-viscoplastic evaluations in polymers, among the software commonly used, the presence of models for these materials in most cases covers no more than the hyperelastic behavior.

In parallel to the growing use of polymers for the most diverse purposes, there has also been advancement in numerical methods capable of predicting the mechanical behavior of these materials since the methods applicable to metals are unable to represent their behavior in a striking way. However, it should be noted that because polymeric materials have a greater diversity of mechanical behavior, commonly each numerical method is valid for a restricted range of polymers. Among the various numerical methods present in the bibliography, the following models can be cited: 8 chain Arruda and Boyce [1993], Ogden [1985], Extended Tube Model Kaliske and Heinrich [1999], Suchocki [2015], Bergstrom and Boyce [1998], Arruda-Boyce Boyce et al. [1994], Hybrid Bergstrom et al. [2003] e Mulliken and Boyce [2006].

The relevance of defining the mechanical characteristics of materials is crucial. The employment of computational approaches in conjunction with Machine Learning presents itself as a feasible alternative for this goal, in addition to providing computational cost reductions of simulations in a finite element environment.

1.2 State-of-the-Art

In this section the reader will be able to find about the state-of-the art of the most relevant topics for the development of this work, they are: (1) characterization of the mechanical behavior of solids, presenting primarily about uniaxial compression and indentation test, (2) rheological models adopted for the mechanical characterization of the elastic-viscoplastic behavior of thermoplastic polymers, (3) numerical implementations of indentation test with the presence of permanent deformations, and (4) application of neural networks for the prediction of mechanical behaviors of materials under different boundary conditions.

1.2.1 Mechanical Characterization of Solids and Experimental Indentation Test

The characterization of material behavior is extremely important for the correct description of its mechanical behavior, which is required for a faithful description using numerical methods. The tensile test is one of the main experiments used to verify the material's behavior and from this test the stress-strain curve can be generated. Several material-related properties, such as Young's modulus, yield strength, and ultimate tensile strength, can be defined using such a curve.

Metals' behavior in both traction and compression is generally similar when evaluating their behavior. However, when the behavior of polymers is evaluated from two perspectives: compression and traction, very different behaviors can be observed. As a result, compression tests are required to evaluate the behavior of polymers from this standpoint.

The compression test involves compressing a specimen, which is usually cylindrical, between two parallel flat surfaces. In this manner, a controlled displacement is applied to one of the surfaces in order to maintain a constant strain rate. The ASTM E9-19 standard, which aims to standardize experimental compression testing procedures, describes the procedures for performing compression on metals at room temperature, including the qualification of the test equipment, dimensions, and specimen preparation, as well as the experimental procedures to be performed. In terms of polymers, the ASTM D695-15 standard describes a test method for compressing rigid plastics, which can also be used to evaluate

composites with rigid polymers as matrix. In addition to the polymeric material's stress-strain curve, the following properties can be determined: Young's modulus, yield stress, deformations beyond the yield stress, and compressive strength.

Because polymers are highly dependent on external factors, ambient conditions can influence their behavior, necessitating the standardization of specimen conditioning and storage. As a result, supplementary standards are used to avoid exposing these materials to degenerative environments such as high temperature, UV light, and humidity, as well as establishing time intervals between specimen manufacture and testing.

The indentation test is another common method for characterizing material properties. According to George and Mohammadreza [2020], indentation testing is a technique widely used to probe the mechanical properties of solid state materials, such as hardness and elastic stiffness, by measuring their surface response to penetration of a probe with known geometry and imposed load. The resistance of a material to local plastic deformation is defined as hardness. The most commonly used hardness tests, according to Smith [2007], are defined by the shape of the indent, the size, and the load. It should be noted that the indentation tests are usually used to describe other elastic and plastic properties of the materials, mainly through the force-displacement curve. Some works presented in the section 1.2.2 demonstrate its use for this purpose.

The main relevant standards to the indentation tests specified above are: (1) ASTM E10-00, which presents the methodology to be adopted for the Brinell hardness of metallic materials test, and (2) ASTM D785-03, which establishes the specified standard method for Rockwell hardness of plastics.

1.2.2 Numerical Constitutive Modeling of Polymers

Several studies discuss the use of computational methods to evaluate the mechanical behavior of polymers. Such methods must be able to effectively represent their dependence on several factors, including strain rate and temperature. Furthermore, it should be emphasized that each numerical model for evaluating polymers is often suitable to a limited range of polymers with similar mechanical properties. This, along with advancements in obtaining new polymers with different behaviors, is one of the reasons why the study of elastic-viscoplastic models is recurring as a research object.

Among the existing models, Perzyna [1966] presents one of the first viscoplastic models that, although more applicable to metals, is also found in the literature for the study of polymers. Such a model is characterized by the replacement of the Lagrange multiplier method by the Penalty method, in order to impose the plasticization criterion. Jeong and Anastasia [2009], for example, apply the referred model for the study of high density polyethylenes under compression in small deformations (1%). Even if in a smaller amount,

there are also numerical studies that use the Perzyna [1966] model for the evaluation of polymers in large deformations, for example, the study of Nguyen et al. [2016], where the author presents an elastic-viscoplastic constitutive damage model for amorphous polymers, applied more specifically to an RTM 6 epoxy resin. Some other studies that use the Perzyna [1966] model are: Belayachi et al. [2008], Al-Rub and Tehrani [2011] , Al-Rub et al. [2014] and Belayachi et al. [2008].

One of the first works on the numerical study of polymers was presented by Arruda and Boyce [1993] and titled by *A Three-dimensional constitutive model for the large stretch behavior of rubber elastic materials.* Such an article can be considered as the basis for the Arruda-Boyce model. It presents a model of hyperelasticity for a material said to be incompressible from the consideration of a molecular structure of eight chains. Later on, Boyce et al. [1994] presented studies of numerical models in large deformations for crystalline polymers, more specifically the PC and PPMA (polymethylmethacrylate). The works presented by Boyce et al. [1994] are shown as a major advance for the study of polymers and are widely used until today, in addition to serving as the basis for several other models obtained later.

In view of the points presented, there are several works that propose modifications or use exciting numerical methods for the evaluation of polymers under different conditions. These works aid in the identification of numerical models pertinent to the type of study and material evaluated. Among the most relevant, there is the study conducted by Antoine and Batra [2014], where they implement the numerical model of Arruda-Boyce with some modifications, such as the use of an incompressible viscoelastic model from Ogden [1985], instead of an eight-chain model. Such a model is used in a three-dimensional study of ballistics at low speeds, where the object subjected to the impact consists of interleaved blades of PMMA and PC. Similarly, Torres and Frontini [2016] carry out a numerical-experimental comparative study of the deformation and failure behavior of the PC under impact at low speeds. To do so, the authors applied the numerical model of Arruda-Boyce with modifications in a VUMAT environment, in order to reproduce the thermomechanical behavior and dependence on the material deformation rate. In the model adopted by the authors, there are changes in the term referring to the plastic deformation rate, where the model is considered dependent on the resistance parameters and shear flow exponent, as well as on a softening term after the occurrence of viscoplastic flow.

Some other pertinent works that use the Arruda Boyce model or this model with modifications can be found at: Polanco-Loria et al. [2010]; Tomas et al. [2008]; Kermouche et al. [2013]; Tomas et al. [2015] e Johnsen et al. [2019].

As previously stated, the Arruda-Boyce model served as the foundation for several other commonly used models, such as the Mulliken Boyce model, which was first presented in 2002 and updated in 2006. This model presents itself as an advance to the Arruda-Boyce model,

mainly due to the addition of a second viscoplastic network. In this model, some changes in the calculation of the viscoplastic flow rate are adopted and can be better understood later in this thesis. An overview of the Mulliken-Boyce model can be found in the paper presented by Mulliken and Boyce [2006] entitled: *Mechanics of the rate-dependent elastic-plastic deformation of glassy polymers from low to high strain rates*, where the model is applied to describe the behavior of PC and PPMA.

The use of the Mulliken-Boyce model can also be found in several areas of research, such as the work conducted by Wang et al. [2017], in which the authors combine this model with the models presented by G'Sell and Jonas [1981] and DSGZ Duan et al. [2001] for the description of the mechanical behavior of the PC at strain rates of 10^{-4} to $5000 \ s^{-1}$ through the implementation of VUMAT's subroutines in the ABAQUS®/Explicit commercial software. The results presented by the authors show a good adequacy of the model to describe the mechanical behavior of the material. The best match between the results obtained numerically and experimentally was by imposing a deformation rate of $10^{-3} \ s^{-1}$, where the error of 0.58%. The biggest divergence between the data was related to a strain rate of $10 \ s^{-1}$, where the error was 13.08%.

Varghese and Batra [2009] presented a constitutive model based on the Mulliken-Boyce model for the numerical representation of the mechanical behavior of PC and PPMA at high strain rates. In the presented study they point out that the proposed modifications: an elasticity module dependent only on the temperature history and the effective strain rate, as well as the introduction of two internal variables in the representation of the two intermolecular contribution networks for a better characterization of the stress softening for high deformation rates, lead to a better adaptation of the numerical model for the simulations conducted. Based on the results, the authors' proposed model is better suited for high deformation rates, such as $770 \ s^{-1}$ for the study of PPMA. However, the observed results indicate a poor suitability for simulations with moderate or low strain rates. In these circumstances, the original Mulliken-Boyce model is clearly more suitable.

As much as the Mulliken-Boyce model was developed to describe the behavior of thermoplastic polymers, its use is also found for the description of thermoset polymers, as is the case of the work presented by Jordan et al. [2008], where they apply a one-dimensional model for the evaluation of an EPON 826 Epoxy resin with a cure by diethanolamine (DEA) at different strain rates (between 10^{-3} to $10^4 \ s^{-1}$). Because the mechanical behavior of the resin used in the studies shows similarity to PC, the authors identified that the Mulliken-Boyce model presents itself as a viable alternative. A comparison between the experimental and numerical results shows a good suitability for all investigated cases. Because Epoxy 826 resin presents a similar behavior for both low and high deformation rates, the Mulliken Boyce model has a better fit than the model presented by Varghese and Batra [2009], for example. The modifications presented by this last model are more applicable to materials

that present a relevant yield characteristic after the elastic zone in simulations of high deformation rates, as is the case of PC and not of EPON 826 resin. As presented in PC and PPMA simulations from studies conducted by Mulliken and Boyce [2006], as the deformation rate increases, or even for materials that have different characteristics, the model has greater difficulty to represent the zone after the region of linear elasticity, more precisely when the tangent module of the curve begins to vary. This adjustment difficulty may extend until the maximum stress peak before the predominance of the nonlinear hardening region. Some possible alternatives for a better adaptation are neither a numerical extension of the zone said to be linear or changes in the tangent module, circumstances that must be weighed by the objectives of the study.

Wang et al. [2018] deals with existing numerical models and proposes new constitutive equations for the evaluation of thermoplastic polymers, using four different numerical models to evaluate the mechanical behavior of PC and ABS, including the original Mulliken-Boyce model and a modified one. As in the studies previously presented, Wang et al. [2018] performs several simulations of low to high deformation rates. The main conclusions show that the Mulliken-Boyce model was adequate to reproduce the behavior of materials in almost all simulations conducted, except for those with high strain rates, as also presented by Varghese and Batra [2009]. It is noteworthy that the model proposed by the authors, called as Wang model, showed good suitability for all simulations, which makes it a viable alternative for PC and ABS simulations, especially for cases of very high strain rate applied, as the model presents a good prediction for strain rates up to $5,000 \ s^{-1}$. Wang's model presents relative simplicity of implementation, the stress is made up of two contribution networks, the first of which reproduces the contribution of low and medium strain rates and the second reproduces the contribution of high strain rates.

The Mulliken-Boyce model was also used in other relevant works: (1) Trivedi and Siviour [2018] apply a modified model for the mechanical evaluation of the behavior of Polyvinyl Chloride (PVC) under different strain rates; (2) Safari et al. [2016] present a new adiabatic model based on Mulliken-Boyce's model for the evaluation of the PC at large deformation rates; (3) Sun and Gamstedt [2019] apply a modified model presented by Varghese and Batra [2009] to discuss the phenomenon of shear bands in glassy and amorphous polymers (in the case of the study, the material evaluated was PPMA); (4) Furmanski et al. [2013] use the Mulliken-Boyce model with failure models for the evaluation of PC and ABS under conditions of large deformations and high deformation rates ($> 10,000 \ s^{-1}$); (5) Sarva et al. [2007] apply the original model for the investigation of the PC in Taylor impact experiments, in order to evaluate its mechanical behavior under non-homogeneous deformation conditions. In this latest study, the evaluations were based on the geometry shape after the impact, where the numerical behaviors were compared with the experimental ones. The results show good adequacy of the original Mulliken-Boyce model for the assessment of scenarios in which the occurrence of residual deformations is one of the topics

of interest.

1.2.3 Numerical evaluation of indentation tests

The investigation of the mechanical and geometric parameters of bodies in contact is an important branch of research in tribology. There are several state-of-the-art works that perform this type of numerical study, and, in general, metallic materials continue to dominate the subject. The topic of contact in polymers is becoming more popular, owing to its increasing structural use. However, some factors continue to be obstacles, such as a lack of libraries previously implemented to evaluate the behavior of polymers, including their elastic-viscoplastic behavior. Because of the wide variation in polymer properties caused by their complex molecular structure, dedicated models are usually required to evaluate their performance.

Indentation test is a relatively cheap characterization process employed for the analysis of compression and surface properties. In particular, the sphere-to-flat standard Brinell test which is often used for the evaluation of Hardness Singh [2021]. It can, however, be used to assess other mechanical properties and parameters related to the elastic and plastic phases of the material's mechanical behavior. According to George and Mohammadreza [2020], the elastic stiffness of a material can be determined by analyzing the surface response to the probe's penetration at an imposed load. Moreover, one of the main outputs obtained by the indentation test is a force-displacement relationship. Therefore, when an indentation test is carried-out at finite strain, inelastic properties can also be evaluated in a combined experimental/numerical study.

The Finite Element (FE) modeling is a popular choice for this kind of investigation, as can be identified in the following studiesWang et al. [2017], Pham and Kim [2017], Wang et al. [2019], Peng et al. [2020], Chen and Cai [2020]. These studies have as main objective the identification of elastoplastic properties, such as residual stresses, longitudinal elastic modulus, and stress-strain curve of metallic materials from the behavior of the depth penetration curves by force, as well residual penetration. Chen and Cai [2020] present several studies for different types of indentation in metals, by comparing three different methods: Numerical Model in Finite Elements, experimental tests, and elastic-plastic indentation model (model based on contact mechanics). The authors' results show a good correlation between the three methods used during the study, allowing them to reaffirm what several other authors have presented thus far: the use of numerical models presents itself as a relevant tool for describing the phenomenon of contact between continuous solids.

Tkalich et al. [2016] presents experimental and numerical investigations of the residual deformations of granite under compression, more precisely of the residual indentation. The evaluations were based on a spherical indentation, considering for both 1/4 of the geometry.

Among the aspects presented by the authors, the most relevant for this thesis is related to the adequacy of the numerical force-penetration curve. The results obtained by the authors show a good adequacy of the curve for the loading phase, whereas for the unloading phase it was verified that the numerical results were all overestimated, reaching a difference between the experimental and numerical results of up to 129% (in studies conducted by the authors, the magnitude of residual penetration was in the order of millimeters).

A common complementary approach to experimental analyses is the usage of calibrated numerical models. After a series of experiments, material properties and numerical parameters can be identified and employed in the modeling and simulation of the mechanical behavior of engineering materials or industrial components. In time, an established numerical model can precisely replicate (or even completely replace) a standard experimental testing procedure for a given material class Kudela and Matousek [2022]. However, intricate failure mechanisms (e.g. fatigue and fretting wear) can still be extremely demanding even after thorough modeling and calibration Doca, Doca et al. [2022, 2022]. A mixed model, using FE model and ANN for the prediction of the stress-strain curves, has been presented by Jeong et al. [2020].

1.2.4 Machine Learning Tools Applied to the Mechanical Description of Materials

Nowadays Artificial Intelligence is commonly used in applications in the most diverse research topics, from the automation of routine processes, to, for example, for the diagnosis of diseases. Looking down the path taken by Artificial Intelligence in parallel with the basic purpose of using computers brings up an opportune reflection.

Just like a human being needs to know in advance what would be a house and what would be a car to be able to make distinctions between the two objects, machines also need a source of prior information for this purpose, which can be called inputs. In other words, just as a person cannot identify the dissimilarities between an object X and Y if he never had contact with them, machines are also unable to do so. This ability of the system to acquire knowledge from a database of initial information is known as Machine Learning, one of the subfields of Artificial Intelligence, and is fundamental for the development of this thesis.

The essence of using computers is the intention to process various types of information by algorithms, in most situations to perform humanly laborious activities and tasks that otherwise would be impossible to be carried out in time. Reproducing what would easily be accomplished by an adult, like differentiating a car and a house in an image, was one of the greatest challenges in the early days of Machine Learning. In some tasks, a simple human perception is still difficult to be replicated. Examining the progress of Artificial Intelligence

in the present day, it is possible to identify a steady growth. The models developed today present answers to problems of much greater complexity than a simple classification of images, models developed for cases in which human cognitive ability alone is no longer sufficient to find the necessary answers.

Regarding the Machine Learning subfields, it is possible to identify two major branches of study: Supervised and Unsupervised Learning. In the first case, Supervised Learning, there is the presence of a target, that is, the algorithm will be trained to associate the input data with the output data. For the previously mentioned case of a dataset of images of houses and cars, the imagens would be the input of the system, whereas the description of car or house would define the output, in this case, it could be, for example, 0 for an image of a house and 1 for the image of a car. In the case of Unsupervised Learning, there is no target, the main function of the algorithm is to observe several examples and try to learn without the presence of an instructor. For the case of categorization between home and car, the basic function of the algorithm would be to identify similarities and dissimilarities between the images for the inference of the classification, for example.

Deep Learning also presents itself as one of the subfields within Machine Learning and can be applied to both Supervised and Unsupervised algorithms. This branch of Machine Learning is based on algorithms that try to model high-level abstractions from the use of a chain of layers, which can be designed purely sequentially or in a more complex way, depending on the object of analysis. A philosophical and mathematical view of deep learning is presented by Bengio et al. [2013], where they describe it as a profound learning from a hierarchical view, in which the higher level, more abstract, learn from those of lower levels, with less abstraction.

The use of Machine Learning tools for engineering applications is on the rise and it is possible to find research that makes use of such tools for the description of different behaviors of materials. The main applications of Machine Learning are carried out via numerical implementations, mainly through libraries specially developed for this purpose, as is the case of the open end-to-end platform Tensor Flow present in programming languages like Python and R. An introduction to the functionalities existent in TensorFlow, as well as the Scikit-Learn library, another library widely used in Machine Learning, can be found in several research studies, including: Geron [2017] and Goodfellow et al. [2016], as well as supporting material provided by the developers.

The research developed by Yang et al. [2020], a study in the same field of research as that presented by Gu et al. [2017] in brittle materials, develops a strategy based on Machine Learning tools to obtain the stress-strain curve of composite materials for stress levels above the elastic limit of the material, a strategy adopted due to the high computational cost for conducting simulations on these materials on tools such as Finite Element. To do so, they apply two different tools: (1) Principal Component Analysis (PCA), a multivariate statis-

tical tool that allows reducing the number of variables in order to reduce the redundancy of information, and (2) Convolutional neural network, an image processing and analysis tool that can be used to obtain lower computational cost during the training. According to the authors, the stress-strain curve was defined as the model's output due to its higher degree of difficulty, given its high dimensionality and additionally because it is possible to use it to define other material properties such as: elastic modulus, rigidity, and hardness. For the creation of the target database, a Finite Element modeling was used, generating a dataset of 100,000 different stress-strain curves with 61 pairs of coordinates, which totals 6,100,000 elements. Regarding the model input, the authors used a binary representation with 121 elements (11x11), where 0 represents a soft block and 1 corresponds to a stiff block (representing a plane). The adopted Machine Learning model used the Adam optimizer, batch size equal to 16 and number of epochs equal to 30, presenting a Mean Absolute Error (MAE) less than 10%.

Also, in the field of material science, Mangal [2018] presents in his thesis a methodology based on ML for the prediction of stress hotspots in monophasic equiaxial microstructures due to the presence of inhomogeneous stress distributions in the crystal structure of metals. The model used by the authors was based on a dataset of 56 synthetic microstructures in a tensor form 128x128x128, trained in a neural network composed of non-sequential layers, as well as the application of PCA to reduce the size of the model. In addition to the points covered in the two articles previously mentioned, Miyazawa et al. [2019] present the interference of the configuration of different types of Layers and activation functions, more precisely *tanh* and *ReLU*.

Jordan et al. [2020] present a study about the dependence of the stress-strain curve in relation to temperature and strain rate in uniaxial tensile tests of polypropylene, using an experimental, analytical and Machine Learning approach. The adopted model can predict the stress-strain curve for magnitudes up to 60% from inputs such as strain rate and temperature. The authors address in their study the impact of the construction of layers, more precisely the number of layers and neurons, in the mean squared error (MSE). For the conducted study, the use of a single layer was able to predict the stress-strain curve without the premise of any mathematical function for the description of the specimen's mechanical behavior, providing a good description of all the experiments carried out. The prediction error was less than the experimental uncertainty.

In order to characterize the mechanical damage in specimens, the study of Zobeiry et al. [2020] presents an approach via Machine Learning (ML) in laminated composites reinforced by polymers. To do so, they use the LS-DYNA finite element commercial software to build a numerical damage model, in order to generate the necessary input for training the model in ML. To determine the best parameters to compose the input, a sensitivity analysis was carried out and it was verified that the use of sequential neural networks would not be

relevant for the conducted study, therefore, differently from the studies presented so far, the authors used several independent neural networks for determining the four necessary outputs, a strategy that can be carried out using the API tool present in the Tensorflow library, which allows the construction of non-sequential neural networks, using an output as input to another branch of the neural network. It is worth mentioning that the strategy taken by the authors allowed the application of a model in ML without the need for image processing, as present in: Yang et al. [2020], Gu et al. [2017] and Mangal [2018], which can be practical, due to the high computational cost necessary in the treatment of images by carrying out convolutions and greater memory allocated for data storage and modeling.

Weng et al. [2020] present a study on the use of Machine Learning to correlate constants of a power low function for the description of plastic behavior to the Mean Error between the prediction and measured data. The author's main objective is based on the strategy of calibrating the stress-strain curve of the material, applying it for the determination of the stress-strain curve for the case of a nanoindentation in gray cast iron. In another study about indentations, Jeong et al. [2020] presents mixed models in finite elements and artificial neural network for the prediction of the stress-strain curve of the plastic zone from the force-penetration curve obtained by compression simulation by macro indentation. Regarding the ML model adopted, the force-numerical displacement curve obtained via Finite Element was used as an input and as output, parameters of the constitutive Swift equation for the description of non-linear plasticity. The results obtained by the authors showed that a data of 1000 was sufficient to train the model, providing an error of less than 1% for the predictions made. In addition to the training carried out with 1000 input data values, the Taguchi orthogonal array (OA) method was applied, which consists of using a limited number of experiments within a set, selected by the combination of multiple factors, which allowed the use of 100 data values instead of 1000. In order to show the effectiveness of such a model, the predictions were compared with the original model, as well as random splits of 100 data values out of 1000. The results show that the training carried out from the application of the OA method presented similar performance as the initial model with 1000 data values as dataset. When evaluating the performance of random splits, it appears that the results were not satisfactory. Another interesting study about the extraction of mechanical properties of materials from indentation tests can be found in Lu et al. [2020], work in the same research domain as those pointed out during this last paragraph.

1.3   Objectives

The use of artificial intelligence is present in the most diverse research fields and engineering applications. Thus, the present work has as main objective the development of a framework for the prediction of the mechanical behavior of inelastic solid materials under

compression. Three analysis steps are undertaken: (1) experimental tests, (2) numerical implementations via Finite Element and (3) development and implementation of neural networks for prediction.

The main hypothesis discussed throughout this work is based on the use of neural networks to predict the behavior of materials under pre-established conditions, which is typically obtained through experimental tests. In this study, predictions were made in two configurations: (1) uniaxial compression in polymers and (2) residual indentation in metals, both with large strains. As the results are presented, it will be possible to evaluate the performance of the neural networks adopted, as well as their use to aid the calibration process of numerical models. For some cases, some considerations should apply.

In more detail, the investigations carried out for the study of polymers are based on the use of neural networks to: (1) prediction of the stress-strain curve from the material parameters of an adopted constitutive model and (2) prediction of the material parameters of a constitutive model using as input an experimental stress-strain curve. The first case evaluates the ability of neural networks to reproduce the results obtained via numerical implementations of a constitutive model and the second case represents the use of neural networks to support the calibration process necessary for the implementation of the constitutive equations via a numerical model.

For metals, the hypothesis to be evaluated is based on the use of neural networks to: (1) prediction of the stress-strain curve from the displacement-force curve for indentation tests and (2) prediction of the displacement-force curve, residual indentation, and contact pressure from material properties. The first case evaluates the use of neural networks to describe the stress-strain curve for a given metal from a displacement-force curve obtained via indentation experiments, and the second case evaluates the ability of neural networks to obtain other important parameters also obtained or via indentation experiments.

To reach the proposed objective, some steps have to be performed, for polymers: (1) due to the performance of simulations in large deformations, implementation of a numerical constitutive model to describe the elastic-viscoplastic behavior of polymers via Finite Element, (2) implementation and calibration of a numerical model for reproducing the uniaxial compression test, (3) creation of datasets for further training of the ANN model, and (4) implementation of neural networks model for the prediction of the established parameters. For Metals: (1) implementation of a numerical constitutive model to describe the elasto-plastic behavior of metals via Finite Element, (2) implementation and calibration of a numerical model for reproducing indentation tests by spherical indenter, (3) creation of datasets for further training of the ANN model, and (4) implementation of neural networks model for the prediction of the established parameters.

It should be noted that the implementation of a numerical model for the description of the elasto-viscoplastic behavior of the evaluated polymers is a fundamental step for the

13

study carried out and contributes to the state-of-the-art, given the limited number of works in this field. The numerical model applied to describe the behavior of the evaluated metals is already widely applied and does not bring great contributions.

1.4 Outline

This document comprises:

Chapter 1: Contextualization and introduction to the topic of study, as well as the objectives pursued in this thesis;

Chapter 2: Presentation of the basic concepts of Continuum Mechanics, in order to present the mathematical basis pertinent to the constitutive models and introduction to concepts related to contact mechanics;

Chapter 3: Detailing of the most widely used computational plasticity models. This chapter presents in more detail the constitutive model for the evaluation of polymeric materials;

Chapter 4: (1) Definition of the constitutive models adopted for studying the mechanical behavior of thermoplastic polymers and metals under predefined conditions, (2) validation of both models adopted through uniaxial compression tests on polymers and indentation tests on metals and, (3) presentation of the methodology adopted for the implementation of ANN for predicting the desired targets for the different studies carried out;

Chapter 5: Presentation of the results obtained for each of the studies carried out, as well as discussion of the main points observed. After presenting all the identified results, a general conclusion is presented;

Chapter 6: This chapter presents future works that will continue to be developed, mainly directed to the study of polymers.

Chapter 2

Mechanical behavior of solids

In this chapter the reader will find the basic principles and properties about continuum mechanics, which will provide the necessary basis for understanding the constitutive models presented in the subsequent chapters for the evaluation of the visco-elastoplastic mechanical behavior of solids. In addition, it is also presented in this chapter about Henck's Hyperlastic Model, base model for the description of the mechanical behavior of materials as polymers.

Subsequently, it can find a brief introduction on the most pertinent concepts and principles about the mechanics of contact, an important basis for the numerical applications carried out later in the study of the contact between a sphere and flat surface, such as the Hertz formulation for the specific case of contact between two spheres, a formulation that can be used for contact between sphere and plane when considering one of the bodies having infinite radius.

2.1 Continuum Mechanics

Continuum Mechanics consists of the study of solids and fluids through a unified approach, where the analyzed subject can be divided into three different parts. The first part refers to field equations, something applied simultaneously to solids and fluids. The second part refers to the constitutive equations, which are different for each type of solid or fluid studied. Finally, the third part deals with objects of analysis that can only be studied from governing equations obtained by combining field equations with appropriate constitutive equations.

According to [15], it is known that the physical object is composed of molecules, which are composed of atoms and, therefore, particles that are not continuously distributed in the object (macroscopic observations reveal the presence of empty spaces between particles). The presence of gaps may or may not be considered when studying the external effects on a

physical object, depending on the hypothesis taken as a basis. The study that considers the presence of gaps is called a microscopic study, whereas the study that ignores the presence of gaps and considers the physical object as a continuous distribution of matter is called a macroscopic study.

Based on the macroscopic view of a solid or fluid, the notion of Continuum can be described as a hypothetical physical material in which all matter is continuously distributed throughout the object. It can be used to study deformations and movements of the continuum from a unified approach to the mechanics of solids and fluids.

2.1.1   Kinematic Description of a Continuum

Considering a deformable body represented by a Continuum that occupies a volume V in an initial instant (t=0). The application of an external force to this body causes a displacement of each material point that composes it, in which the trajectory can be defined as an evolution of the position $\vec{x}$ as a function of time (t). It is worth noting that the coordinates called materials are constant over time, whereas spatial coordinates evolve over time. The equation 2.1 formally represents the set of trajectories of all material points of the continuum [48].

$$\vec{x} = \vec{\phi}(\vec{X}, t) \tag{2.1}$$

Regarding the mathematical aspect, the transformation $\vec{\phi}$ is a bijective function, that is, each material point $\vec{X}$ corresponds only to a single spatial point at each instant t. In the same sense, two distinct material points cannot present the same spatial position for each instant t. Thus, the initial position of a particle can be obtained by the inverse of eq. 2.1, such as:

$$\vec{X} = \vec{\phi}^{-1}(\vec{x}, t) \tag{2.2}$$

given the bijective characteristic existing between the spatial and material coordinates, an Eulerian representation ($\vec{x}$,t) and a Lagrangian representation ($\vec{X}$,t) can be defined as an independent variable for the description of the movement.

Once the transformation of the Continuum $\vec{\phi}$ has been defined, the notions of displacement, velocity and acceleration can be represented as eq. 2.3 with support of figure 2.1.

$$\vec{u}(\vec{X}, t) = \vec{x}(\vec{X}, \vec{t}) - \vec{X}$$

$$\vec{v}(\vec{X}, t) = \frac{\partial}{\partial t}\vec{u}(\vec{X}, t) \tag{2.3}$$

$$\vec{a}(\vec{X}, t) = \frac{\partial}{\partial t}\vec{v}(\vec{X}, t)$$
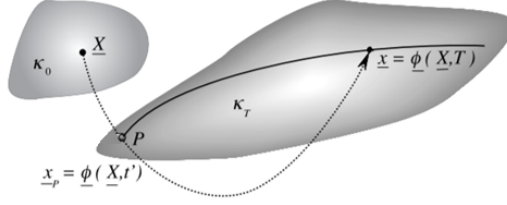
Figure 2.1: Representation of the Continuum transformation.

2.1.2 Deformation of a Continuum

Adopting a Lagrangian point of view and considering a transformation $\vec{\phi}$ from an initial configuration ω_0 to a current configuration ω, the local transformation in the vicinity of a point $\vec{X}$ can be described, with reference to the initial spatial coordinates, as:

$$\vec{dx} = \boldsymbol{F} d\vec{X} \tag{2.4}$$

That is, the Gradient Strain Tensor $\boldsymbol{F}$ can be defined by:

$$\boldsymbol{F} = \frac{\partial \vec{x}}{\partial \vec{X}} \tag{2.5}$$

Chadrasekharaiah and Debnath [1943] shows that from a mathematical point of view, the vectors $d\vec{X}$ and $d\vec{x}$ are elements of vector spaces that tangent to $\vec{X}$ and $\vec{x}$, respectively. Since $d\vec{X}$ and $d\vec{x}$ belong to distinct spaces, an expression like $d\vec{X} + d\vec{x}$ has no mathematical meaning. From a physical point of view, $d\vec{X}$ represents the direction of a line or material fiber drawn in ω_0 that necessarily passes through X. This line becomes a curve which the tangent in x is in accordance with $d\vec{x}$.

The deformation gradient can also be called a transformation gradient, as it is a tangent linear application. Its existence comes from the regularity admitted for $\vec{\phi}$ and particularly in the initial time ($t=0$) it is identical to the second-order identity tensor, since $\omega(\vec{X}, 0) = \vec{X}$. Another important characteristic of the deformation gradient tensor is that the determinant is always greater than zero.

$$\boldsymbol{F}(\vec{X}, t = 0) = \boldsymbol{I} \tag{2.6}$$

As already presented, the deformation of a material fiber element $d\vec{X}$ (initial configuration) for a later configuration ($d\vec{x}$) is performed through the deformation gradient $\boldsymbol{F}$. Therefore, it is possible to establish how volumes and surfaces behave as the body moves.

Having as reference the presence of three non-coplanar material vectors ($d\vec{X}_1$, $d\vec{X}_2$ and $d\vec{X}_3$), the scalar triple product between them can be expressed as:

$$dX_1 \cdot (dX_2 \wedge X_3) > 0 \tag{2.7}$$

Give that the scalar triple product presented above represents the volume of a parallelepiped delimited by three vectors, it can be presented that:

$$dV = dX_1 \cdot (dX_2 \wedge X_3) > 0 = \left[dX_1, dX_2, dX_3 \right] \tag{2.8}$$

that is, the scalar triple product can be obtained by the determinant of a second order tensor composed of the three column vectors, as follows:

$$dV = dx_1 \cdot (dx_2 \wedge x_3) > 0 = [dx_1, dx_2, dx_3] = [\boldsymbol{F}dx_1, \boldsymbol{F}dx_2, \boldsymbol{F}dx_3] = (det\boldsymbol{F}) \left[dX_1, dX_2, dX_3 \right] \tag{2.9}$$

and written in another way, in terms of the Jacobian, as:

$$\frac{dv}{dV} = J \ , \ J \colon = det\boldsymbol{F} > 0 \tag{2.10}$$

Regarding the deformation process, if a material body in a reference configuration ω_0 is submitted to a transformation $\boldsymbol{F}_1$ and immediately afterwards, starting from a configuration ω_1, it is submitted to a new $\boldsymbol{F}_2$ transformation. The total transformation, in reference to the ω_0 reference configuration, can be represented by:

$$\boldsymbol{F} = \boldsymbol{F}_1\boldsymbol{F}_2 \tag{2.11}$$

this equation shows that the deformation of a solid can be decomposed and mathematically represented by a tensor product. However, it is important to note that the mathematical procedure presented is not applicable for all types of deformation gradients.

In the same line of reasoning, Kroner [1959] and Lee [1969] showed that the deformation gradient can be decomposed multiplicatively into elastic and plastic components, such as:

$$\boldsymbol{F} = \boldsymbol{F}^e\boldsymbol{F}^p \tag{2.12}$$

2.1.3 Deformation tensors

It is considered a rigid body that moves according to:

$$\vec{x}(\vec{X}, t) = \boldsymbol{R}(t)\vec{X} + \vec{c}(t) \tag{2.13}$$

where, $\boldsymbol{R}$ represents a rigid body rotation and $\vec{c}$ a rigid translational displacement.

Since $\boldsymbol{R}$ is an orthogonal tensor, the following property is therefore valid:

$$\boldsymbol{R}\boldsymbol{R}^T = \boldsymbol{R}^T\boldsymbol{R} = \boldsymbol{I} \tag{2.14}$$

For pure rigid body movement, the deformation gradient tensor $\boldsymbol{F}$ is not null, but equal to the rotation tensor.

As exposed by Simo and Hughes [1997], the right and left Cauchy-Green deformation tensors are presented as alternatives for the use of the deformation gradient tensor. The use of such tensors is present, for example, in constitutive equations of hyperelasticity and they are of great importance in the studies conducted during this thesis. The definition of the right Cauchy-Green deformation tensor can be obtained from the scalar product between two elementary vectors $d\vec{X}_1$ and $d\vec{X}_2$ as they become $d\vec{x}_1$ and $d\vec{x}_2$, as follows:

$$\vec{dx}_1.\vec{dx}_2 = (\boldsymbol{F}.\vec{dX}_1).(\boldsymbol{F}.\vec{dX}_2) = \vec{dX}_1.(\boldsymbol{F}^T.\boldsymbol{F}).\vec{dX}_2 = \vec{dX}_1.\boldsymbol{C}.\vec{dX}_2 \tag{2.15}$$

That is,

$$\boldsymbol{C} = \boldsymbol{F}^T\boldsymbol{F} \tag{2.16}$$

This is a second order tensor, symmetrical and called material tensor since it operates from also material vectors.

In Lagrangian representation, the expression of the scalar product of the elementary vectors in a reference configuration as the initial configuration can be presented by:

$$\vec{dX}_1.\vec{dX}_2 = (\boldsymbol{F}^{-1}.\vec{dx}_1).(\boldsymbol{F}^{-1}.\vec{dx}_2) = \vec{dx}_1.(\boldsymbol{F}^{-T}.\boldsymbol{F}^{-1}).\vec{dx}_2 = \vec{dx}_1.\boldsymbol{B}.\vec{dx}_2 \tag{2.17}$$

where $\boldsymbol{B}$ is called the left Cauchy-Green deformation tensor, also being a symmetrical and second order tensor. However, it is important to note that, unlike the Cauchy-Green expansion tensor on the right, this is a spatial tensor.

$$\boldsymbol{B} = \boldsymbol{F}\boldsymbol{F}^T \tag{2.18}$$

Like the $\boldsymbol{F}$ tensor, $\boldsymbol{C}$ and $\boldsymbol{B}$ tensors also have the property of not being null in rigid body movements.

2.1.4   Polar Decomposition

From a purely mathematical point of view, it can be shown that every second-order tensor can be written as the product of an orthogonal tensor $\boldsymbol{R}$ and another symmetric tensor called $\boldsymbol{U}$, such as:

$$F = RU \tag{2.19}$$

Based on eq. 2.16 and applying the equation eq. 2.19, it is possible to show that:

$$C = F^T F = U^T R^T R U = U U \tag{2.20}$$

that is, the U tensor can be determined by the square root of the right Cauchy-Green deformation tensor (C), as shown below:

$$U = \sqrt{C} \tag{2.21}$$

In order to determine the solution of the equation presented in eq. 2.21, Chaves [2019] shows that it is necessary to rotate this tensor until it contains only the eigenvalues on its main diagonal. In this way, the square root can be determined using the relation shown below, since C' only presents values in its main diagonal.

$$\sqrt{C'} = \begin{bmatrix} \sqrt{c'_{11}} & 0 & 0 \\ 0 & \sqrt{c'_{22}} & 0 \\ 0 & 0 & \sqrt{c'_{33}} \end{bmatrix} \qquad Where: \qquad C' = \begin{bmatrix} c'_{11} & 0 & 0 \\ 0 & c'_{22} & 0 \\ 0 & 0 & c'_{33} \end{bmatrix} \tag{2.22}$$

Since C is a positive symmetric tensor, it has a set of positive eigenvalues ($\lambda_{11}, \lambda_{22}$ and λ_{33}), which allows rewrites it as:

$$C = Q^T C' Q \tag{2.23}$$

In this case,

$$C' = \begin{bmatrix} \lambda_{11} & 0 & 0 \\ 0 & \lambda_{22} & 0 \\ 0 & 0 & \lambda_{33} \end{bmatrix} \qquad and \qquad Q = \begin{bmatrix} \vdots & \vdots & \vdots \\ N_1 & N_2 & N_3 \\ \vdots & \vdots & \vdots \end{bmatrix} \tag{2.24}$$

Finally, the U tensor can be determined by:

$$U = \sqrt{C} = Q^T . \sqrt{C'} . Q \tag{2.25}$$

According to Chadrasekharaiah and Debnath [1943], the decomposition presented above portrays that the tensor U performs an extension of the $d\vec{X}$ fiber and then a rotation R of that fiber is applied. Such a tensor is configured as a material tensor, as well as F.

Similar to that performed in eq. 2.19, it is also possible to decompose F in terms of a

rotation tensor followed by a stretch tensor in a spatial configuration denoted by $\boldsymbol{V}$, such as:

$$\boldsymbol{F} = \boldsymbol{V}\boldsymbol{R} \tag{2.26}$$

i. e.,

$$\boldsymbol{V} = \boldsymbol{F}\boldsymbol{R}^{-1} \tag{2.27}$$

In summary, the figure 2.2 explains the transformations presented so far. Through it, it is possible to verify three different transformations, the first represents the purely application of the gradient deformation tensor, the second represents a material transformation, where first there is a stretching of the body to later rotate it. Finally, the third represents a spatial transformation, where at first there is the rotation of the object to later stretching it.
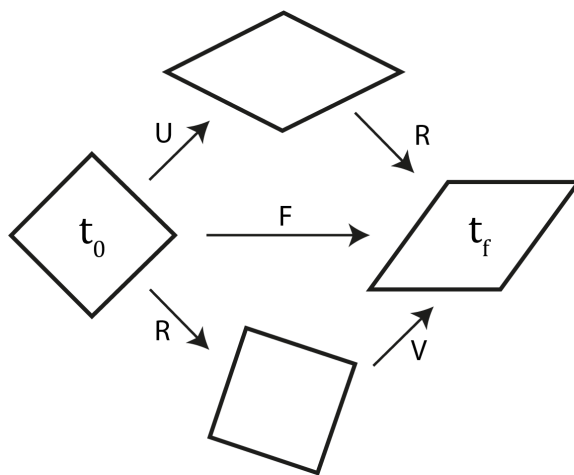
Figure 2.2: Linear stretching and rotation transformations.

Two other important properties of the tensors $\boldsymbol{U}$ and $\boldsymbol{V}$ refer to the determination of Hencky's Lagrangian and Eulerian logarithmic deformations (something discussed in more detail in the section 2.1.6) and can be expressed as follows:

$$\log\left(\boldsymbol{U}\right) = \frac{1}{2}\log\left(\boldsymbol{C}\right) \tag{2.28}$$

$$\log\left(\boldsymbol{V}\right) = \frac{1}{2}\log\left(\boldsymbol{B}\right) \tag{2.29}$$

2.1.5 Velocity Gradient

The determination of the strain-rate tensor assumes that the spatial representation of the velocity gradient ($\boldsymbol{L}$) can be expressed by:

$$L(\vec{x}, t) = \nabla \vec{v}(\vec{x}, t) \tag{2.30}$$

Being the time derivative of the deformation gradient:

$$\dot{\boldsymbol{F}} = \frac{\partial^2 \phi}{\partial t \partial \vec{X}}(\vec{X}, t) = \frac{\partial^2 \phi}{\partial \vec{X} \partial t}(\vec{X}, t) = \nabla \vec{V}(\vec{X}, t) = \nabla \vec{v}(\vec{x}, t) \boldsymbol{F} \tag{2.31}$$

the inverse of the gradient on both sides of the equation can be applied, allowing to find that:

$$\boldsymbol{L} = \dot{\boldsymbol{F}} \boldsymbol{L}^{-1} \tag{2.32}$$

Since every tensor can be expressed as the sum of a symmetric part $\boldsymbol{D}$ and another asymmetric part $\boldsymbol{W}$, the velocity gradient tensor $\boldsymbol{L}$ can be expressed by:

$$\boldsymbol{L} = \boldsymbol{D} + \boldsymbol{W} \tag{2.33}$$

Where, $\boldsymbol{D}$ can be understood as a strain rate and $\boldsymbol{W}$ as a rotation rate tensor Irgens [2008].

Since the elastic deformation gradient is restricted to being only the result of the elongation ($\boldsymbol{L}$), it can therefore be decomposed into:

$$\boldsymbol{L} = \boldsymbol{L}^e + \boldsymbol{L}^e \boldsymbol{L}^p (\boldsymbol{L}^e)^{-1} \tag{2.34}$$

Where,

$$\boldsymbol{L}^p = \dot{\boldsymbol{F}}^p (\boldsymbol{F}^p)^{-1} = \boldsymbol{D}^p + \boldsymbol{W}^p \tag{2.35}$$

In the equation 2.35, $\boldsymbol{D}^p$ is the plastic strain rate and $\boldsymbol{W}^p$ is the plastic rotation rate tensor. For isotropic materials, $\boldsymbol{W}^p$ is assumed to be a null tensor, which allows to present that:

$$\dot{\boldsymbol{F}}^p = \boldsymbol{D}^p \boldsymbol{F}^p \tag{2.36}$$

2.1.6 Hencky's Hyperelastic Model

According to Xiao and Chen [2002], the hyperelasticity model of Hencky [1931] presents itself as a model of finite isotropic elasticity with a linear relationship between the Kirchhoff stress tensor and the logarithmic strain tensor (Hencky deformation). This model is

configured as a generalization of the classic law of Hooke Truesdell and Noll [1965] for a case of infinitesimal elasticity (eq.2.37).

$$\mathcal{L}_{ijkl} = \Lambda\delta_{ij}\delta_{kl} + G(\delta_{ik}\delta_{jl}\delta_{jk}) \tag{2.37}$$

Assuming that the stress-strain relationship for an isotropic solid in infinitesimal strains is characterized by Hooke's law, that is, it can be represented by the tensor of fourth order of linear elasticity (eq.2.37), a consideration of an isotropic material and symmetry of the stress tensor allows to obtain:

$$\boldsymbol{\sigma} = \Lambda tr(\epsilon)\boldsymbol{I} + 2G\boldsymbol{\epsilon} \tag{2.38}$$

In this case, $\boldsymbol{\sigma}$ represents the Cauchy stress tensor, $\boldsymbol{\epsilon}$ the infinitesimal strain tensor; Λ and G are Lamé's elastic constants, which can be determined by the relationships below:

$$\Lambda = \frac{E\nu}{(1+\nu)(1-2\nu)} \tag{2.39}$$

$$G = \frac{E}{(1+\nu)} \tag{2.40}$$

The relationship for an isotropic elastic solid, in the case of infinitesimal deformations, can be described from a non-linear stress response function, in which the stress is a function of the right Cauchy-Green deformation tensor as $\boldsymbol{\sigma} = \Phi(\boldsymbol{B})$. According to Truesdell and Noll [1965] and Ogden [1985], this relationship can be called hyperelastic or in the sense of Green, whenever there is a potential isotropic function called a stress-energy function, such as $\sum = \hat{\sum}(\boldsymbol{B})$.

In fact, Hooke's law was developed to represent an isotropic hyperelastic relationship in infinitesimal deformations, as presented in eq. 2.37. However, it can be used to describe the elastic behavior of engineering materials within an adequate range of finite deformations. For this purpose, the replacement of the Cauchy stress tensor and infinitesimal deformation is performed by the Kirchhoff tensor and finite deformation, respectively, according to eq. 2.41.

$$\boldsymbol{T} = \Lambda tr(\boldsymbol{E})\boldsymbol{I} + 2G\boldsymbol{E} \tag{2.41}$$

The strain tensor can be represented logarithmically as:

$$\boldsymbol{E} = \frac{1}{2}ln(\boldsymbol{B}) \tag{2.42}$$

Considering the relationship between Cauchy and Kirchhoff tensors, the elastic stress

can be expressed by:

$$\boldsymbol{\sigma}^e = \frac{1}{J^e}(2\mu^e \boldsymbol{E}^e + \lambda^e tr(\boldsymbol{E}^e)\boldsymbol{I}) \tag{2.43}$$

The term referring to logarithmic deformations can be obtained from the principal applied stretches and the corresponding orthonormal vectors represented by the eigenvectors of the right Cauchy-Green deformation tensor.

$$\boldsymbol{E} = \sum_{i=1}^{3} ln(\lambda_i) \otimes n_i n_i \tag{2.44}$$

Tomas et al. [2008] present that an approximation to the logarithmic deformation can be performed from a fourth-order Padé approximator expanded in the vicinity of the second-order identity tensor, as follows:

$$\boldsymbol{E} = \ln(\boldsymbol{U}^e) = \ln(\sqrt{\boldsymbol{F}^{eT}\boldsymbol{F}^e}) = \ln(\sqrt{\boldsymbol{C}^e}) \tag{2.45}$$

$$ln(\sqrt{\boldsymbol{X}}) \approx 3(\boldsymbol{X} + \boldsymbol{I})(\boldsymbol{X} - \boldsymbol{I})[2(\boldsymbol{X}^2 + 4\boldsymbol{X} + \boldsymbol{I})]^{-1} \tag{2.46}$$

2.2 Analytical Conception of Contact Mechanics

Contact Mechanics is a field of knowledge, which focuses on the interaction between two or more surfaces in contact, either through the application of external loads, or through the molecular interaction between the surfaces in contact.

When two solid surfaces are in contact with the application of a compressive load or even without the application of external forces, when only the body forces act, there will always be distortions in each of the solids. Such deformations will be purely elastic if the internal forces are not large enough to cause stresses above the elastic limit of the material. Otherwise, the solids will present permanent deformations.

The changes in the surfaces in contact can be observed in two different scales: microscopic or macroscopic. On a microscopic scale, the deformations will cover the roughness of the surface in contact, while on the macroscopic scale they will cover the geometric deformations of the solid and can be classified according to the following classes:

1. Punctual Contact (example: sphere/sphere);

2. Linear Contact (example: cylinder/cylinder);

3. Surface Contact (example: plane/plane).

In view of the brief introduction presented so far, Hertz's theory presents itself as an analytical investigation of the mechanical behavior of solids in contact, which can be applied, mainly, for the study of punctual and linear contact. However, extensions of Hertz's theory can be carried out to study more complex contact configurations.

According to Johnson [1985], a first consideration for applying the theory of Hertz [1882] is based on the fact that, initially, when two elastic solids of revolution are brought into contact, this contact will occur over a line or a point, depending on the geometry of the surfaces in contact. The application of an external load, or even the effect of body forces, will cause deformations in the vicinity of the point initially in contact, originating no longer a line or a point in contact, but an area (it is important to note that the region in contact should have dimensions much smaller than the other dimensions of the solids). The four main conditions of Hertz's theory are presented below.

1. All solids in contact must respect Hooke's law, that is, present homogeneous, isotropic and linear elastic behavior;

2. The surfaces in contact must be continuous and counter-formal;

3. The applied forces must be purely normal, without the presence of tangential forces.

4. The area in contact should be small when compared to the dimensions of the solids in contact and the equivalent radii of curvature.

The fourth hypothesis is based on the consideration of elastic semi-spaces to determine local displacements. When a normal compression force is applied, a small elliptical area represents the region of contact between the bodies. In this case, the contact pressures must not suffer any interference from the presence of the boundaries.

The mathematical description of the punctual contact phenomenon can be carried out by applying a normal load of small magnitude to both solids, as shown in Figure 2.3. The region in contact between the solids deforms elastically in a distributed and symmetrical way around an initial point of contact Johnson [1985].
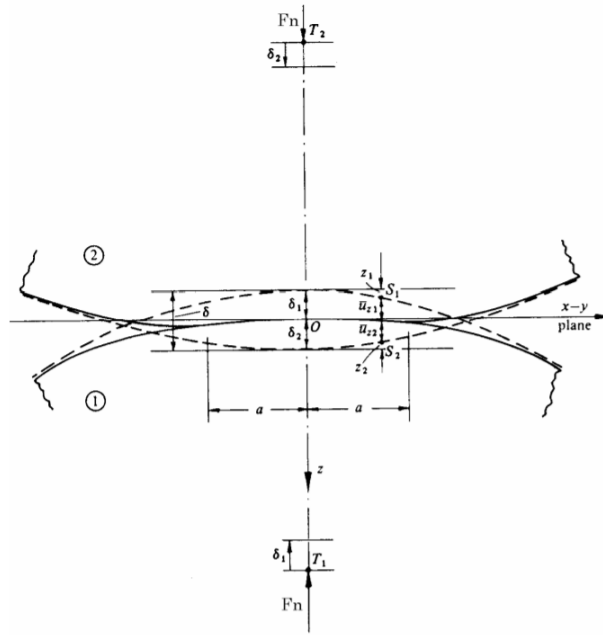
Figure 2.3: Geometric representation of the deformation of elastic bodies subjected to purely normal load. Johnson [1985]

As normal compressive force is applied, the centers of the contacting solids represented by δ_1 and δ_2 shift. The approximation of the centers can be determined by the distance between them, known as penetration, that is, $\delta = \delta_1 + \delta_2$.

The term called penetration does not represent the term itself, since there is no penetration between bodies, something physically impossible. The formulation for penetration represents the elastic displacements in the z direction that the bodies undergo. Such displacements can therefore be represented for each solid by:

$$\overline{u}_{z,1} = w_1$$

$$\overline{u}_{z,2} = w_2$$

$$(2.47)$$

where, the distance between the points presented by S_1 and S_2, in the occurrence of elastic deformations, can be obtained, geometrically by:

$$z = z_1 + z_2 - \delta + (\omega_1 + \omega_2) \tag{2.48}$$

The surfaces of the solids in contact can be described by a polynomial function, thus, eq. 2.48 can be rewritten as present in eq. 2.49. In this case, the polynomial function for the description of the surface in contact was truncated to terms greater than 2.

$$z = Ax^2 + Bx^2 - \delta + (\omega_1 + \omega_2) \tag{2.49}$$

26

The equation presented in eq. 2.49 allows to infer that the right side of the equation is always equal to or greater than zero, since it becomes null when the points S_1 and S_2 establish contact. Otherwise, it will always be greater than zero.

Therefore, it can be said that for the considerations presented, the distance between two points on the surface of each solid, when located on the same normal to the common tangent plane, can be represented by:

$$Ax^2 + Bx^2 - \delta + (\omega_1 + \omega_2) \geq 0 \tag{2.50}$$

where, such an inequality expresses the relationship between geometric modifications and elastic displacements, being the starting point for the mathematical development of the elastic contact problem developed by Hertz.

By analogy to the electrostatic problem, in which the intensity of an electric charge in an elliptical area produces parabolic variation of the electric potential over a surface, the force distribution per unit area can be expressed in a semi-ellipsoidal form, as shown in eq. 2.51, where a and b represent the major and minor semi-axes, respectively.

$$p(x,y) = p_0 \sqrt{1 - \frac{x^2}{a^2} - \frac{y^2}{b^2}} \tag{2.51}$$

In this case, the total applied load can be expressed in two different ways:

$$F_n = \iint_S p(x,y)\, dx\, dy = \iint_S p_0 \sqrt{1 - \frac{x^2}{a^2} - \frac{y^2}{b^2}}\, dx\, dy \tag{2.52}$$

$$F_n = \frac{2}{3} \pi\, a\, b\, p_0 \tag{2.53}$$

For the case of two solids in contact, the use of elastic semi-spaces subjected to point charges allows to determine that the equivalent Young's modulus (E^*) can be determined as:

$$\frac{1}{E^*} = \left(\frac{1 - \nu_1^2}{E_1} + \frac{1 - \nu_2^2}{E_2} \right) \tag{2.54}$$

The parameters of maximum Hertz pressure (p_0) and average pressure (p_m) can be defined by:

$$p_0 = \frac{3}{2} \frac{F_n}{\pi\, a\, b} \tag{2.55}$$

$$p_m = \frac{F_n}{\pi\, a\, b} \tag{2.56}$$

The specific study of the contact between a sphere and a flat plane, the main object of analysis during this thesis, can be performed from the observation of contact between two spheres with radii of curvature defined by R_1 and R_2 (Fig. 2.4). In this situation, the contact area is defined in a circular shape, which corresponds to an ellipse with a semi-major axis identical to the semi-minor axis $(a = b)$.
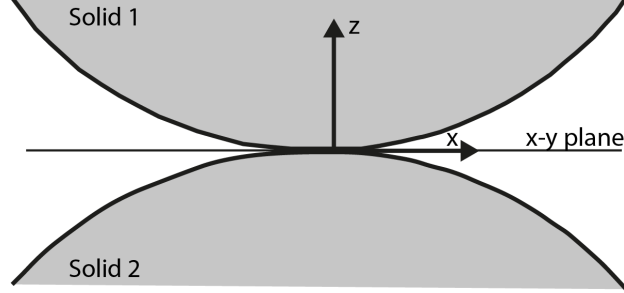
Figure 2.4: Counter-formal contact between two spherical surfaces.[Reproduction]

Therefore, the equation presented in eq. 2.51 can be expressed by:

$$p(r) = p_0 \sqrt{1 - \frac{r^2}{a^2}} \tag{2.57}$$

The radius of the Hertzian contact area can be described as a function of the normal force applied or as a function of the maximum Hertz pressure, as shown in eq. 2.58.

$$a = b = \sqrt[3]{\frac{3}{4} \frac{F_n}{(A+B)E^*}} = \frac{\pi}{3} \frac{p_0}{(A+B)E^*} \tag{2.58}$$

Where, parameters A and B can be determined by:

$$A = B = \frac{1}{2} \left(\frac{1}{R_1} + \frac{1}{R_2} \right) \tag{2.59}$$

and penetration by:

$$\delta = \frac{3}{4} \frac{F_n}{a\,E^*} = a^2(A+B) = \frac{\pi}{2} \frac{a\,p_0}{R^*} \tag{2.60}$$

The theory of Boussinesq [1885] together with the assumptions that solids in contact behave like elastic semi-spaces, makes it possible to determine the solution for the stress state inside the solids in contact

Based on the same coordinate system shown in fig.2.4 and assuming that in the case of the Hertz contact, the stresses along the OZ axis are the main stresses due to the geometric and contact symmetry, it is possible to observe, at first empirically, that the principal stresses σ_{xx}, σ_{yy} and σ_{zz} reach their maximum magnitudes at the contact surface and decrease as it moves away from this surface towards the interior of the solid .

The main stress of greater magnitude is present in the direction of the compressive load application (direction of the OZ axis) and can be determined by Johnson [1985]:

$$\sigma_{max} = C_\sigma \sigma_{ref} \tag{2.61}$$

$$C_\sigma = \frac{3}{2} \frac{k}{\pi} \frac{1}{C_a^3} \tag{2.62}$$

$$\sigma_{ref} = a(A + B)E^* \tag{2.63}$$

For the case of contact between two spheres, the term referring to the eccentricity of an ellipse is equal to 1, configuring a region of circular contact. The term C_a can be expressed according to eq 2.64, and for this case it is approximately equal to 0.91.

$$C_a = \sqrt[3]{\left(\frac{3\,a}{3\,\pi\,b}\right) \int_{\frac{\pi}{2}}^{0} \sqrt{1 - \left(1 - \frac{a^2}{b^2}\right) sin(\alpha)^2} d\alpha} \tag{2.64}$$

Regarding the shear stresses, these can be determined by:

$$\tau_{max} = C_\tau \sigma_{ref} \tag{2.65}$$

in which, C_τ can be obtained by eq. 2.66 and for a sphere-sphere configuration it is equal approximately to 2.35.

$$C_\tau = \frac{3}{2} \frac{a}{b} \int_{\frac{\pi}{2}}^{0} \frac{d\alpha}{\sqrt{1 - \left(1 - \frac{a^2}{b^2}\right) sin(\alpha)^2}} \tag{2.66}$$

2.3   Material Hardness

According to Gianfrancesco [2017], the term hardness can be defined as the resistance of the material to plastic deformation such as indentation, wear, abrasion and scratch. The SI unit of hardness is N/mm^2, however, different types of hardness are found in the bibliography and are not necessarily presented following the SI. Brinell and Rockwell are the main methods commonly used.

The different types of hardness (Brinell, Rockwell and others) are measured using different methods. The common point between them is the application of an indent in order to create an indentation on the test piece surface area, in which harder materials have shallow indentation whereas softer materials will present fewer deep indentations.

The Brinell test consists of a steel ball of 10 mm in diameter as an identifier, usually maintained for 30 seconds under the application of a compressive load. The magnitude

of the load depends on the material tested, however, commonly is 3000 kg but it can be reduced to 500 kg for softer materials.

After removing the identifier, the dimensions of the dent are measured and used to calculate Brinell hardness using the following equation:

$$HB = \frac{2F}{\pi D(D - \sqrt{D^2 - d^2})} \tag{2.67}$$

where, F represents the force in N, D the indenter diameter and d the indentation diameter, both in mm.

The Brinell hardness test is applied primarily to metallic materials, whereas the Rockwell test can be applied to a wider range of materials, in which different scales represent different material characteristics, each one providing the information about the indenter and compression load.

As an experimental procedure, before carrying out the Rockwell hardness test, a small test load is applied in order to set the indenter on the test piece and remove the effect of surface irregularities, thus providing better accuracy.

A relevant point for the experimental test is the loading speed. It appears that variations in the speed of load application can produce considerable differences in the measured hardness value. Finally, the formula for Rockwell hardness is:

$$HR = N - \frac{d}{s} \tag{2.68}$$

where, N and s are scales factors depending on the scale used, and d is the depth of the permanent indentation in mm.

Chapter 3

Constitutive Models

In order to present the reader about constitutive models in plasticity Regimes, this chapter aims to present the plasticity models most commonly applied for the description of plastic behavior in solids. As it will be possible to identify, most models applied to metals do not present a good prediction of the behavior of polymers, therefore, it is presented later on models applied specifically for the visco-elastoplastic description of polymers. The main model presented in this chapter concerns the Mulliken-Boyce model, a base model for the future applications of this thesis. In this way, it is also presented about the numerical implementation of such a model, as well as a sensitivity analysis of the main parameters that constitute such a model.

3.1 Numerical Plasticity Models

The theory of elasticity limited by Hooke's laws was developed, above all, for the study of isotropic solids, applying, therefore, for the description of temporary deformation phenomena. In these events, the deformed solid recovers exactly its primitive form after removing the previously applied external forces. In certain circumstances, when the applied force amount causes stress above a certain level (yield stress), even after removing the external stress, permanent deformations are present, that is, the solid no longer presents its initial configuration [62].

Considering the stress-strain curve for a uniaxial test of a ductile metal (Figure 3.1), it is possible to identify the presence of the two zones previously indicated. The first domain represents the existence of a purely elastic zone, that is, without the evolution of any permanent deformation (plastic deformation) and is bounded by the yield stress (Y_0).

If the material continues to be loaded until it exceeds the yield stress, there will be an evolution of permanent deformations due to the beginning of plastic flow. In parallel with

the evolution of plastic deformations, an evolution of the yield stress is also observed, a phenomenon called hardening.
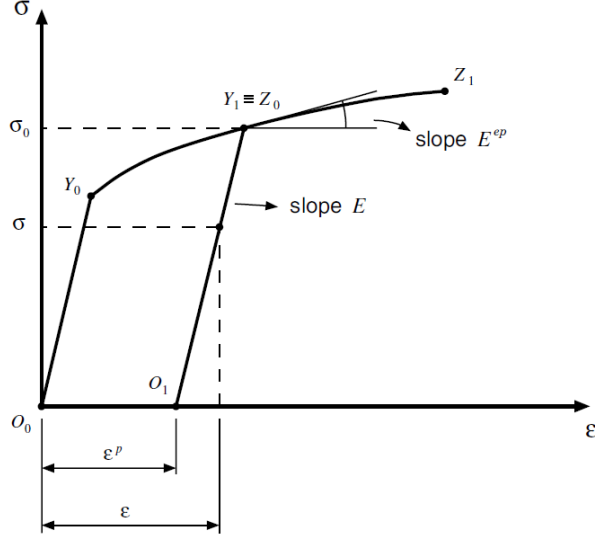
Figure 3.1: Stress-strain curve for a ductile material.

As Neto et al. [2008] shows, the basic premise in the study of plasticity in small deformations is the decomposition of the total deformation (ϵ) as the sum of an elastic component ϵ^e (also known as reversible deformation) and another plastic component (ϵ^p), such as present in eq. 3.1.

$$\epsilon = \epsilon^e + \epsilon^p \tag{3.1}$$

3.1.1 Von Mises criterion

The von Mises criterion suggests that the yield of the materials starts when the second invariant ($J2$) of the deviatoric stress reaches a critical value k. For this reason, this criterion is also commonly known as $J2$ plasticity theory or $J2$ flow theory.

The starting point for the development of the von Mises criterion considers that the threshold for the occurrence of plasticity is linked to the energy of elastic shear deformation. The elastic energy can be defined, based on the power of internal efforts, such as:

$$W^e = \int_0^t -P_{int}dt' = \int_0^t \boldsymbol{\sigma} : \dot{\boldsymbol{\epsilon}}^e dt' \tag{3.2}$$

Introducing the deviatoric parts of the stress tensor and the elastic strain tensor in the expression of the strain energy presented in eq. 3.2. The part of the energy due to shear for an isotropic elastic material can be determined as shown in eq. 3.3, where G represents

the Coulomb shear modulus of elasticity.

$$W_D^e = \int_0^t \boldsymbol{s} : \dot{\boldsymbol{\epsilon}}^e \, dt' = \frac{\boldsymbol{s} : \boldsymbol{s}}{4G} \tag{3.3}$$

The von Mises criterion proposes that the shear energy must be less than a threshold denominated by W_y in order to remain in the elastic domain of the material.

$$W_D^e \leq W_y \tag{3.4}$$

Shear energies above this threshold, therefore, cause the presence of plastic deformations.

Mathematically, the plasticity rule for the von Mises criterion can be expressed by eq. 3.5, where, k represents the yield stress of the material in a pure shear condition.

$$f(J_2) = \sqrt{J_2} - k = 0 \tag{3.5}$$

3.1.2 Tresca Criteria

The criterion postulated by Tresca shows that the plasticity in a deformed body is reached when the absolute value of the shear stress reaches a critical value T. This condition can be expressed mathematically by:

$$\max_{\substack{i,j \in \{1,2,3\} \\ i \neq j}} |\sigma_i - \sigma_j| \leq \sigma_Y \tag{3.6}$$

Where the maximum shear stress can be obtained from the principal stresses:

$$|\sigma_{max}| = \frac{1}{2} \max_{\substack{i,j \in \{1,2,3\} \\ i \neq j}} |\sigma_i - \sigma_j| \tag{3.7}$$

In the Tresca criterion, for a given state of stresses, the elastic limit occurs when the stress levels are within the failure surface, otherwise, the behavior is called elastoplastic.

3.1.3 Johnson-Cook Constitutive Model

The constitutive model presented by Johnson-Cook is a model based on Mises plasticity and expresses the stress in the plastic regime as the dissociated product from three different terms: plastic deformation (isotropic hardening), deformation rate (sensitivity to the rate of force application) and temperature (softening by thermal effects).

$$\sigma_Y = [A + B(\epsilon^p)^n] \left[1 + Cln\left(\frac{\dot{\epsilon}^p}{\dot{\epsilon}_0}\right) \right] (1 - \hat{\theta}^m) \tag{3.8}$$

$[A, B, n, C, \dot{\epsilon}_0, m]$ are parameters of the material, found experimentally. A, B and n represent the quasi-static behavior and C the plastic effects (it is worth remembering that the strain rate tends to increase as the loading application speed increases). The third part of the Johnson Cook equation contemplates the effects of temperature. $\hat{\theta}^m$ is a relationship between the melting temperature of the material and the ambient temperature, m the softening exponent, ϵ_0 the effective plastic deformation and $\dot{\epsilon}^p$ the time derivative of the effective plastic deformation.

As the constitutive model of Johnson-Cook is a model based on an isotropic hardening, such model does not present good predictions for the response of thermoplastic polymers under cyclic loads. In the case of the application of a monotonic compression load, Bergstrom [2015] states that this model shows good agreement with the experimental behavior for several materials, however the same study pointed out that the behavior predicted after the removal of the load significantly overlaps the residual deformation.

3.1.4 Drucker-Prager Constitutive Model

The Drucker-Prager failure criterion consists of a plasticity model with isotropic hardening, developed especially for the prediction of granular solids, but that can also be used to describe the behavior of several thermoplastic polymers. Due to its formulation being based on a pressure-dependent yield stress, it can represent different yield stresses for tensile and compression (in fact, several thermoplastic polymers are dependent on yield strength in relation to pressure).

This constitutive model is based on the modification of the criterion presented by Von Mises, in which the sensitivity of hydrostatic pressure is introduced in the mathematical formulation. The criterion defines that the limit of the elastic zone is reached when a critical combination between the shear stress reaches a certain magnitude. This relationship is represented, due to the isotropy of the material, by the following equation:

$$\sqrt{J_2} + \eta \frac{I_1}{3} = \overline{c} \tag{3.9}$$

where, n and $\overline{c}$ represent parameters of the material. In the specific case of n equal to zero, the cylinder of the Von Mises criterion is reached.

Like the Johnson-Cook model, the Drucker Prager model also has limitations as it fails to accurately describe the discharge response in many thermoplastic polymers.

3.2 Arruda-Boyce model

The eight-chain model developed by Arruda-Boyce is a hyperelastic model motivated by the deformation behavior of the elastomer microstructure and presented itself as a first model before the development of the elastic-viscoplastic model. The main assumption is based on the fact that the macromolecules are located, on average, along the diagonals of a unit cell positioned in the principal stretches, as shown in Figure 3.2.
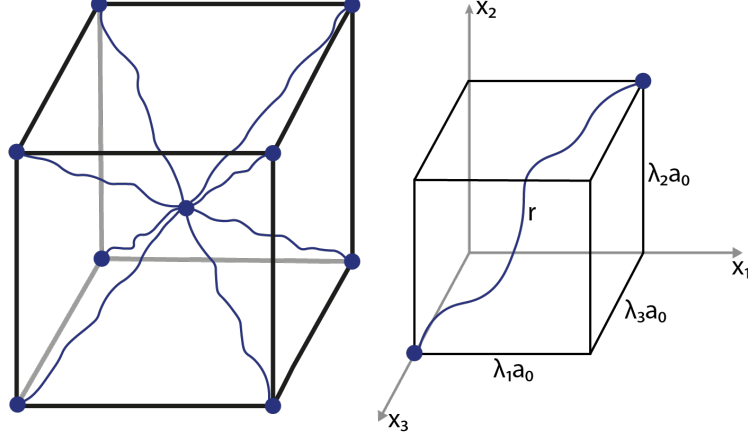
Figure 3.2: Arruda-Boyce 8-chain model: representative positioning of macromolecules.

Considering the figure 3.2, it is possible to identify that the lateral lengths of the unit cells in the reference state are indicated by a_0 and the length of each non-deformed chain by r_0, that is, $r_0 = a_0\sqrt{3}$. Furthermore, it is also considered that each macromolecule is freely articulated with n rigid links, each of length L. For this model, the average point-to-point distance, in the absence of external force, is equal to $L\sqrt{n}$. Defining λ_1, λ_2 and λ_3 as the principal distortion stretches applied, the effective length of the distortion chain becomes:

$$r = a_0\sqrt{\lambda_1^2 + \lambda_2^2 + \lambda_3^2} \tag{3.10}$$

The average of the principal distortion stretches applied allows to determine that:

$$\lambda_{chain} = \left[\frac{\lambda_1^2 + \lambda_2^2 + \lambda_3^2}{3}\right]^{\frac{1}{2}} = \sqrt{\frac{tr[\boldsymbol{C}^*]}{3}} = \sqrt{\frac{tr[\boldsymbol{B}^*]}{3}} = \sqrt{\frac{tr[\boldsymbol{I_1}^*]}{3}} \tag{3.11}$$

where, $\boldsymbol{B}^* = J^{-\frac{2}{3}}\boldsymbol{B}$. In this equation, it can be inferred that the distortion elongation chain is, in fact, a function only of the first invariant called $\boldsymbol{I_1}^*$.

Physically, the eight-chain model is a model defined as an isotropic thermoplastic model, whose free Helmholtz energy per unit of reference volume (Ψ) is dependent on the temperature θ_0, $\sqrt{tr[\boldsymbol{B}^*]/3}$ and the Jacobian.

The Arruda-Boyce elastic-viscoplastic model is a model used for the prediction of both

glassy and thermoplastic polymers. This model was developed to predict large deformations, time dependence and possible temperature dependence. The behavior of the polymer class where the Arruda-Boyce elastic-viscoplastic model is applied is briefly constituted by linear phase, yield, and non-linear hardening.

In the structure of the Arruda-Boyce elastic-viscoplastic model, the total deformation gradient is decomposed into two components, one elastic and one plastic, following eq. 3.12 and presented by Kroner [1959] and Lee [1969]. The figure 3.3 shows a one-dimensional rheological representation, where it is possible to interpret the decomposition of the deformation gradient tensor as two networks acting in series, that is, one network representing an elastic phase and the other a viscoplastic phase .
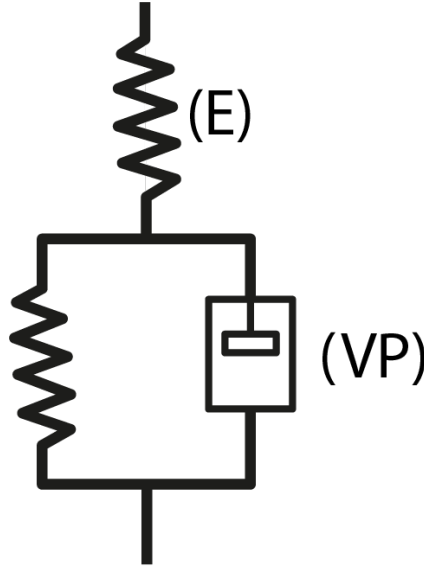
Figure 3.3: One-dimensional rheological representation - Arruda-Boyce model.

Using the decomposition of the deformation gradient, it is possible to determine the Cauchy Stress from an elastic linear relationship, where $\boldsymbol{E}^e$ is the logarithm of the left stretch tensor $ln(\boldsymbol{V}^e)$; μ^e and λ^e are the Lamé constants related to the elastic material properties.

$$\boldsymbol{T}^e = \frac{1}{J^e}(2\mu^e \boldsymbol{E}^e + \lambda^e tr[\boldsymbol{E}^e]\boldsymbol{I}) \tag{3.12}$$

The stress that drives the plastic flow (viscoplastic stress) is given by the tensorial difference between the linear elastic relation and the BackStress, as:

$$\boldsymbol{T}^{vp} = \boldsymbol{T}^e - \frac{1}{J^e}\boldsymbol{T}^e \boldsymbol{T}_B \boldsymbol{T}^{e^T} \tag{3.13}$$

The Arruda-Boyce elastic-viscoplastic model is developed from an approach of statisti-

cal mechanics, more precisely the application of Gaussian statistics, for the description of forces in a deformed polymeric network. The application of a Gaussian statistic produces deformation energies, where λ represents the extensions of the fibers and G the rubbery modulus in function of the chain density n, Boltzmann constant K and the temperature θ.

$$W = \frac{1}{2}(\lambda_1^2 + \lambda_2^2 + \lambda_3^2 - 3), \; G = nK\theta \tag{3.14}$$

Previously to the work proposed by Arruda-Boyce, there are works related to the construction of networks from chains described by Gaussian statistics or by modified Gaussian statistics in order to evaluate stretches larger than those allowed by the Gaussian mathematical assumptions, as present by Wang and Guth [1952] and Treloar [1946]. These models have in common the use of two parameters, the rubbery modulus G and the λ_{chain} defined as the elongation value of the chain when the length reaches its maximum extension state. The stretch of the chain is determined by the current length divided by the initial length, as shown below:

$$\lambda_{chain} = \frac{r_{chain}}{r_0} \tag{3.15}$$

The initial length of the chain is obtained through the theory called by Random Walk statistics as:

$$r_0 = \sqrt{N}l \tag{3.16}$$

Thus, for the total length $r_L = lN$, the locking Stretch becomes:

$$\lambda_L = \frac{r_L}{r_0} = \sqrt{N} \tag{3.17}$$

According to the statistical mechanics approach to rubber elasticity, the chain segment between chemical cross-links can be modeled with a number N of rigid links equal to length 1. The rigid link is the length of the real chain segment on the rigid body movement in response to an imposed deformation. Depending on the rubber material, the rigid link may span several repeated molecular units. The initial length of the chain is obtained from a random walk consideration of N steps of length 1 (Random Walk), and is denominated by r_0, as shown in eq. 3.16.

The limiting chain extensibility, defined as the final length divided by the initial length, is provided in terms of the statistical parameters $\lambda_L = \sqrt{N}$. At any chain length value, the most likely distribution of rigid links in relation to the chain-length vector can be determined.

According to Kuhn and Grun [1942] about the use of Langevin, the probability of the distribution of the most likely connection angle given a vector length, is equal to the length of the vector r_{chain}. In this sense, Kuhn and Grun [1942] obtained an expression for the

probability density function of the chain lengths and, later, for the configurational entropy of a stretched chain of length r_0.

$$s_{chain} = k \left[c - N \left(\frac{r_{chain}}{NL} \right) \beta + ln \left(\frac{\beta}{sinh(\beta)} \right) \right] \qquad (3.18)$$

where c is a constant and β is the inverse of the Langevin function $\beta = L_l^{-1} [\frac{r_{chain}}{Nl}]$, for a Langevin function defined by $\mathcal{L}^{-1}(\beta) = coth(\beta) - \frac{1}{\beta}$

The use of the mathematical model proposed by Langevin explains the extensibility of the limiting chain based on the proportionality of the deformation in relation to the change in entropy by stretching the chains of an unstretched state.

The energy term can be written as a function of the current length as shown in eq. 3.19, where n is the chain density and c' is a combination of constants.

$$W = nK\Theta N \left[\frac{r_{chain}}{Nl} \beta + \ln \left(\frac{\beta}{\sinh(\beta)} \right) \right] - \Theta c' \qquad (3.19)$$

In the developed formulation, the material is considered incompressible, and its principal stresses can be determined from the work of deformation to an arbitrary pressure p and the principal stretches denominated by λ_i.

$$\sigma_i = \lambda_i \frac{dW}{d\lambda_i} + p \qquad (3.20)$$

The equation 3.21 presents a different writing for the stress-stretch relationship, in terms of the differences between two principal stresses in order to eliminate the pressure term.

$$\sigma_1 - \sigma_2 = \lambda_1 \frac{dW}{d\lambda_1} - \lambda_2 \frac{dW}{d\lambda_2} \qquad (3.21)$$

Considering the equation 3.21 and deriving the function presented in 3.19 in relation to λ_1 and λ_2, it is possible to determine that the stress-stretch can be rewritten as:

$$\sigma_1 - \sigma_2 = \frac{nk\Theta}{3} N L_l^{-1} \left[\frac{\lambda_{chain}}{\sqrt{N}} \right] \frac{\lambda_1^2 - \lambda_2^2}{\lambda_{chain}} \qquad (3.22)$$

Briefly, the term obtained in the above equation can be referred as the stress in the Langevin spring and can finally be represented as:

$$\boldsymbol{T}_B = C_r \sqrt{N} L_l^{-1} \left[\frac{\lambda_{chain}}{\sqrt{N}} \right] \frac{\Lambda_i^{p2} - \frac{1}{3} I_1}{\lambda_{chain}} \qquad (3.23)$$

Where $\boldsymbol{T}_B$ is a stress tensor depends on the inelastic deformation, C_r represents the rubbery modulus, which can be determined by $C_r = nk\theta$ and Λ_i^p are the principal stretches given by the eigenvalues of the inelastic stretch tensor, something discussed in section 2.1.4.

The term referring to the nonlinear hardening stress can be represented differently as presented by Mulliken-Boyce (eq. 3.38), where it is not necessary to determine the eigenvalues and eigenvectors of the stretching tensor, something that can be computationally costly in simulation of explicit integration due to the magnitude of time increment.

$$\boldsymbol{T}_B = \frac{C_r}{\lambda_{chain}^p} \frac{\mathcal{L}^{-1}(\lambda_{chain}^p/N)}{\mathcal{L}^{-1}(1/N)} \boldsymbol{B}_{dev}^p \tag{3.24}$$

Dealing specifically with the viscoplastic term of the Arruda-Boyce model, it appears that after obtaining the linear stress term and the BackStress, it is possible to determine the plastic strain flow tensor $\boldsymbol{D}^p$. Therefore, it is necessary to determine the deviatoric part of the viscoplastic stress (3.13), since it is the part responsible for plastic deformations.

$$\boldsymbol{T}_{dev}^{vp} = \boldsymbol{T}^{vp} - \frac{1}{3}tr[\boldsymbol{T}^{vp}] \tag{3.25}$$

In view of the deviatoric part of the viscoplastic term, the equivalent shear strength can be obtained as shown in eq. 3.26 and the flow law by eq. 3.27. To obtain the flow law, it is assumed that the plastic rotation rate tensor is a null tensor, that is, it is considered exclusively a kinematic strain rate.

$$\tau = \sqrt{\frac{\boldsymbol{T}_{dev}^{vp} : \boldsymbol{T}_{dev}^{vp}}{2}} \tag{3.26}$$

$$\boldsymbol{D}^p = \dot{\gamma}^p \boldsymbol{N} \tag{3.27}$$

where, $\boldsymbol{N}$ represents a normalized tensor aligned with the deviatoric stress tensor and is determined by:

$$\boldsymbol{N} = \frac{\boldsymbol{T}_{dev}^{vp}}{\sqrt{2}\tau} \tag{3.28}$$

In the original Arruda-Boyce study, the plastic flow rate is given by the equation presented in eq. 3.29, where $\dot{\gamma}_0$, A and s are material constants. Eq. 3.30 presents the stress softening term through the evolution to the s athermic shear. In this equation, the terms h and S_{ss} are also configured as material constants.

$$\dot{\gamma}^p = \dot{\gamma}_0 \exp\left[-\frac{As}{k\theta}\left(1 - \left(\frac{\tau}{s}\right)^{5/6}\right)\right] \tag{3.29}$$

$$\dot{s} = h \left[1 - \frac{s}{S_{ss}} \right] \dot{\gamma}^p \qquad (3.30)$$

3.3 Mulliken-Boyce Model

Mullike-Boyce's numerical model presents itself as an evolution of the model presented by Arruda and Boyce [1993]. In this model, instead of using one viscoplastic network, there are two networks in parallel called by activated molecular processes, each with their respective elastic and viscoplastic properties, as represented in the figure 3.4.

The basic principle present in the viscoplastic behavior of the material is based on the flow theory of Ree-Eyring, where, it is shown that there are the presence of several active processes that can contribute to the general behavior of the material under deformations. Physically, such processes can be understood as movements at molecular levels, presenting a threshold, determined by temperature and strain rate, below which, the associated molecular movement is restricted. Such a restriction can be understood as the resistance to deformation of the material.
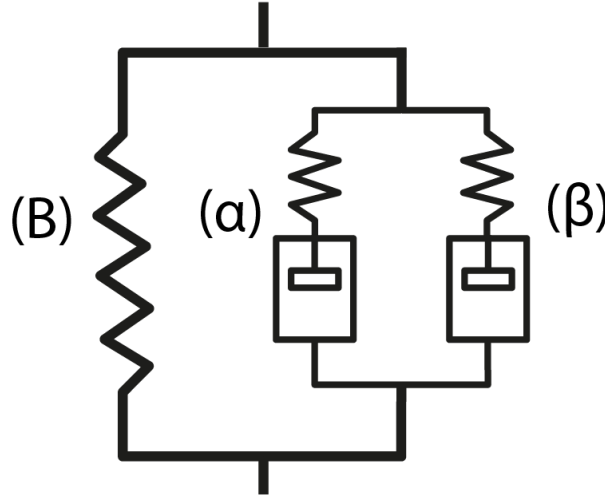
Figure 3.4: One-dimensional rheological representation - Mulliken-Boyce model

The intermolecular contribution to the stress state of α and β chains can be obtained by the constitutive laws of springs in a linear-elastic domain, as shown in 3.31. It is noteworthy that the real stresses are obtained from Hencky's hyperelastic behavior, as discussed in section 2.1.6.

$$\boldsymbol{T}_{A,\alpha} = \tfrac{1}{J_\alpha} \mathcal{L}_\alpha^e [ln(\boldsymbol{U}_{A,\alpha}^e)]$$

$$\boldsymbol{T}_{A,\beta} = \tfrac{1}{J_\beta} \mathcal{L}_\beta^e [ln(\boldsymbol{U}_{A,\beta}^e)]$$

$$(3.31)$$

Since the rheological model is represented by two viscoplastic components in parallel with a non-linear entropic hardening component, referring to the BackStress, it is possible to show that, under the application of any load, all components are subjected to the same deformation, therefore:

$$\boldsymbol{F}_{A,\alpha} = \boldsymbol{F}_{A,\beta} = \boldsymbol{F}_B = \boldsymbol{F} \tag{3.32}$$

As shown in eq. 2.12, the deformations of α and β contributions can be determined by the following property:

$$\boldsymbol{F}_{A,\alpha} = \boldsymbol{F}^e_{A,\alpha}\boldsymbol{F}^p_{A,\alpha}$$
$$\boldsymbol{F}_{A,\beta} = \boldsymbol{F}^e_{A,\beta}\boldsymbol{F}^p_{A,\beta} \tag{3.33}$$

Conducting stresses are used to specify the directions of the tensors $\boldsymbol{F}^p_{A,\alpha}$, $\boldsymbol{F}^e_{A,\beta}$ and plastic flow, as presented in the equation 3.34. $\boldsymbol{T}'_{A,\alpha}$ and $\boldsymbol{T}'_{A,\beta}$ represent the deviatoric parts of $\boldsymbol{T}_{A,\alpha}$ e $\boldsymbol{T}_{A,\beta}$, respectively.

$$\boldsymbol{N}_\alpha = \frac{1}{\sqrt{2}\tau_\alpha}\boldsymbol{T}'_{A,\alpha}$$
$$\boldsymbol{N}_\beta = \frac{1}{\sqrt{2}\tau_\beta}\boldsymbol{T}'_{A,\beta} \tag{3.34}$$

The effective equivalent shear stress is given by:

$$\tau_\alpha = \sqrt{\tfrac{1}{2}(\boldsymbol{T}'_{A,\alpha} : \boldsymbol{T}'_{A,\alpha})}$$
$$\tau_\beta = \sqrt{\tfrac{1}{2}(\boldsymbol{T}'_{A,\beta} : \boldsymbol{T}'_{A,\beta})} \tag{3.35}$$

Finally, the two constitutive laws for viscoplastic behavior of α and β chains are described as:

$$\dot{\gamma}^p_\alpha = \dot{\gamma}^p_{0,\alpha}exp\left[-\frac{\Delta G_\alpha}{k\theta}\left(1 - \frac{\tau_\alpha}{s_\alpha + \alpha_{p,\alpha}p}\right)\right]$$
$$\dot{\gamma}^p_\beta = \dot{\gamma}^p_{0,\beta}exp\left[-\frac{\Delta G_\beta}{k\theta}\left(1 - \frac{\tau_\beta}{s_\beta + \alpha_{p,\beta}p}\right)\right] \tag{3.36}$$

in the eq. 3.36, $\dot{\gamma}^p_\alpha$ e $\dot{\gamma}^p_\beta$ represent the pre-exponential factors, ΔG_α and ΔG_β the activation energy, p the pressure; $\alpha_{p,\alpha}$ and $\alpha_{p,\beta}$ the pressure coefficient. The internal variable s_α s_β describes the athermic shear strength and respects the relationships presented below, where h_α e h_β represents the softening slope and s_{ss} is called the preferred state.

$$s_{0,\alpha} \equiv \frac{0,077\mu_\alpha}{1-\nu_\alpha}$$

$$\dot{s}_\alpha = h_\alpha \left(1 - \frac{s_\alpha}{s_{ss}}\right) \dot{\gamma}_\alpha^p$$

$$s_{0,\beta} \equiv \frac{0,077\mu_\beta}{1-\nu_\beta}$$ (3.37)

$$\dot{s}_\beta = h_\beta \left(1 - \frac{s_\beta}{s_{ss}}\right) \dot{\gamma}_\beta^p$$

In the Mulliken-Boyce model, the nonlinear hardening stress component (*BackStress*) due to the entropic resistance of the molecular alignment is defined as:

$$\boldsymbol{T}_B = \frac{C_R}{3} \frac{\sqrt{N}}{\lambda_{chain}^p} \mathcal{L}^{-1} \left(\frac{\lambda_{chain}^p}{\sqrt{N}}\right) \boldsymbol{B^*}_{dev}$$ (3.38)

where, $\boldsymbol{B^*}_{dev}$ is the deviatoric part of the left Cauchy-green Tensor.

Ultimately, the total stress in the polymer is given by the tensorial sum of the contributions of the intermolecular stresses α and β, as well as the nonlinear hardening stress (BackStress):

$$\boldsymbol{T} = \boldsymbol{T}_B + \boldsymbol{T}_{A,\alpha} + \boldsymbol{T}_{A,\beta}$$ (3.39)

3.3.1 Implementation and Numerical Calibration of an Elastic-viscoplastic Model for Thermoplastic Polymers

The numerical model presented by Mulliken and Boyce [2006] was implemented through the use of subroutines in VUMAT in the commercial software in finite element ABAQUS®, an interface present in ABAQUS®/explicit, which allows the implementation of constitutive equations through tensorial definitions, defined by the user.

UMAT subroutines are also intended for the same purpose, however, unlike VUMAT subroutines, it requires updating the tangent module at each time increment, which can be considered complex when using constitutive equations, in which the derivative of the stress tensor increment in relation to the strain deformation tensor is unknown or costly to obtain. According to Vergard [2014], for the implementation of the Mulliken-Boyce model with an implicit integration (UMAT), a viable alternative would be the use of the perturbation method.

Another requirement for using VUMAT is to transform rate equations into incremental equations using a suitable integration procedure, such as Euler method or midpoint method. Such methods are reasonably simple to be implemented, however, they present a stability

limit, that is, deformation increments above a certain threshold cause a non-convergence of the step. Usually, the stability threshold of the deformation increment is less than the magnitude of the deformation at the elastic threshold.

The Mulliken-Boyce model, as previously presented, requires the definition of 16 material parameters referring to the two chains that represent the intermolecular contributions and the non-linear hardening contribution chain, as present in the section 3.3. Table 3.1 shows all the parameters necessary to define the relevant material properties.
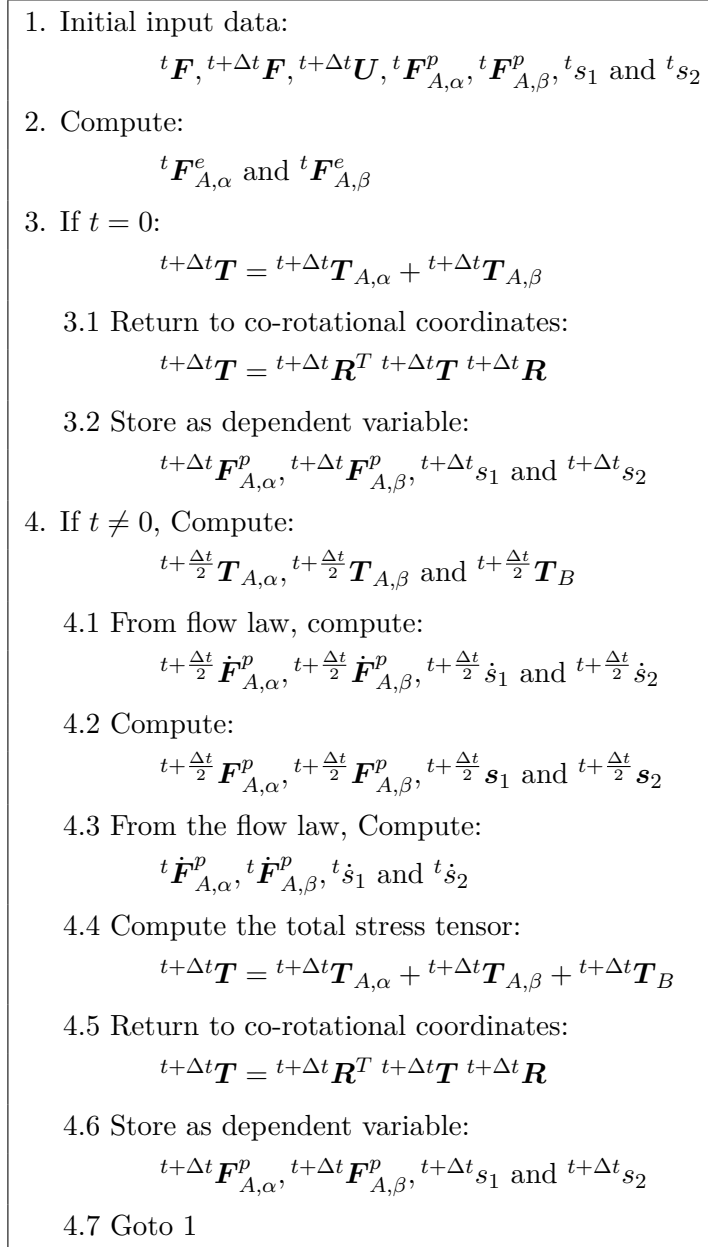
Table 3.1: Mulliken-Boyce model parameters.

Symbol	Parameter
E_α	Young's modulus - alpha chain
E_β	Young's modulus - beta chain
ν	Poisson's ratio
$\dot{\gamma}_{0,\alpha}^{p}$	Pre-exponential factor - alpha chain
$\dot{\gamma}_{0,\beta}^{p}$	Pre-exponential factor - beta chain
$\alpha_{p,\alpha}$	Pressure coefficient - alpha chain
$\alpha_{p,\beta}$	Pressure coefficient - beta chain
ΔG_α	Activation energy - alpha chain
ΔG_β	Activation energy - beta chain
h_α	Softening slope - alpha chain
h_β	Softening slope - beta chain
s_{ss}	Preferred states of athermal shear strengths
C_r	Rubbery modulus
N	Limiting chain extensibility
k	Boltzmann Constant
Θ	Temperature

The implementation of the Mulliken-Boyce model follows the flowchart of the table 3.2. For this, a main subroutine was developed containing the main steps for the implementation of the numerical model. The presence of auxiliary scripts such as: definition of the flow equation, determination of the contribution of non-linear hardening and tensor calculations were implemented as auxiliary subroutines, being called whenever necessary.

In the main subroutine there is the definition of the basic properties relevant to the definition of the material (table 3.1), as well as the input of the variables defined as dependent state variables, better defined later on. The basic operation of the main subroutine is based on the input of the strain gradient in t and $t + \delta t$ and the right stretch tensor $\boldsymbol{U}$ in $t + \Delta t$. Given these input data, tensor calculations are performed during the subroutine, in order to determine the Cauchy stress tensor. All the tensor calculations necessary for the definition of additional tensors were presented in the chapter 2.1.

Table 3.2: Flowchart for implementing the Mulliken-Boyce model: Main subroutine.

1. Initial input data:
$${}^{t}\boldsymbol{F}, {}^{t+\Delta t}\boldsymbol{F}, {}^{t+\Delta t}\boldsymbol{U}, {}^{t}\boldsymbol{F}^{p}_{A,\alpha}, {}^{t}\boldsymbol{F}^{p}_{A,\beta}, {}^{t}s_1 \text{ and } {}^{t}s_2$$

2. Compute:
$${}^{t}\boldsymbol{F}^{e}_{A,\alpha} \text{ and } {}^{t}\boldsymbol{F}^{e}_{A,\beta}$$

3. If $t = 0$:
$${}^{t+\Delta t}\boldsymbol{T} = {}^{t+\Delta t}\boldsymbol{T}_{A,\alpha} + {}^{t+\Delta t}\boldsymbol{T}_{A,\beta}$$

   3.1 Return to co-rotational coordinates:
$${}^{t+\Delta t}\boldsymbol{T} = {}^{t+\Delta t}\boldsymbol{R}^{T} \, {}^{t+\Delta t}\boldsymbol{T} \, {}^{t+\Delta t}\boldsymbol{R}$$

   3.2 Store as dependent variable:
$${}^{t+\Delta t}\boldsymbol{F}^{p}_{A,\alpha}, {}^{t+\Delta t}\boldsymbol{F}^{p}_{A,\beta}, {}^{t+\Delta t}s_1 \text{ and } {}^{t+\Delta t}s_2$$

4. If $t \neq 0$, Compute:
$${}^{t+\frac{\Delta t}{2}}\boldsymbol{T}_{A,\alpha}, {}^{t+\frac{\Delta t}{2}}\boldsymbol{T}_{A,\beta} \text{ and } {}^{t+\frac{\Delta t}{2}}\boldsymbol{T}_{B}$$

   4.1 From flow law, compute:
$${}^{t+\frac{\Delta t}{2}}\dot{\boldsymbol{F}}^{p}_{A,\alpha}, {}^{t+\frac{\Delta t}{2}}\dot{\boldsymbol{F}}^{p}_{A,\beta}, {}^{t+\frac{\Delta t}{2}}\dot{s}_1 \text{ and } {}^{t+\frac{\Delta t}{2}}\dot{s}_2$$

   4.2 Compute:
$${}^{t+\frac{\Delta t}{2}}\boldsymbol{F}^{p}_{A,\alpha}, {}^{t+\frac{\Delta t}{2}}\boldsymbol{F}^{p}_{A,\beta}, {}^{t+\frac{\Delta t}{2}}s_1 \text{ and } {}^{t+\frac{\Delta t}{2}}s_2$$

   4.3 From the flow law, Compute:
$${}^{t}\dot{\boldsymbol{F}}^{p}_{A,\alpha}, {}^{t}\dot{\boldsymbol{F}}^{p}_{A,\beta}, {}^{t}\dot{s}_1 \text{ and } {}^{t}\dot{s}_2$$

   4.4 Compute the total stress tensor:
$${}^{t+\Delta t}\boldsymbol{T} = {}^{t+\Delta t}\boldsymbol{T}_{A,\alpha} + {}^{t+\Delta t}\boldsymbol{T}_{A,\beta} + {}^{t+\Delta t}\boldsymbol{T}_{B}$$

   4.5 Return to co-rotational coordinates:
$${}^{t+\Delta t}\boldsymbol{T} = {}^{t+\Delta t}\boldsymbol{R}^{T} \, {}^{t+\Delta t}\boldsymbol{T} \, {}^{t+\Delta t}\boldsymbol{R}$$

   4.6 Store as dependent variable:
$${}^{t+\Delta t}\boldsymbol{F}^{p}_{A,\alpha}, {}^{t+\Delta t}\boldsymbol{F}^{p}_{A,\beta}, {}^{t+\Delta t}s_1 \text{ and } {}^{t+\Delta t}s_2$$

   4.7 Goto 1

Some points of greater relevance present in the main subroutine to be highlighted are: (1) use of the midpoint method as an integration procedure for transforming rate equations into incremental equations and (2) defining the variables to be stored as dependent states, something better explained later.

The flowcharts presented in 3.3 and 3.4 represent the numerical procedures for the plastic flow model and non-linear hardening. Both are part of the main subroutine, being called whenever pertinent.

Table 3.3: Flowchart for implementing the Mulliken-Boyce model: Viscoplastic flow sub-routine.

1. Initial input data: $\boldsymbol{T}^e, p$ and s

2. Compute:
$$\boldsymbol{T}^e_{dev} = \boldsymbol{T}^e - \tfrac{1}{3}tr[\boldsymbol{T}^e]$$

3. Determine the equivalent stress:
$$\tau = \sqrt{\tfrac{1}{2}\left(\boldsymbol{T}^e_{dev} : \boldsymbol{T}^e_{dev}\right)}$$

4. Compute:
$$\boldsymbol{N} = \tfrac{1}{\sqrt{2}\tau}\boldsymbol{T}^e_{dev}$$

5. Compute the constitutive equation for the viscoplastic behavior of the material:
$$\dot{\gamma}^p = \dot{\gamma}^p_0 exp\left[-\tfrac{\Delta G}{k\theta}\left(1 - \tfrac{\tau}{s+\alpha_p p}\right)\right]$$

6. Calculate the plastic flow law:
$$\boldsymbol{D}^p = \dot{\gamma}^p \boldsymbol{N}$$

7. Determine the athermic shear stress flow:
$$\dot{s} = h\left(1 - \tfrac{s}{s_{ss}}\right)\dot{\gamma}^p$$

7. Return: $\boldsymbol{D}^p$ and $\dot{s}$

Table 3.4: Flowchart for implementing the Mulliken-Boyce model: Sub-routine for calculating the nonlinear hardening contribution.

1. Initial input data: $\boldsymbol{F}$

2. Calculate the left Cauchy-Green tensor:
$$\boldsymbol{B} = \boldsymbol{F}\boldsymbol{F}^T$$

3. Determine:
$$\boldsymbol{B}^* = det(\boldsymbol{F})^{-\frac{2}{3}}\boldsymbol{B}$$

4. Compute the deviatoric tensor of $\boldsymbol{B}^*_{dev}$:
$$\boldsymbol{B}^*_{dev} = \boldsymbol{B}^* - \tfrac{1}{3}tr[\boldsymbol{B}^*]$$

5. Calculate the chain elongation lock parameter:
$$\lambda^p_{chain} = \sqrt{\tfrac{tr[\boldsymbol{B}^*]}{3}}$$

6. Determine the Langevin inverse, as:
$$\mathcal{L}^{-1}(\zeta) = cotg(\zeta) - \tfrac{1}{\zeta}, \text{ where, } \zeta = \tfrac{\lambda^p_{chain}}{\sqrt{N}}$$

7. Find the contribution due to nonlinear hardening:
$$\boldsymbol{T}_B = \tfrac{C_R}{3}\tfrac{\sqrt{N}}{\lambda^p_{chain}}\mathcal{L}^{-1}\left(\tfrac{\lambda^p_{chain}}{\sqrt{N}}\right)\boldsymbol{B}^*_{dev}$$

8. Return: $\boldsymbol{T}_B$

3.3.2   Dependent State Variables

To determine the magnitude of plastic deformations of each of the two chains representing the activated molecular processes, it was necessary to store the variables of the plastic deformation gradient of the α and β chains, as well as the athermic shear stress for each chain. This process occurs through the storage of variables such as: dependent state variables, when at each start of time increment, the variables stored in the previous increment can be used as variables in the current increment. It should be noted that the specific storage of the plastic deformation gradient of both chains is not mandatory, the storage of the elastic deformation gradient can also be a strategy adopted.

3.3.3   Numerical Integration Procedure

The integration scheme using the midpoint method used for the rate equation integration procedure was implemented in two different ways, first, for the athermic shear stress rate ($\dot{s}$), the method was applied following the procedure presented in eq. 3.40 (Simo and Hughes [1997]).

$$
{}^{t+\Delta t}x = {}^{t}x + \Delta t \; f\big({}^{t+\frac{\Delta t}{2}}x\big)
$$

$$
{}^{t+\frac{\Delta t}{2}}x = \tfrac{1}{2}\big({}^{t+\Delta t}x + {}^{t}x\big)
$$

$$(3.40)$$

For the numerical integration of the hyperelasticity plastic flow equation, the application of an integration using exponential maps is adequate for the numerical solution of a problem with a defined initial value. Below is the numerical procedure for an exponential mapping of the strain rate tensor.

$$
{}^{t+\frac{\Delta t}{2}}\boldsymbol{F}^p = \exp\left[\left(\tfrac{\Delta t}{2}\right){}^{t}\boldsymbol{W}\right]{}^{t}\boldsymbol{F}^p
$$

$$
{}^{t+\Delta t}\boldsymbol{F}^p = \exp\left[\Delta t \; {}^{t+\frac{\Delta t}{2}}\boldsymbol{W}\right]{}^{t}\boldsymbol{F}^p
$$

$$(3.41)$$

There are different techniques for determining the exponential tensor, among them the Hughes-Winget approach (Neto et al. [2008]) and Padé's approaches (Tomas et al. [2008]) are commonly used for this purpose. The first technique, Hughes-Winget approximation, shows that if the $\Delta t \; {}^{n+\frac{1}{2}}\boldsymbol{W}$ is small enough, that is, small increment of rotations, it can be assumed that the terms of second order or higher orders of $\Delta t \; {}^{n+\frac{1}{2}}\boldsymbol{W}$ can be neglected, so it can be considered that the exponential mapping tensor can be approximated by:

$$
\exp\left[\left(\frac{\Delta t}{2}\right){}^{t+\frac{\Delta t}{2}}\boldsymbol{W}\right] \approx \left[\boldsymbol{I} + \left(\frac{\Delta t}{2}\right){}^{t+\frac{\Delta t}{2}}\boldsymbol{W}\right]
$$

$$(3.42)$$

The second order Padé approximation for exponential mapping can be obtained using the equation presented in eq. 3.43. In this equation, the Padé approximator was expanded around the null tensor

$$P_2^2(\exp(\boldsymbol{x})) = (\boldsymbol{x}^2 + 6\boldsymbol{x} + 12\boldsymbol{I})(\boldsymbol{x}^2 - 6\boldsymbol{x} + 12\boldsymbol{I})^{-1} \tag{3.43}$$

Since explicit integrations require small time increments to satisfy the convergence criterion at each time increment, the use of the Padé approach presents an appropriate conformity for the exponential calculation of the plastic flow. In his studies, Baaser [2004], compares a second-order Padé approximation and the analytical solution of an exponential mapping. The results show that the approximation for a second-order 3X3 tensor is accurate to approximately 10^{-6}.

Evaluations carried out during the implementation of the Mulliken-Boyce elastic-viscoplastic model showed that there are no relevant differences between the two methods presented for performing exponential mapping. Both present a satisfactory approach for this purpose.

3.3.4   Sensitivity Analysis - Mulliken-Boyce Model

A series of changes in the parameters presented in the table 3.1 allow to identify how each parameter of the material interferes in the behavior of the stress-strain curve. Jordan et al. [2008] carried out similar verification by changing the material parameters in order to observe modifications in the behavior curves for compression tests of an epoxy resin.

An evaluation of the order of magnitudes of the parameters presented in the table 3.5 for PC, ABS and a blend of the two materials allowed to infer that the contribution of the second chain to the description of the material's behavior under compression in the test conditions of this study is less relevant than the contribution of the first chain, that is, changes in the parameters of greater relevance of the second chain do not significantly interfere in the description of the material's behavior. However, it is important to note that for cases of high strain rates, the second chain makes a great contribution in the material behavior.

In order to verify the influence of each parameter of the behavior of the numerical curve obtained from the use of the Mulliken-Boyce model, the properties of the PC/ABS 80:20 material present in 3.5 are taken as an example.

With reference to the nominal values presented, changes will be made to these values of ±30%, in order to verify how each parameter interferes in the behavior of the numerical model.

The term referring to the pre-exponential factor interferes in the maximum limit of the

Table 3.5: PC/ABS 80:20 Parameters - Mulliken-Boyce Model

Parameter	Nominal value	Lower limit	Upper limit
E_1	1531,0	-	-
E_2	5,49	-	-
ν	0,38	-	-
$\dot{\gamma}^p_{0,\alpha}$	$2,98 \times 10^{16}$	$2,08 \times 10^{16}$	$3,87 \times 10^{16}$
$\dot{\gamma}^p_{0,\beta}$	$3,36 \times 10^5$	-	-
$\alpha_{p,\alpha}$	0,168	-	-
$\alpha_{p,\beta}$	0,245	-	-
ΔG_α	$4,14 \times 10^{-19}$	$2,90 \times 10^{-19}$	$5,38 \times 10^{-19}$
ΔG_β	$3,77 \times 10^{-20}$	-	-
h_α	300	210	390
h_β	-	-	-
s_{ss}	0,88	-	-
C_r	12,20	8,54	15,86
N	5,29	3,70	6,87
k	$1,38 \times 10^{-23}$	-	-
Θ	296	-	-

linear elastic zone of the curve, so that the greater the magnitude of this parameter, the greater the limit of the elastic region. However only large variations of this parameter cause significant changes. For example, the figure 3.5 shows that changes of 30% in the value of the related parameter do not cause significant changes in the curve. It should also be noted that significant changes to this parameter may cause a change in the tangent module of the curve in the elastic zone.
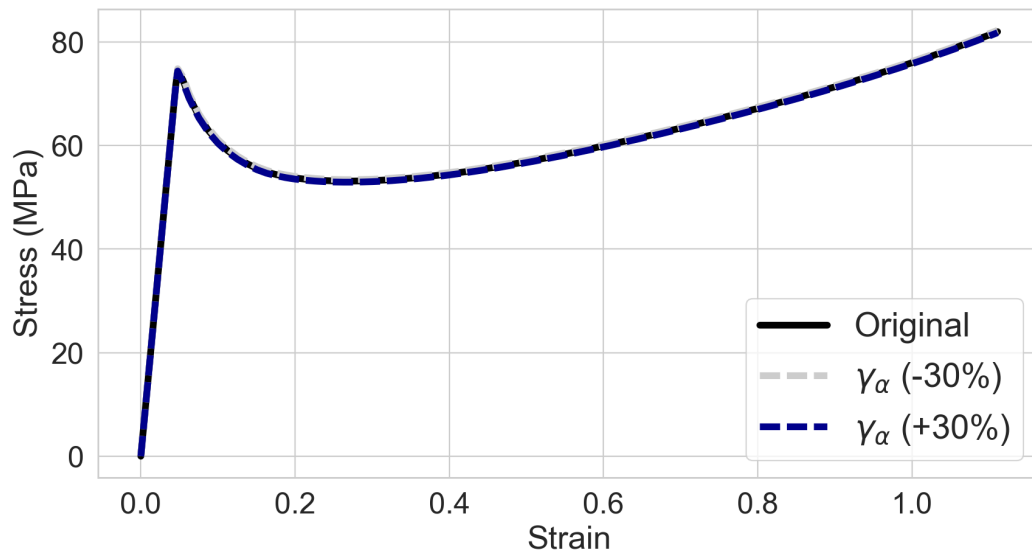
Figure 3.5: Total Cauchy stress: Changes in the pre-exponential factor parameter-alpha chain.

Modifications in the activation energy parameter of the same proportionality as those made in the pre-exponential factor cause more significant changes in the material's elastic zone. The figure 3.5 shows that an increase in this parameter caused a grow in the region of linear elasticity. It is important to note that, in some cases, changes in this parameter can change the behavior of the compression chain to extension or vice versa.
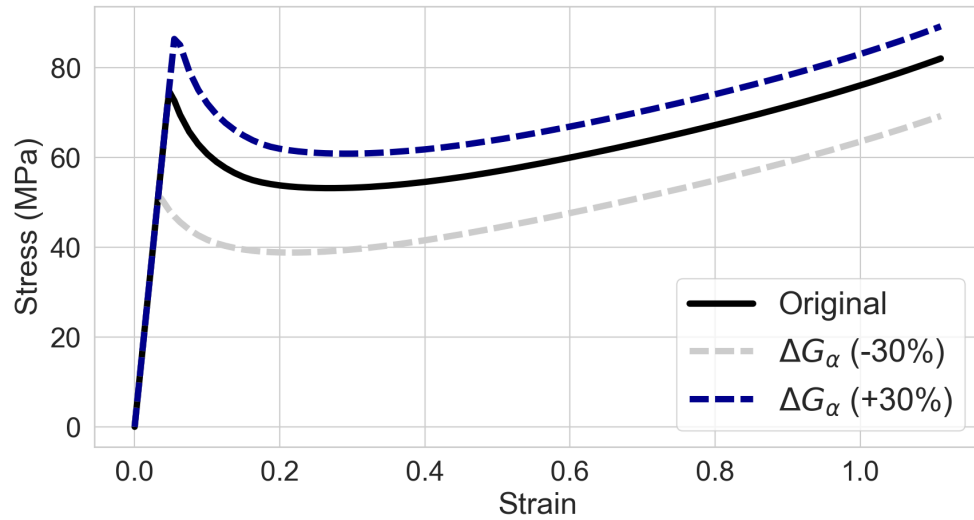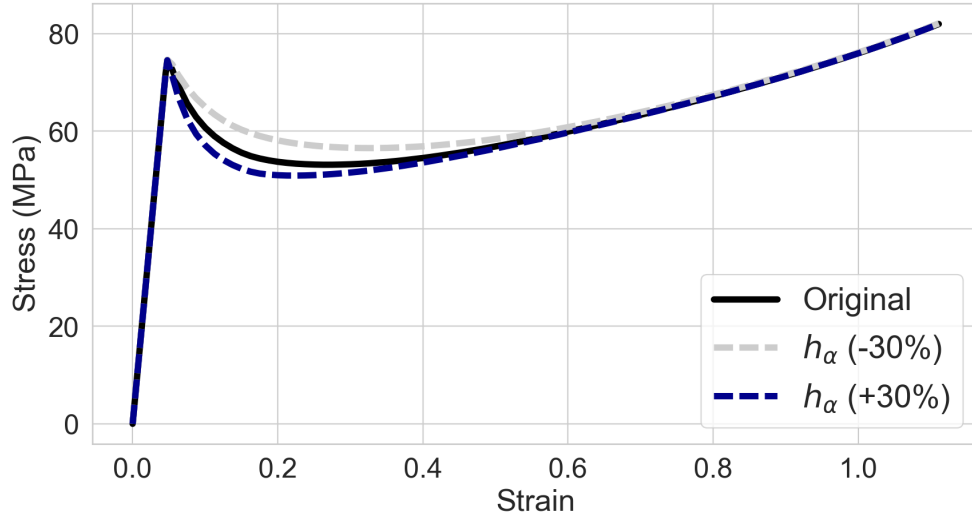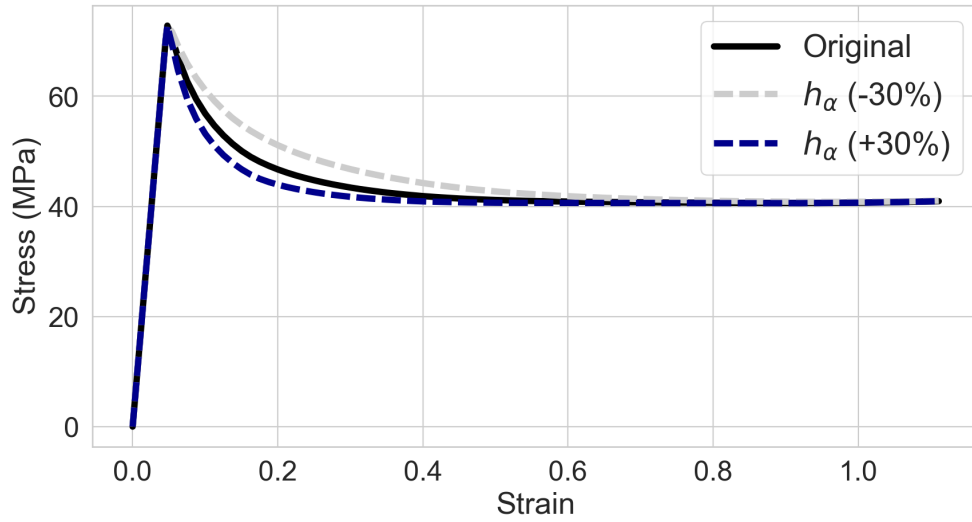

(a) Cauchy Stress - total.
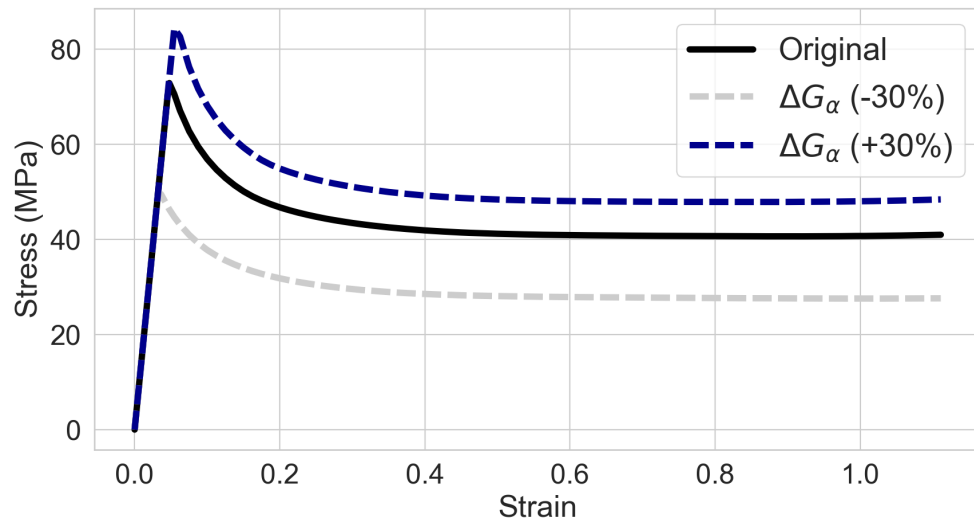
(b) Cauchy Stress- $T_{A,\alpha}$.

Figure 3.6: Changes in the Activation energy parameter - alpha chain.

The softening slope and preferred state parameters, differently from the two parameters presented above, define the behavior of the material yield zone, after the linear elasticity region. The first parameter (softening slope) produces more subtle changes in this zone, while the second parameter causes more significant changes, as it can be seen in figure 3.6.

(a) Cauchy Stress - total.

(b) Cauchy Stress - $T_{A,\alpha}$.

Figure 3.7: Changes in the Softening slope parameter - alpha chain.

The parameters responsible for the region of non-linear hardening, extensibility of the limiting chain and rubbery modulus, act in all regions of the material curve, however more present after the yield zone. The second parameter (rubbery modulus), for the same percentage variation, causes more pronounced changes than the limit chain extensibility parameter. The figures 3.8 and 3.9 show that the extensibility parameter of the limiting chain, unlike the rubbery modulus, allows the description of curves where the stress increase due to hardening it is more expressive for higher levels of strain. For low deformations (after the yielding region), the stress increase occurs more smoothly.
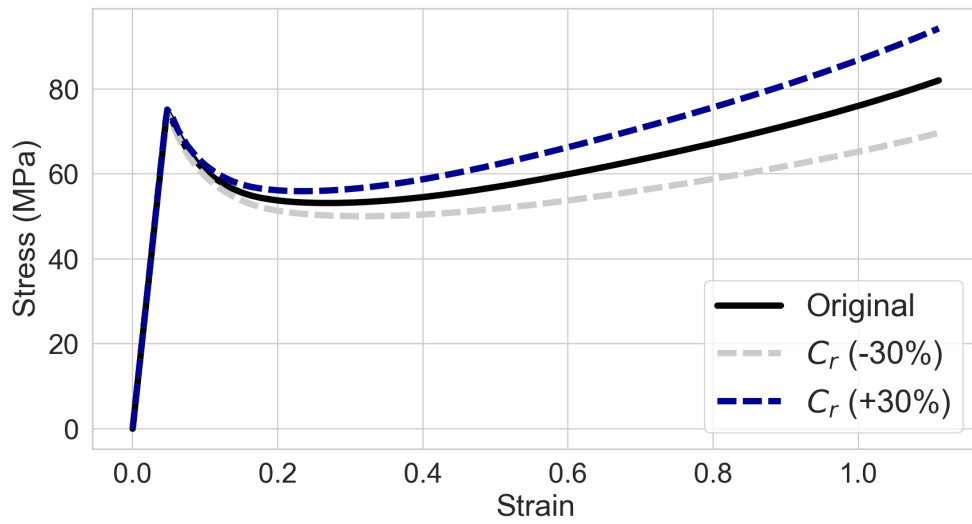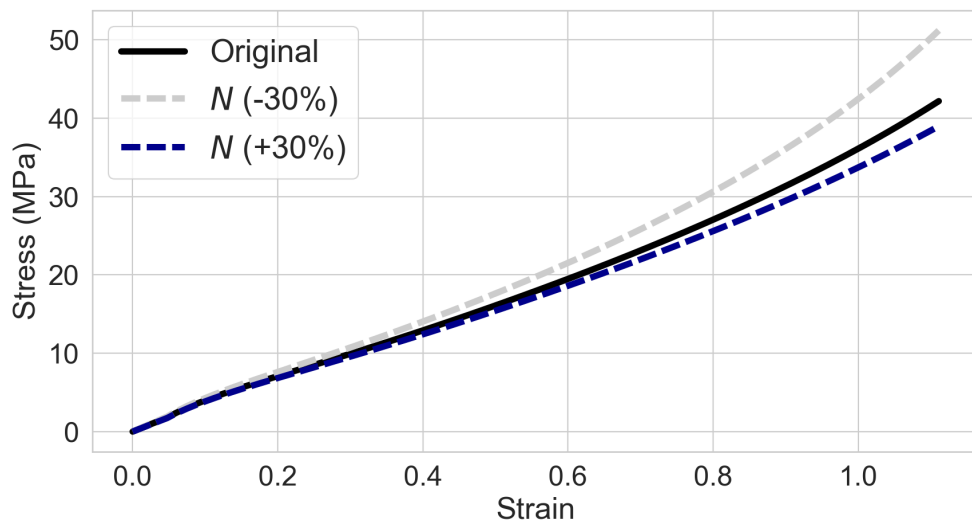
(a) Cauchy Stress - total.
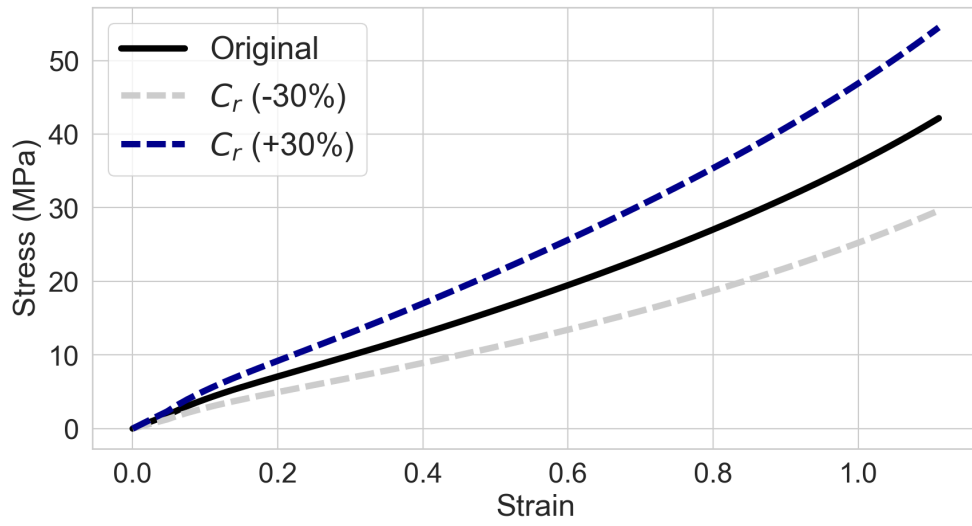
(b) Cauchy Stress - T_B.

Figure 3.8: Changes in the Rubbery modulus parameter - non-linear hardening chain.
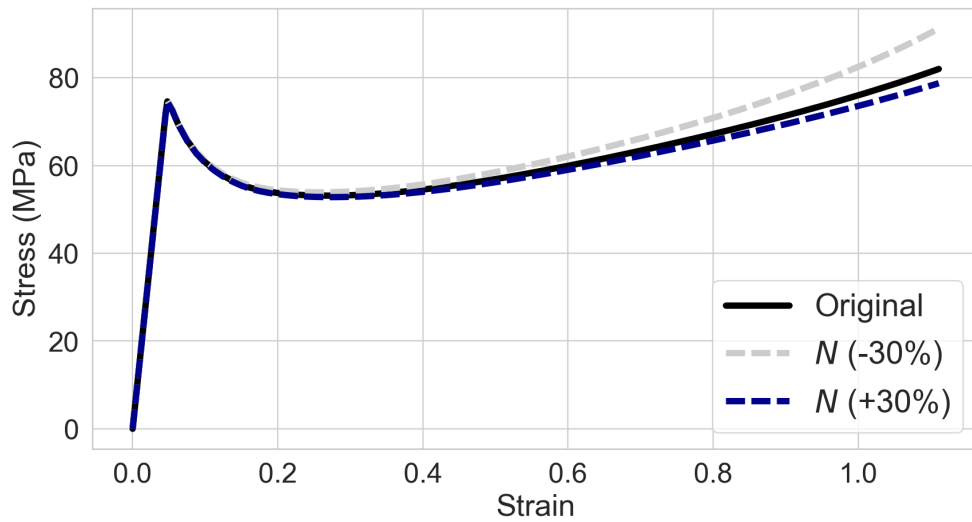
(a) Cauchy Stress - total.

(b) Cauchy Stress - T_B.

Figure 3.9: Changes in the Limiting chain extensibility parameter - non-linear hardening chain

Regarding the model's response to the description of the viscous behavior of the material, the figure 3.10 presents sensitivity analyzes of the imposed strain rates. The responses of the implemented model were consistent with what is physically expected: an increase in the deformation rate caused, mainly, a greater predominance of the elastic zone. Experimental and numerical studies on the behavior of PC, ABS and blends of the two materials present similar behaviors to those found in this sensitivity analysis study (see Wang et al. [2018] and Varghese and Batra [2009]).
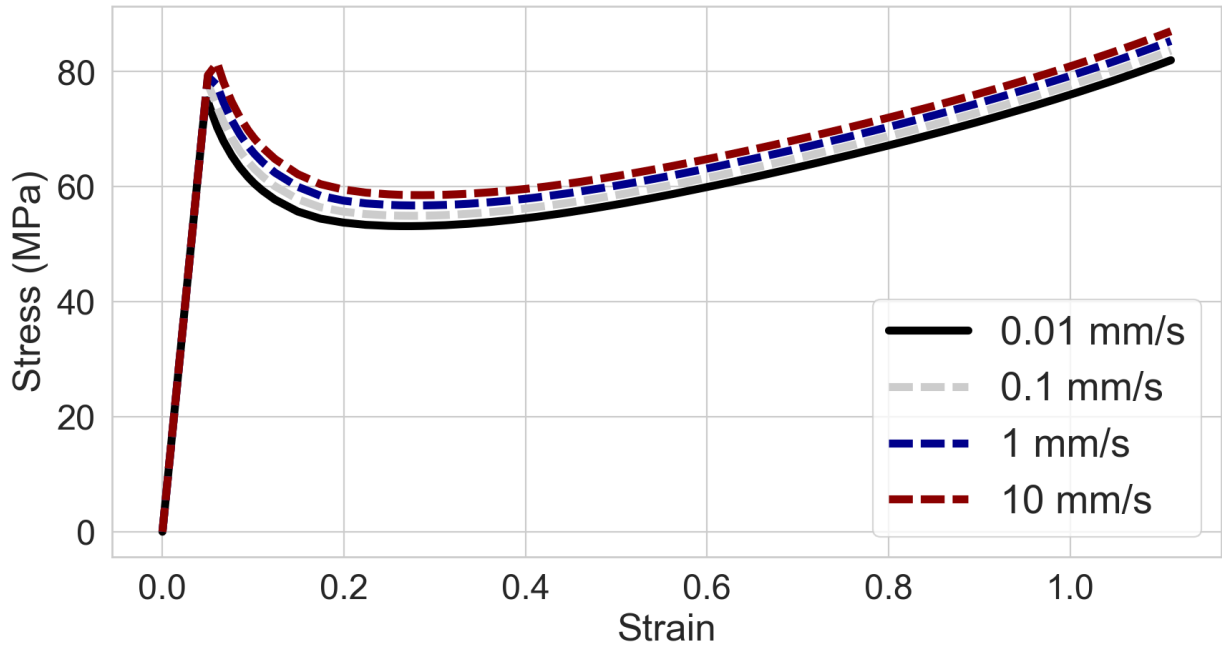
Figure 3.10: Impact of strain rate variation on the behavior of the stress-strain curve

It is undisputed that the deformation rate imposed on the deformable body is a ratio between the deformation due to the application of an external effort and the application time. In explicit dynamics analyzes, the time of application of the external effort interferes in the computational cost, that is, numerical evaluations with low strain rates can be quite computationally costly.

In view of the results obtained by the sensitivity analysis of Arruda-Boyce model, it is possible to observe that the increase or decrease in the region of linear elasticity due to the magnitude of the deformation rate can be compensated through other parameters such as the pre-exponential factor or more effectively by modifying the activation energy parameter. Such a strategy presents itself as a viable alternative for evaluations where the computational cost can be quite costly, as well as for simulations where the influence of the strain rate is not configured as the objective of the analysis.

Chapter 4

Artificial Neural Networks

In general, as previously presented in the chapter 1.2.4, Machine Learning refers to the study of problems in a statistical way, being able to generalize a function from limited observations through training models. The most basic representation obtained by using Machine Learning can be performed for one-dimensional curve-fitting, commonly used, for example, for linear regression problems with a single variable. When applied to larger problems, the tool will work on obtaining hypersurfaces that minimize the function.

The basic structure of neural networks is primarily composed of: (1) input and output data, (2) layers, (3) optimizer and (4) loss function. Figure 4.1 illustrates this basic anatomy of neural networks, where the input layer receives information from the input data, which is the data used for training the model. The input layer is then connected to the other layers that make up the neural network, which can be sequential or non-sequential. The following steps work as an iterative process, where predictions are made from an entity called weights. Each prediction made by the model is compared with true targets from a loss function. In this iterative process, weights are updated from an optimizer, so that predictions are as close as possible to true targets.
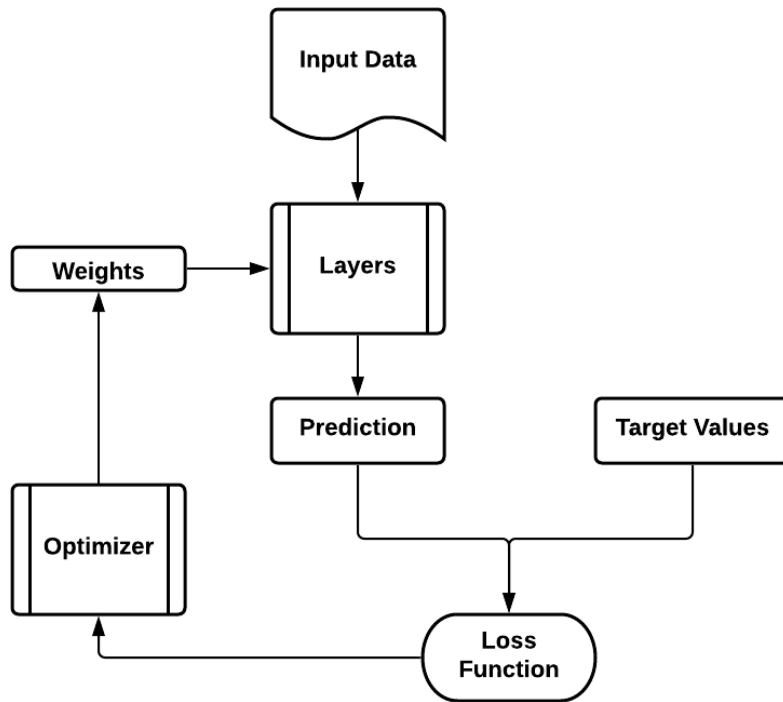
Figure 4.1: Basic structure of neural networks.

A first introduction about neural networks can be made from the understanding of what would be a perceptron, a concept developed between 1950 and 1960 by the scientist Frank Rosenblatt, inspired by Walter Pitts and Warren McCulloch. Such a model is based on a neural network composed of sigmoid neurons where neurons are capable to output values equal to 0 or 1. The simple example shown in figure 4.2 shows a perceptron with three inputs x_1, x_2 and x_3, in which Rosenblatt introduced a first understanding of weights, real numbers that manage to express the importance of the respective input to the output. Different from the outputs, it is possible to assign any value to the weights.
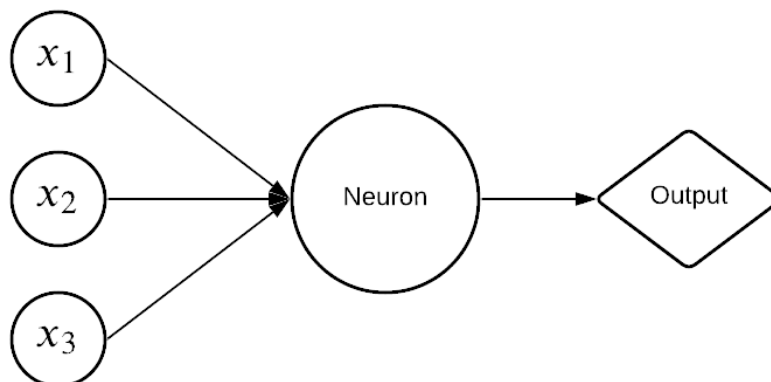

Figure 4.2: Structure of a perceptron.

The structure of layers in neural networks depends on the output format, where each type of layer is appropriate for a given type of input tensor. In the usual case of a dataset with different information per event, the use of a two-dimensional tensor can be used, called Dense class in the Keras library. The basic implementation of dense layers (default configuration) is based on a linear operation between the output and the input, it should be noted that when it comes to layers, an input dimension is automatically related to the output of the previous layer. Thus, the linear representation of a dense layer is given by:

$$x_o = \phi_a(x.W + b) \tag{4.1}$$

Where ϕ_a represents the activation function applied to the layer, W is the Kernel term, representing the weight matrix, x the input layer and b the term referring to the bias. For the initialization of the weight matrix and the bias, random Gaussian values are used. The figure 4.3 presents a neural network composed by 2 hidden layers, initially fed by a layer related to the input data. The figure shows the presence of the weight matrix (W), as well as the bias (b). It is possible to identify schematically, as shown in eq. 4.1, the process of composing the neurons of each layer in order to obtain the output of the neural network.
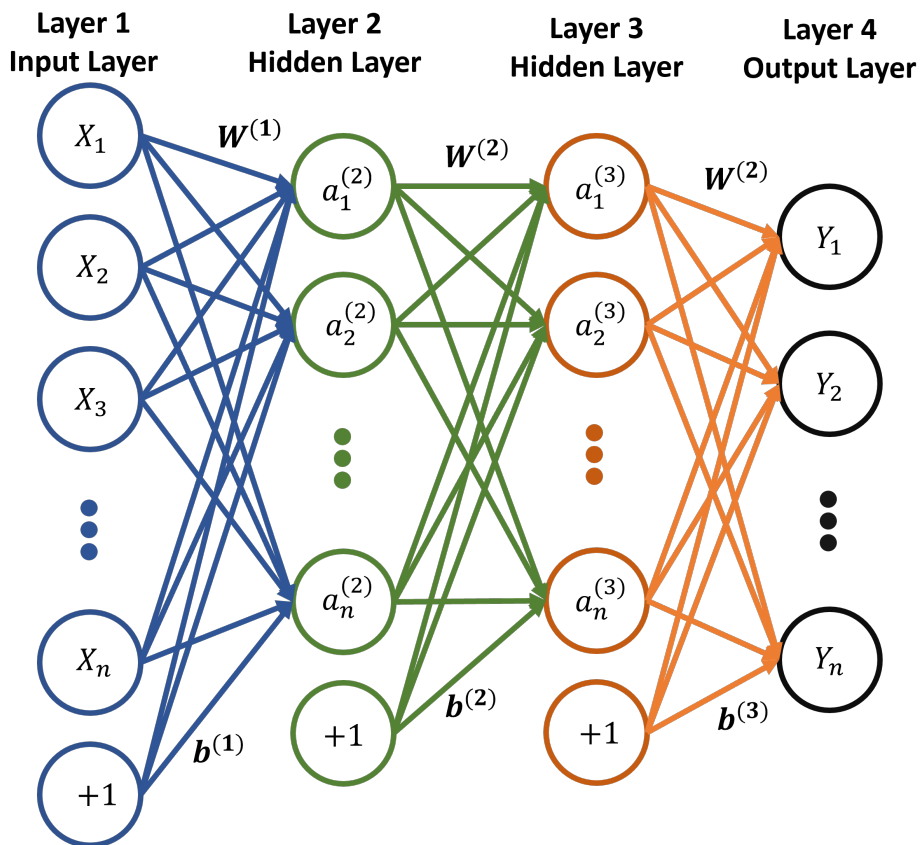

Figure 4.3: Representation of a neural network composed of two hidden layers.

As shown in eq. 4.1, the neural network will apply a linear representation between the output and the input, however, depending on the object of analysis, such representation

may not be sufficient, therefore, the implementation of customized layers may be necessary. The use of the API tool allows the creation of layers of greater complexity.

Regarding the activation functions present in the field of neural networks, its application occurs between the input feeding the current neuron and the output of this same neuron towards the next layer. Activation functions have a determining role in the output model of learning, accuracy, and computational efficiency of model training, i.e., they have a great effect on the model's capacity and convergence speed. In certain circumstances, the incorrect use of the activation function can hinder or even prevent the model from converging.

Among the most commonly used functions are: (1) binary function, which can be used for classification problems in 2 categories, (2) linear activation functions, (3) sigmoid/logistic functions, used for outputs between 0 and 1, normalized at the output of each neuron and commonly used for classification problems, (4) tangent hyperbolic function, (5) ReLU - Rectified Linear Unit, a function that returns $max(x, 0)$ allowing faster convergence of the neural network. Other functions are available, as well as the possibility to create customized functions.

In Machine Learning applications, the back-propagation algorithm is commonly used in conjunction with Gradient Descent, a base algorithm for several others, such as Adam. The purpose of applying the Gradient Descent is to minimize the loss function through an iterative process, starting with random values, called random initialization. Regarding Gradient Descent, the term called as learning rate refers to the step size of each iteration. If it is too small, the algorithm will need many iterations to converge and otherwise, if it is too large, the minimum global value may not be found, leading to a divergence.
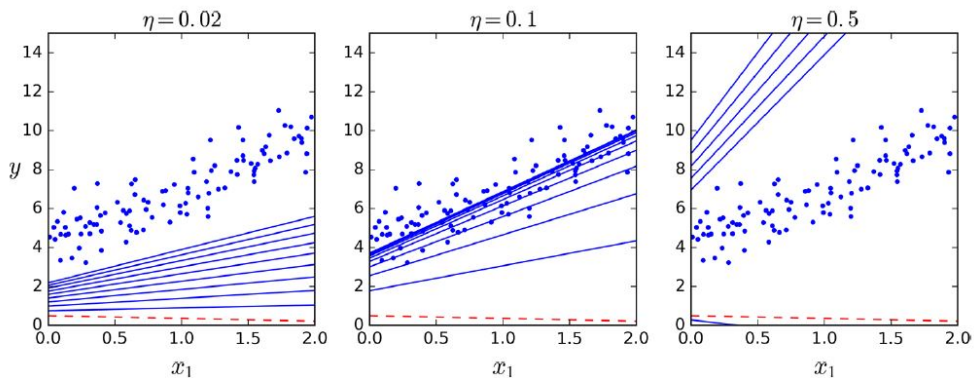

Figure 4.4: Example of various learning rates for Gradient Descent method. Geron [2017]

The figure 4.4 presents three different situations for the study of rate learning, in the first case the learning rate is less than ideal, that is, it appears that it will take more iterations than the ideal to obtain the convergence of analysis. The opposite situation occurs in the third graph of the figure, where the learning rate is so large that results in a divergence.

The second case of the figure presents an intermediate situation, where the imposed value of the learning rate was able to achieve a convergence, however, without needing so many iterations for this purpose. Still regarding the optimization process, one of the biggest difficulties is in identifying when the global minimum is reached and not just some local minimum, a fact that can be achieved with other strategies, such as the use of Callbacks in Keras.

Gradient Descent can be applied mainly in three different ways: (1) Batch Gradient Descent, (2) Stochastic Gradient Descent, and (3) Mini-batch Gradient Descent. In the first case, the Loss function gradient will be calculated for the entire model, which requires a high computational cost for that purpose, especially for models with a very large training set. In the second case, instead of evaluating the entire model, the algorithm will choose a random instance in the training set (epoch) for each step and thus calculate the gradients for that instance. Therefore, the computational cost for training the model will be much lower. Due to its stochastic nature, such a model presents less regularity, that is, instead of decreasing progressively until reaching the minimum, the Loss function will bounce up and down, however, decreasing its average until reaching the minimum. According to Geron [2017], when the Loss function is very irregular, the application of Stochastic Gradient Descent can help to skip local minimums, having a greater chance of finding the global minimum than Batch Gradient Descent. Regarding the Mini-batch Gradient Descent, this algorithm will work similarly to the Batch Gradient Descent, however, at each step, instead of computing the gradient of the entire training set, it will compute the gradient of small random sets of instances, called mini-batches.

Chapter 5

Methodology

This chapter describes the methodology used to: (1) predict the material parameters of the rheological model used for evaluating polymers under uniaxial compression, as well as the stress-strain curve, and (2) predict the stress-strain curve, displacement-force curve and contact pressure of indentation in metals.

The reader will also find information in this chapter about the experimental tests performed for the calibration of the numerical model in Finite Element, as well as the numerical model validations. The methodology used to predict the targets via ANN for each of the evaluated cases is then detailed.

5.1   Finite Element Modeling

In this section, the reader will find out about the numerical study of (1) visco-elastoplastic behavior of polymers under uniaxial compression test and (2) residual indentation in metals. For the study of polymers, the model adopted is based on: (1) Mulliken-Boyce model and (2) Gent model for the nonlinear hardening. Once the rheological model is defined, the mechanical behavior of cylindrical specimens will be evaluated in a uniaxial compression test, which will allow the calibration of the numerical model from the data related to the experimental tests conducted.

For the study of metals, the adopted model is based on the use of Hooke's law to describe the linear phase and Ludwik's equation to describe the non-linear phase. As with polymers, the studies carried out for metals will be validated by experimental tests of residual indentation sphere-plane tests.

5.1.1 Uniaxial Compression study in Polymers

To validate and establish the relevant parameters to the modified Mulliken-Boyce model, a series of evaluations of uniaxial compression tests for different compositions of polycarbonate (PC) and Acrylonitrile Butadiene Styrene (ABS) were conducted. The establishment of the parameters of the numerical model was based on the adequacy of the curve obtained via ABAQUS® in reference to the experimental tests of compression of the specimens.

The compression tests were conducted on a universal testing machine MTS 810 with a maximum capacity of 100 kN, where cylindrical test pieces of 9 mm in diameter and height were compressed to a total displacement of 6.1 mm at a strain rate of 0.01 mm/s with displacement and room temperature at 20°C control.

The compression was performed in a loading/unloading mode with 8 cycles, each with 5 steps of 0.1525 mm and with a variation in the compression speed in relation to time, in order to guarantee a constant strain rate. Discharges are considered in the test to reduce the friction effect between the lower and upper plate of the specimen support, as well as to mitigate the "jamming" effect of the cylinder under test. Finally, the output curves represent resulting average curves of 5 compression tests per evaluated material.

5.1.1.1 Numerical Model

During the first steps of the calibration process of Mulliken-Boyce's implemented numerical model for the description of the elastic-viscoplastic behavior of PC, ABS and blends of the two materials, challenges were identified in describing the behavior of the non-linear hardening response for strain levels greater than 60%. Thus, a modification of the original Mulliken-Boyce equation was carried out, changing the description of the non-linear hardening behavior from the 8-chain model by a model based on the equation presented by Horgan and Saccomandi [2002].

The constitutive model presented by Horgan and Saccomandi [2002] presents itself as an extension of the Neo-Hookean hyperelastic model, aiming at a better characterization of the response of elastomer-like materials at large deformations. Therefore, the Cauchy stress for the description of the nonlinear hardening phase can be determined according to the following equation:

$$\boldsymbol{T}_G = \frac{M_i}{J} \frac{1}{1 - \frac{I_1^* - 3}{J_m}} dev[\boldsymbol{B}^*] + k(J-1)\boldsymbol{I} \tag{5.1}$$

where, M_i represents an equivalent shear modulus, J_m is a dimensionless parameter that controls the limited chain extensibility at large strains, k is the bulk modulus, I_1^* is the first invariant of $\boldsymbol{B}^*$.

Based on the equation 3.39, it is therefore proposed to replace the term $\boldsymbol{T_B}$ for the term $\boldsymbol{T_G}$ in the equation 5.1, i.e., the description of the stress in the solid is:

$$\boldsymbol{T} = \boldsymbol{T_G} + \boldsymbol{T_{A,\alpha}} + \boldsymbol{T_{A,\beta}} \tag{5.2}$$

Such rheological model will be called modified Mulliken-Boyce model and will be used to describe the elastic-viscoplastic behavior of all simulations in Finite Element for polymers conducted during this work. Figure 5.1 presents a comparison between the adopted rheological model and the original Mulliken-Boyce model and, as it is possible to identify, the modified model more faithfully represents the results obtained experimentally.
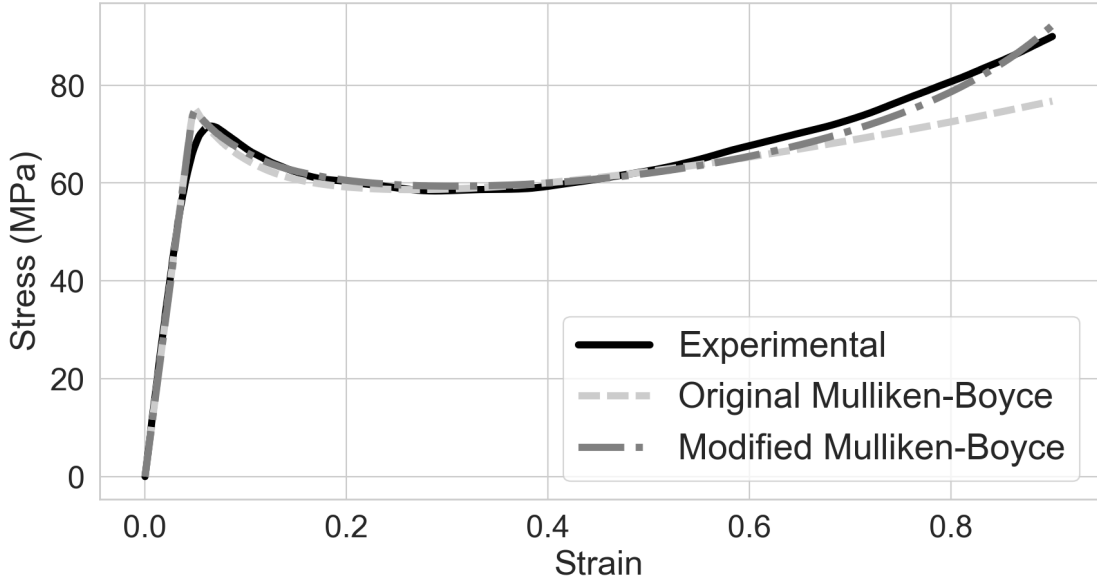
Figure 5.1: Uniaxial compression test - comparative between experimental test, original Mulliken-Boyce and modified Mulliken-Boyce: ABS.

The numerical reproduction of the uniaxial compression test via ABAQUS® was performed through the consideration of 1/4 of cylinder, being adopted for both symmetry boundary conditions on the appropriate faces, as shown in figure 5.2(a). In order to reproduce the contact between the upper and lower face of the specimen with the support and compression plate of the test machine, a surface-to-surface interaction between the faces in contact was adopted. For the properties of the contact formulation, the penalty method was adopted for normal and tangential behavior, allowing contact separation for the first mentioned behavior and definition of a friction coefficient of 0.1 for the second.

(a) Boundary conditions of the FE model.

(b) Hexagonal structured mesh of the numerical model for the study of uniaxial compression.
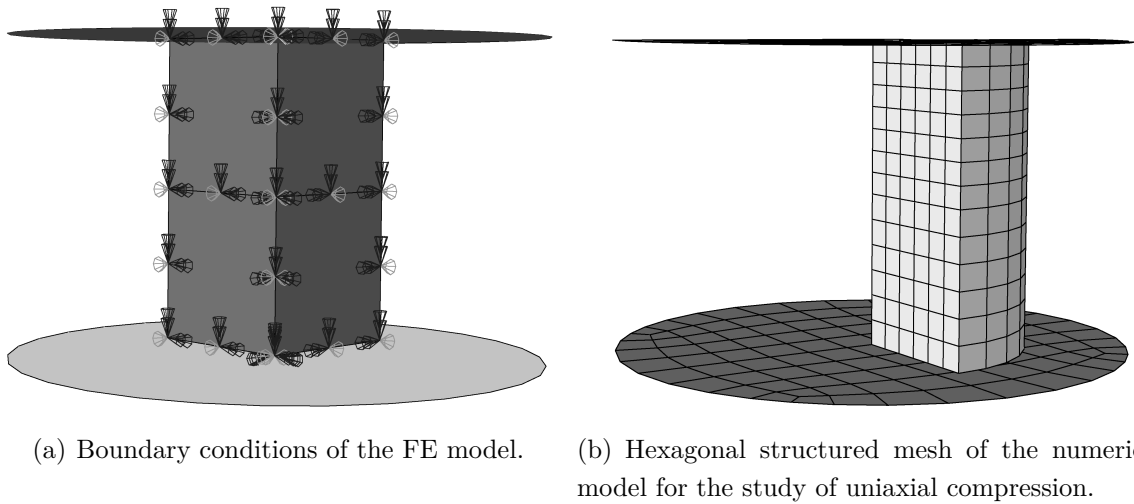
Figure 5.2: Finite element numerical model of the cylindrical specimen uniaxial compression test

Regarding the definition of contact, it is worth noting that the two support surfaces were represented as rigid bodies, in order to have a lower computational cost. The adoption of this numerical representation was based on the convergence of the simulation since it allowed the convergence of the numerical tests for deformations greater than 50%. The use of boundary conditions due to displacement and rotation restrictions were previously used, however, they did not prove to be a viable alternative for the series of simulations conducted, since they presented great distortions in the elements present in the restricted surfaces, thus causing failure of convergence.

The analysis of uniaxial compression of the cylindrical specimen was implemented from a structured mesh consisting solely of explicit hexagonal elements with an average dimension of $7 \times 10^{-4}\,m$, length obtained after conducting a mesh convergence study. Due to the presence of large deformations in the analyzes conducted, the use of mesh distortion and full integration controls was defined. The mesh adopted in the numerical model is shown in figure 5.2(b).

Two other important aspects for the implementation of the adopted model are the use of a non-linear increment of displacement, in order to impose on the simulation a constant deformation rate and the use of the mass scaling tool for simulations in a quasi-static regime, that is, when dynamic effects are not significant in the behavior of the analyzed object. Such a tool works to control the time increment, especially in small elements that end up controlling the time increment of the simulation.

5.1.1.2 Numerical Model Validation

The behavior of the cylindrical specimen under the effect of uniaxial compression is represented in the figure 5.3 in four different compression stages. The numerical model was adopted to predict the behavior of the specimen up to axial strain rates of 60%, although it was able to predict at strain levels of 110%. In the latter case, the model presented a greater inadequacy, especially for ABS and PC.
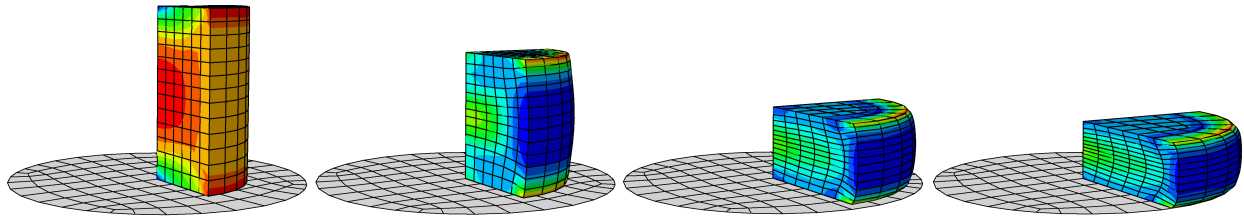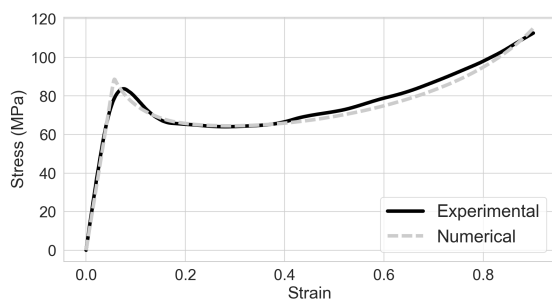

Figure 5.3: Different stages of simulation of the numerical uniaxial compression test.

The comparative graphs between the experimental and numerical results are presented in the sequence of figures below. Figure 5.4(*a*) represents the data for the PC, fig. 5.4(*b*) for ABS, 5.5(*a*) for PC/ABS 80:20 and fig. 5.5(*b*) for PC/ABS 60:40.
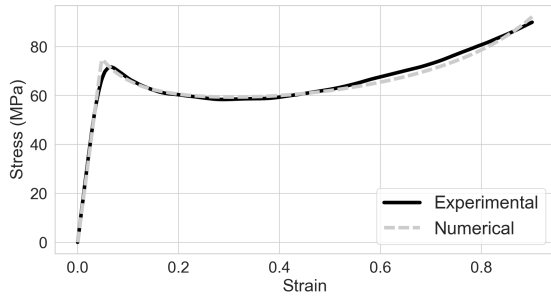

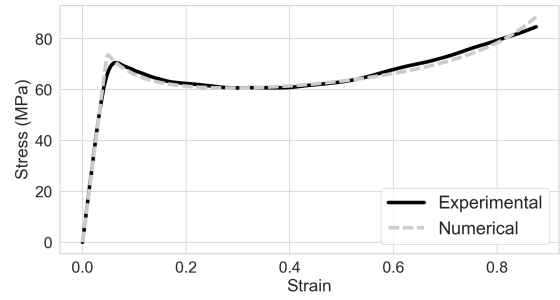(a) Uniaxial compression test - experimental-numerical: PC.
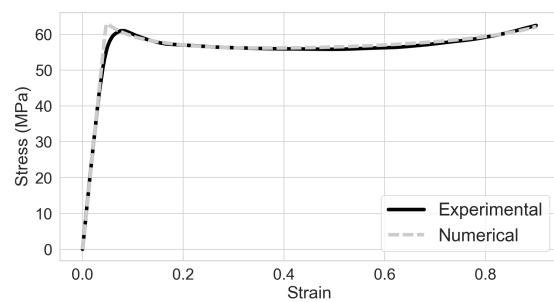
(b) Uniaxial compression test - experimental-numerical: ABS.

Figure 5.4: Uniaxial compression test - experimental-numerical calibration

(a) Uniaxial compression test - experimental-numerical: PC/ABS 80:20.

(b) Uniaxial compression test - experimental-numerical: PC/ABS 60:40.

Figure 5.5: Uniaxial compression test - experimental-numerical calibration

Table 5.4(a) shows the coefficients of determination for all the comparative curves performed during this section.

Table 5.1: Coefficients of determination between experimental and numerical results.

Material	R^2
PC	0.96
PC/ABS 80:20	0.98
PC/ABS 60:40	0.99
ABS	0.99

In view of the obtained values, good correlations between the experimental and numerical results for all investigated cases is identified. PC showed the lowest value of coefficient of determination, equal to approximately 0.96, whereas the PC/ABS 60:40 blend and ABS showed the best fit with 0.99. In general, the coefficient of determination for all materials evaluated, under the magnitude of imposed strain, are similar.

When evaluating the curves obtained for all numerical tests conducted, it is identified that the region to present the greatest dissimilarity in relation to the results obtained through the experiment is related to the yield zone. The experimental results show a smoother region, while the numerical model shows a more abrupt yield.

In view of the numerical results presented for the evaluation of the target polymers of this study, it is possible to identify that the FE model adopted can reproduce the viscoelasto-plastic behavior of these materials in a satisfactory manner. This preliminary result contributes to the state of the art, given the small presence of studies that present methodologies for numerical implementation aimed at evaluating the visco-elasto-plastic behavior in polymers and in particular for implementations via VUMAT and for the study of indentation.

5.1.2   Residual Indentation study in Metals

Indentation tests were performed between two components: (1) prismatic flat counterparts composed of various metals in the following dimensions: 20mm x 20mm x 5mm and, (2) spherical pad made of Tungsten carbide with 2.5 and 7.5 mm radius. The counterpart and pads are shown in figure 5.6(a).

Regarding the preparation of the samples, all were cleaned with isopropyl alcohol and stored in zip lock bags, to reduce the possibility of oxidation. Before the experiments, all the pieces were carefully examined in order to check the presence of any imperfections and contaminants. After the conclusion of the tests, the parts were cleaned using a compressed air gun to remove possible particles and put in new zip locks to be subsequently evaluated under the microscope.

For the experiments carried out, an MTS 809 axial-torsional testing machine was used, a machine capable to perform axial and rotational motions simultaneously. Therefore, the experiments were carried out from the insertion of the counterpart together with a custom holding device in order to accommodate it firmly, as well as the spherical pad, as shown in figure 5.6(b). Regarding the equipment to evaluate the deformed surface, a confocal laser microscope (Olympus LEXT OS4100) and an optical microscope (Carl Zeiss AXIO Imager M2) were used.

After the correct positioning of the counterpart and pad in the test equipment, the Basic Testware software provided by the manufacturer was used to define the test parameters related to the application of the compression load. For this purpose, the desired load is then configured in the software and, after manually displacing the upper grip towards the lower one, the software slowly rises the flat pad in the direction of the tool at a fixed speed of 0.5 mm/min. After reaching the desired load, the pad stops moving and remains fixed with a constant contact pressure at the pre-set value, providing as output a history of displacement and force during the entire test. After the compression test was performed, the flat samples were then analyzed in the microscopes with a 20x magnifications lens using an increase in luminosity of approximately 60%. From these analyzes, residual penetration and volume of the indentation mark were obtained.

(a) Polymerical flat counterpart and R3 steel pad.
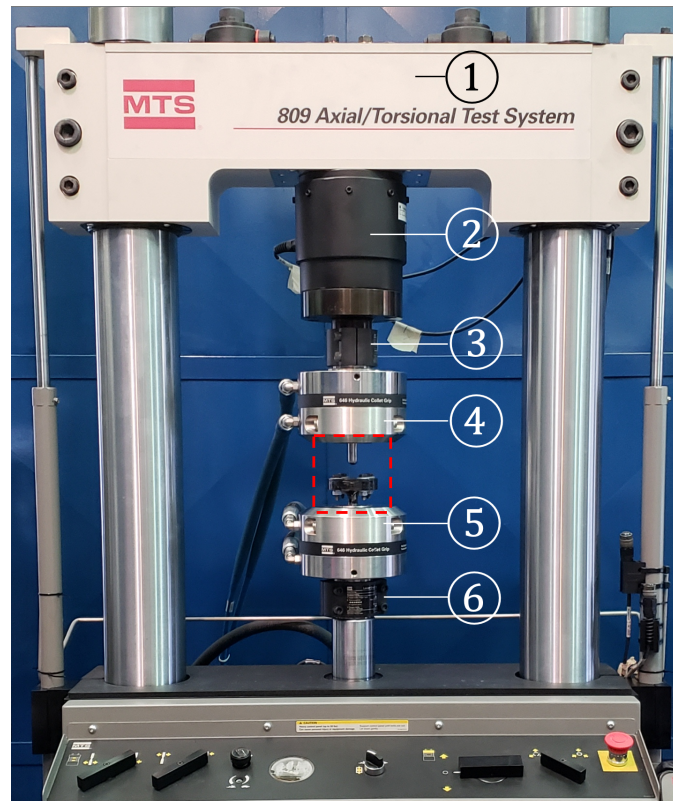
(b) MTS 809 axial-torsional testing machine: (1) Crosshead, (2) Force transducer, (3) Top cell, (4) Upper grip, (5) Lower grip and (6) Bottom cell.

Figure 5.6: Polymerical flat counterpart and R3 steel pad.Padim et al. [2019]

5.1.2.1 Numerical Model

As constitutive model, a J2-associated flow theory with rate-independent deformation and isotropic hardening is adopted. The flow is described according to the von Mises criterion and the stress-strain relationship is defined by the Ludwik's equation,

$$\sigma = \sigma_0 + K(\epsilon + \epsilon_0)^n, \tag{5.3}$$

where, σ is the true stress, σ_0 the yield stress, ϵ_0 the yield strain, ϵ the plastic strain, n the hardening exponent, and K a strength coefficient.

To simulate the behavior of a solid subjected to a spherical indenter, a FE model is implemented in the commercial package ABAQUS®. Since the indentation problem is axisymmetric, its modeling can be achieved in a two-dimensional domain and using only one-half of its geometry.

Concerning the discretization of the solids, the pad and flat counterpart domains are divided using structured meshes composed of first order quadrilateral elements. In order

to achieve accurate results at a reduced computational cost, full Gaussian integration is used only on the elements at the contact interface while the remaining ones are defined with a single Gauss point (reduced integration). Moreover, the contact interface is meshed with 15×10^{-6}m elements while the other zones employ elements up to 2mm in size. The implementation of the contact constraints is achieved using a node-to-segment segmentation of the interface and the Lagrange multiplier method for the enforcement of both normal and tangential constraints. The problem is defined in a static setting and the prescribed load is applied to the top of the sphere in 100 incremental steps while the base of the flat counterpart is restrained in the y-direction. The solution procedure adopted is the Newton's method with a convergence criteria set as a residual force of 10^{-8}N. Fig. 5.7 shows the geometry, its partitions, and the discretization employed.
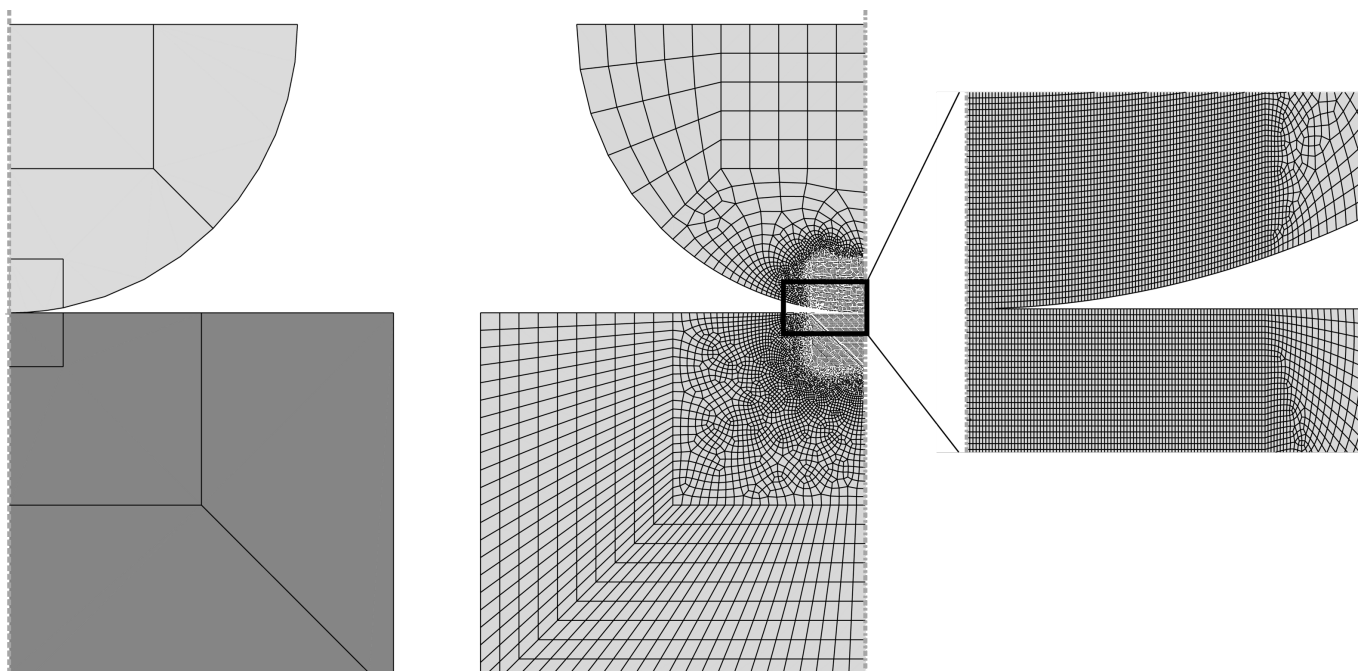

Figure 5.7: Finite element numerical model of the flat counterpart and pad.

5.1.2.2 Numerical Model Validation

In order to validate the proposed FE model, two steps are considered: an evaluation in the linear elastic domain; and another in the inelastic domain. For the validation of the model in the linear elastic domain, the set of analytical equations for sphere-to-flat contact known as Hertzian formulae Hertz [1882] and Johnson [1985] has been considered. Since modeling of elastic behavior is rather trivial, just one material pairing is analyzed: a flat SAE 1045 steel specimen ($E = 210$GPa, and $\nu = 0.33$) and a Tungsten carbide spherical indenter ($E = 669$GPa, $\sigma_0 = 650$MPa, and $\nu = 0.22$). The force, F, applied to the indenter is set to 100N and the indenter radius, r, is 7.5mm. Table 5.2 presents the comparative data between the numerical and analytical results, showing a maximum relative error equal

to 3.44%.

Table 5.2: Validation: analytical versus numerical results in the elastic phase.

Parameter	Analytical	Numerical	Rel. error (%)
Indentation depth (mm)	0.0029	0.0030	3.44
Spherical cap's radius (mm)	0.1470	0.1490	1.34
Max Pressure (MPa)	2186.57	2153.00	1.53
Max shear stress (MPa)	466.64	463.40	0.69

For the validation of the FE model within the plastic zone, an evaluation of the residual indentation radius of four materials, under at different test configurations, is carried out. Tungsten carbide spheres (2.5mm and 7.5mm radius) are employed to promote the indentation marks on prismatic metallic specimens (20mm x 20mm x 5mm). The experiments are carried-out on a MTS 809 axial testing machine together with a custom holding device to accommodate the specimens. The compression load is applied using a prescribed displacement rate of 0.5mm/min. After indentation, marks are established and then the specimens are analyzed in a confocal laser microscope (Olympus LEXT OS4100). Further details on the experimental procedures can be found in Padim et al. [2019]. Table 5.3 presents the comparison between experimental and numerical data, where the maximum error observed is equal to 5.49%.

Table 5.3: Validation: experimental data versus numerical results in the inelastic phase.

Counterpart material	F(N)	r(mm)	Exp.	Num.	Rel. error (%)
R3 steel	500	7.5	2.56	2.67	4.29
R3 steel	1000	7.5	5.56	5.51	0.90
SAE 1045	2450	2.5	76.0	74.0	2.63
AL 7050 T7451	2450	2.5	95.8	96.2	0.42
Brass C45801	2450	2.5	114.8	121.1	5.49

5.2 Applied Methodology

In order to fulfill the goal of creating an ANN able to make predictions, the methodology was firstly based on the conception of a numerical model for the simulation of uniaxial compression in polymers and sphere-to-flat contact interaction for the study of indentation in metals. In this way, a FE model was implemented within the commercial package ABAQUS®. Nevertheless, other numerical approaches such as in-house codes and different methods like the Boundary Element Method can be employed for this task. The only restriction is the calibration and thorough validation of the numerical model adopted. For

the description of the mechanical behavior of the evaluated polymers, the modified Mulliken-Boyce method is applied. For the studies of indentation in metals, Hooke's law and Hertzian formulae are employed for the linear elastic zone, while for the nonlinear zone the Ludwik's equation was defined. Once identified that the adopted models satisfactorily reproduce the experimental tests, the numerical model in FE can be employed as a surrogate model for the generation of the large dataset used to train the ANN model.

The methodology adopted for the mechanical behavior characterization of the evaluated materials was based on the following structure: creation of an input dataset generated via simulations in Finite Element and training an ANN model to predict the behavior from the simulation's inputs and outputs conducted via FE via ABAQUS®. Due to the numerical model adopted having as a basic premise the representation of the mechanical behavior of the materials, the numerical models adopted were previously calibrated from experimental tests. Such a strategy allows the generation of a larger dataset for the composition of the ANN model, if compared to the adoption of a training model from a dataset of experimentally data. Such a methodology was designed to perform all predictions studies by the ANN algorithms developed in this work, and the same methodology is applied to all four studies:

1. Prediction of the material parameters of the modified Mulliken-Boyce model;

2. Prediction of the stress-strain curve using the modified Mulliken-Boyce numerical model;

3. Prediction of the stress-strain curve through the displacement-force curve obtained via indentation test;

4. Prediction of the displacement-force curve and contact pressure through the stress-strain curve obtained via the indentation test;

For all studies performed, a supervised deep learning algorithm was implemented in Python programming language, using mostly the Keras library.

5.2.1   Uniaxial Compression in Rigid Thermoplastic Polymers

Figure 5.8 shows the adopted methodology applied for the prediction of the material parameters and stress-strain curve of the modified Mulliken-Boyce model, respectively. The main differences compared to the study in metals are in the definitions of input, output, boundary conditions, and Artificial network layout. In general, the methodological structure will consist of a database generated from a finite element numerical model that reproduces the experimental tests and, later, will be used as input and/or output dataset for the implementation of the ANN model.
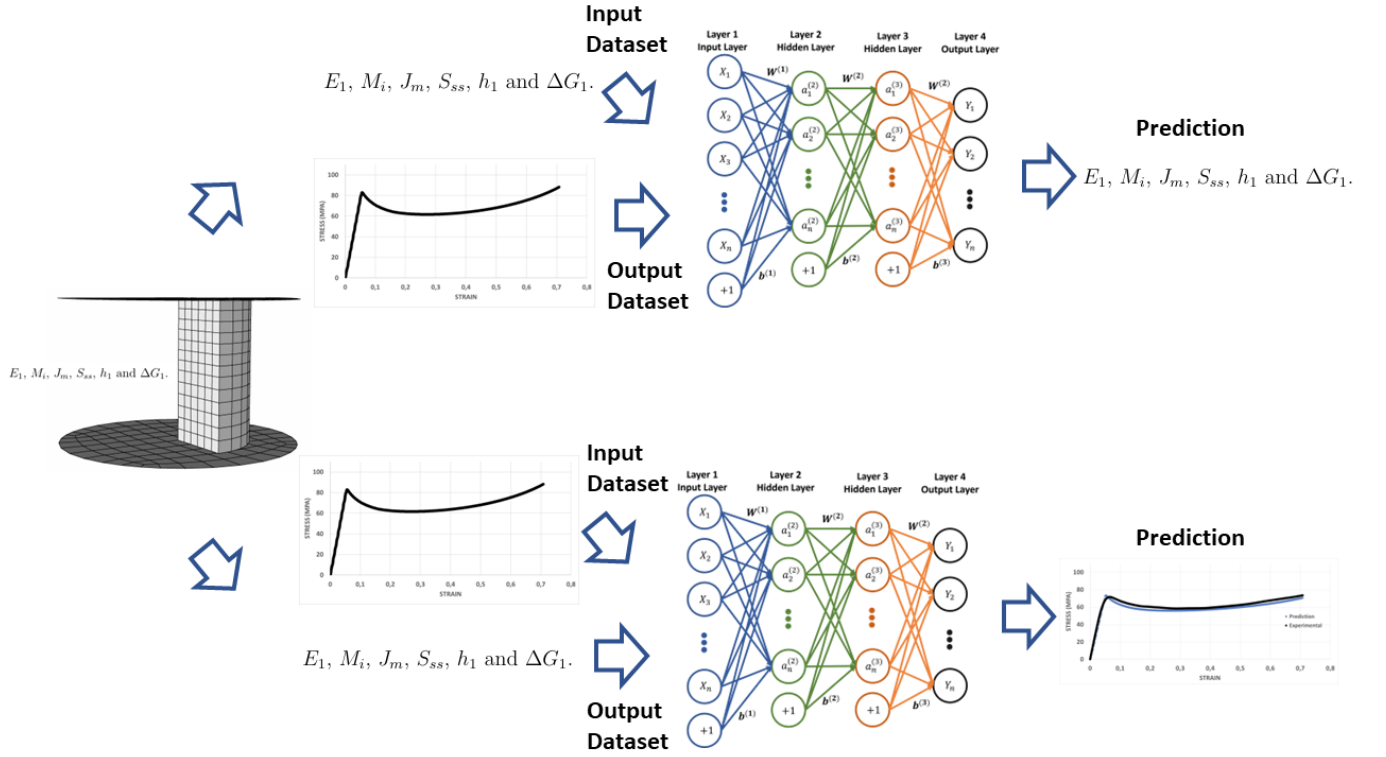
Figure 5.8: Methodology flow for predicting the material parameters based on the stress-strain curve applied for the study in rigid thermoplastic polymers.

The relevant parameters are inputted in the modified Mulliken-Boyce algorithm (implemented via VUMAT) so that Finite Element simulations can be performed. During the FE simulations, the model's output is defined, which for the studies carried out are based on the stress-strain curve. Subsequently, the dataset generated from the material parameters and the stress-strain curves obtained via FE is used as input and output for the ANN Model. For the case of the study of indentation in metals, in addition to considering the material parameters and the stress-strain curve, the displacement-force curve is also considered to compose the input and/or output, depending on the study carried out, for instance.

The parameters related to the input dataset of the ML model were chosen from the sensitivity analyzes performed in the section 3.3.4. For the construction of the input dataset, variations in these parameters were carried out and implemented numerically via Finite Element through the procedures performed in the section 5.1.1, totaling 520 simulations to compose the input dataset. The parameters adopted to compose the target of the ML model are: E_1, M_i, J_m, S_{ss}, h_1 and ΔG_1. Tab. 5.4 shows the range of values considered for each parameter.

Table 5.4: Range of material properties adopted for generating the database in the study of rigid thermoplastic polymers.

Parameter	Lower Limit	Upper Limit
E_1 (MPa)	765	1607
M_i	3.04	19.76
J_m	1.75	4.73
S_{ss} (MPa)	0.27	0.90
h_1 (MPa)	125	475
ΔG_1 (J)	1.86×10^{-19}	5.67×10^{-19}

Certain magnitudes of the evaluated material parameters resulted in the divergence of the simulation via FEM. Because of this, in order not to consider incomplete simulations in the training of the neural network, a data cleaning was performed to exclude simulations not completed via FEM. Such cases happened for the parameters relevant to the occurrence of yield and nonlinear hardening.

Regarding the handling of data, the strategy was based on the normalization of both the input and the output of the ML model, due to the large differences in magnitude between the data. This strategy is widely used in ANN, since it facilitates the convergence of the model, as presented by Chollet [2018].

In parallel to the strategy adopted regarding the data interpolation process in order to decrease the size of the input tensor, the elastic zone of the strain-strain curve with less data points were intentionally represented, as it is represented by a linear zone. After such a region, there is the presence of a greater number of points due to the non-linearity of the curve, favoring the learning process. The highest data density is present in the representation of the stress-strain curve of the materials investigated in this study, however, behaviors that exceed the limits established by the behavior of the PC and of ABS were considered in order to investigate, further on, the possibility of such a proposed and adopted model being able to describe the behavior of other polymers with similar behavior to the polymers considered in this work.

5.2.1.1 Artificial Deep Neural Network Applied to the prediction of Mulliken-Boyce Parameters from Stress-Strain curve

For the description of the stress-strain curve, 150 points were considered, which resulted in a tensor with dimensions equal to 520x150. As the output dataset is composed of the material parameters of the modified Mulliken-Boyce model, the dimension of the 2d tensor is equal to 520X1 or 520x6. It should be noted that the points on the stress-strain curve considered in the training of the neural network were obtained via interpolation, since the

use of 150 ordered pairs is sufficient for the ANN. The stress-strain curve generated via FEM has 1000 ordered pairs.

Regarding the data splitting (splitting of the complete dataset into two different datasets, training, and testing dataset), it was defined the use of 70% of the total curves for the training dataset and 30% for the testing dataset.

Concerning the composition of the model's neural networks, the strategy adopted was the use of sequential layers implemented via API, where each target's prediction was obtained via a different branch of the neural network. All predictions were made using linear neurons, except the predictions for the M_i. For this parameter, it was adopted the use of quadratic neurons implemented via custom layers also via API.

One of the biggest challenges for the implementation of neural networks is defining the layer structure, something that requires a lot of time and processing memory due to the need to run the model for each change in order to assess the impact on the predictions. The structure of neural networks for predicting the parameters of the modified Mulliken-Boyce model is shown in figure 5.9. As it is possible to identify in this figure, the adopted neural network is represented as a deep learning, due to the number of hidden layers of the model. The neural network for the prediction of material parameters is composed of two types of branches. The branch presented in orange considers the complete dataset, that is, all material parameters make up the dataset. The branches shown in blue take into account only the dataset for parameter to be predicted. In this way, as shown by figure 5.9, for the prediction of ΔG_1, all parameters are considered. For the remaining, the other parameters are not. For the prediction of ΔG_1, E_1 and h_1 only two hidden layers are used, all composed of linear neurons. For the prediction of the parameters S_{ss}, J_m and M_i, three hidden layers are used, and all composed of linear neurons, except the M_i network, which uses quadratic elements. Several other layer configurations were tested during the studies carried out (simpler architectures, with fewer layers and neurons, as well as more complex architectures), the configuration adopted is the one that presents the best accuracy of the predictions made.
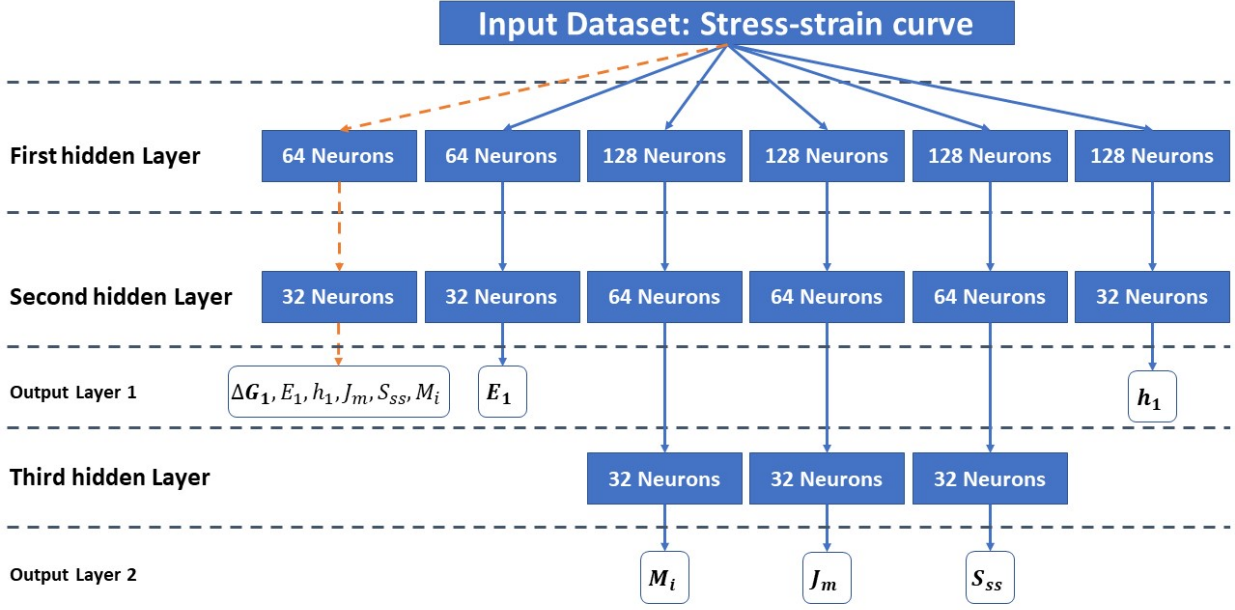
Figure 5.9: Adopted Neural Network for the prediction of the modified Mulliken-Boyce parameters through stress-strain curves.

The algorithm adopted for the optimization process was Adam, presented by Kingma and Ba [2014] and applied for first-order gradient-based optimization of stochastic objective functions through an adaptive estimate of lower-order moments. In general, the Adam optimizer can be seen as a combination of two other algorithms: RMSprop and Stochastic Gradient Descent, working with the squared gradients to scale the learning rate. The adoption of Adams as an optimizer was made since it allows a faster convergence for studies of deep neural networks, compared to other optimizers. A comparison between several optimizers in the learning process in image processing using deep learning was presented by Kingma and Ba [2014].

Optimizers work along with loss functions for the learning process, for the ML model proposed, the mean squared error (MSE) was adopted, according to 5.4, where n represents the number of predictions generated, Y the target and $\hat{Y}$ the prediction.

$$MSE = \frac{1}{n} \sum_{n=1}^{n} (Y_i - \hat{Y}_i)^2 \qquad (5.4)$$

Working in parallel to avoid the occurrence of (1) overfitting and underfitting, habitual problems in the machine training process, and (2) failure of adequacy of the learning rate, callback functions were implemented via API in the adopted model. For the first situation, a tool called *Early Stopping* was implemented, where the learning process is completed when the algorithm identifies that the Loss function does not improve for more than 50

epochs. In this case, the learning process is interrupted and the weight matrix adopted refers to the $(n - 50)$ epoch, where n represents the last epoch of the training.

In the second situation, an algorithm was implemented via API to update the hyperparameter related to the learning rate in the Adam optimizer. Therefore, a decrease of 5% in the learning rate was defined for each situation in which the loss function does not show improvement for more than 15 sequential epochs. The adoption of this strategy, in addition to allowing better control of the training, allows a lower computational cost, since it starts training the model with greater magnitudes of learning rate that decrease as the model learns.

Finally, for the training step, a batch size equal to 32 was defined, which configures a case of Mini-batch Gradient Descent. During the construction of the ML model, the three following considerations were investigated: (1) Batch Gradient Descent, (2) Stochastic Gradient Descent, and (3) Mini-batch Gradient Descent. The use of (3) enabled the best accuracy of the model. The use of a batch size equal to the dimension of the input dataset entailed a higher computational cost and, in this study, did not provide improvements.

Table 5.5 summarize the structure and main information of the neural networks considered, i.e., neural network for predicting the material properties of the modified Mulliken-Boyce model.

Table 5.5: Number of neurons and activation function adopted for the ANN used to predict the material parameters of the modified Mulliken-Boyce model.

	ΔG_1	E_1	M_i	J_m	S_{ss}	h_1
1st hidden layer	64 - relu	64 relu	128 - relu	128 - relu	128 - relu	128 - relu
2nd hidden layer	32 - relu	32 - relu	64 - relu	64 - relu	64 - relu	32 - relu
3rd hidden layer	-	-	32 - relu	32 - relu	32 - relu	-
Neuron Order	Linear	Linear	Quadratic	Linear	Linear	Linear
Learning rate	10^{-6}	10^{-6}	10^{-6}	10^{-6}	10^{-6}	10^{-6}
Output Dimension	6	1	1	1	1	1

5.2.1.2 Artificial Deep Neural Network Applied to the prediction of the Stress-Strain curve from Mulliken-Boyce Parameters

A reverse model to the one presented in item 5.2.1.1 was also implemented. In this, instead of predicting the material parameters of the modified Mulliken-Boyce model, the reverse is performed, i.e., prediction of the stress-strain curve from the material parameters. In this case, the ANN model behaves like a surrogate model, instead of FEM. It uses neural networks instead of well-established methods, such as FEM, to obtain the mechanical behavior of materials.

To predict the stress-strain curve, it was defined that the output, i. e., the stress-strain curve, will be composed of 500 ordered pairs. When considering a smaller number of points, a lower accuracy of the model was obtained. A number of points greater than 500 did not lead to an improvement in the predictions made, it only increased the processing time. In this way, the input dataset has a dimension equal to 520x6 and the output a dimension equal to 520x500. The input and output dataset can still be represented by the data shown in figure 5.9 however, in the opposite way.

Regarding the other parameters considered in this configuration, the Adams optimizer continues to be used, however with an initial learning rate equal to 10^{-6}. Regarding the batch size, the case of Batch Gradient Descent was considered. Mean squared error (MSE) continues to be used as a Loss Function.
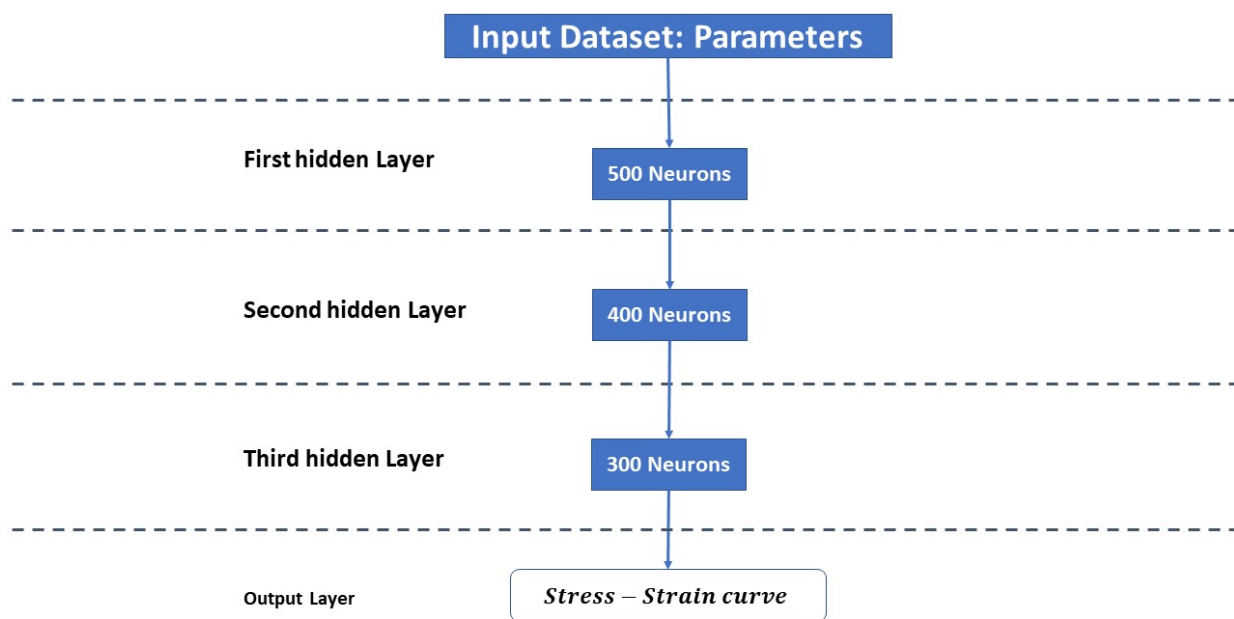
Figure 5.10: Adopted neural network for the prediction of the stress-strain curve through the modified Mulliken-Boyce parameters.

Fig. 5.10 presents the structure of the neural network considered in the stress-strain curve prediction study. As seen, there is the consideration of a deep learning with 3 hidden layers. The neurons used for all layers are linear and all make use of the Relu activation function. For training the model, 70% of the dataset was considered as training dataset. Of the remaining 30%, 50% was used during training as a test dataset and the other 50% used to evaluate the model's efficiency.

Table 5.6 summarize the structure and main information of the neural networks considered, i.e., neural network for predicting the stress-strain curve from the material properties.

Table 5.6: Number of neurons and activation function adopted for the ANN used to predict the stress-strain curve.

	Stress-Strain curve
1st hidden layer	500 - relu
2nd hidden layer	400 - relu
3rd hidden layer	300 - relu
Neuron Order	Linear
Learning rate	10^{-6}

5.2.2   Residual Indentation in Metals

Figure 5.11 presents the methodology adopted for the study of metals, i.e, stress-strain curve prediction from displacement-force curve and displacement-force curve prediction from stress-strain curve (material properties). As identified by figure 5.11, the study is carried out considering different boundary conditions and material properties: (1) indentation radius, (2) strength, (3) Young's modulus, (4) yield strength, (5) hardening strength and (6) hardening exponent. Table 5.7 presents the total interval considered for the generation of the database used in the training of the neural network. It should be noted that for the two studies carried out for metals, different considerations were made, resulting in different considerations of range of the parameters considered in the study. The considered range for each of the studies is presented in more detail in items 5.2.2.1 and 5.2.2.2.
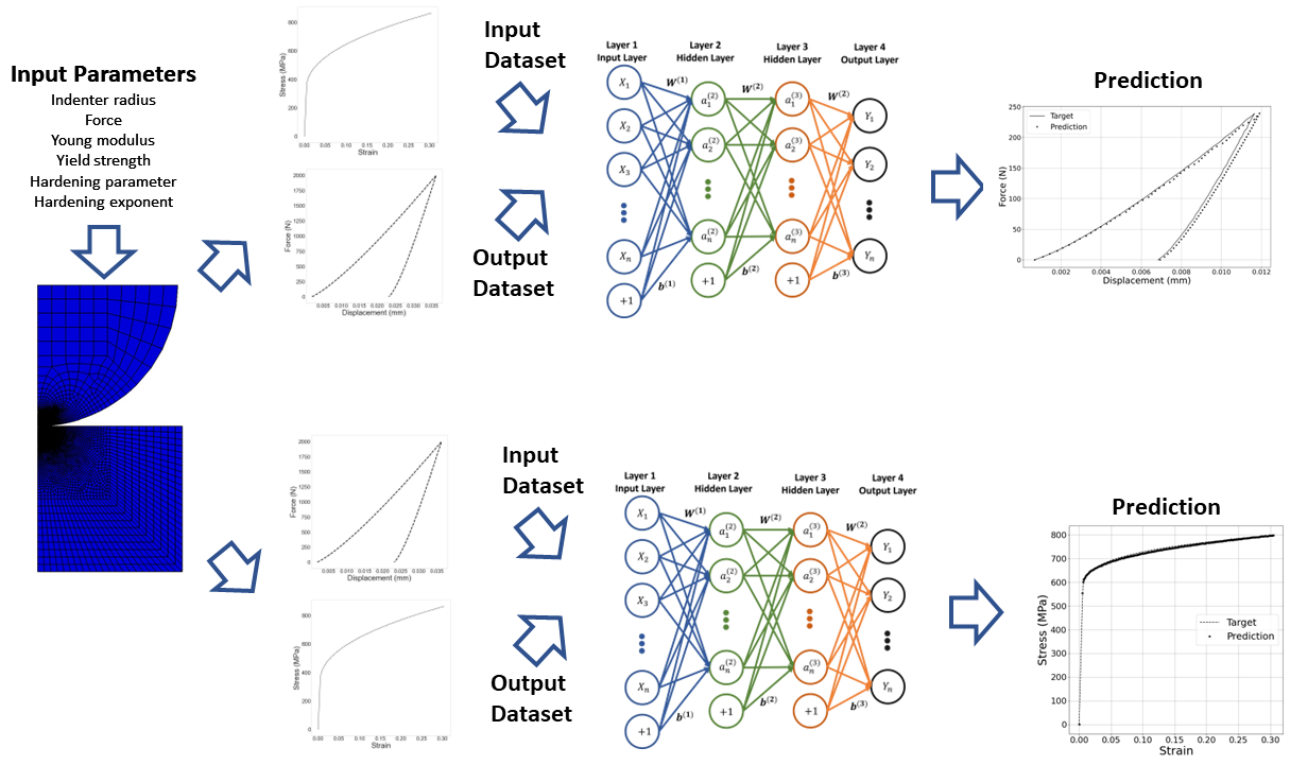
Figure 5.11: Methodology flow for predicting the stress-strain curve based on the displacement-force curve applied for the study in metals.

The database construction process starts from the generation of random values following a rectangular distribution for the parameters adopted within the stipulated range (something also applied for the study in rigid thermoplastic polymers). Subsequently, these values are used to obtain stress-strain and displacement-force curves via finite element simulations. Once the necessary databases have been created, in this case: (1) boundary conditions and material properties, (2) stress-strain curve and (3) displacement-force curve, neural networks are trained to carry out the desired predictions. As idealized for polymers, it is considered that the finite element model works as a surrogate model for the reproduction of experimental tests.

Table 5.7: Total range of the material properties adopted for generating the database in the study of metals.

	Range
indentation radius (mm)	2.5 - 15
Force (N)	100 - 3000
Young's modulus (MPa)	147 - 273
Yield strength (MPa)	200 - 800
Hardening strength (MPa)	150 - 1000
Hardening exponent	0.1 - 1.0

5.2.2.1   Artificial Deep Neural Network Applied to the prediction of the Stress-Strain curve from Displacement-Force Curve

In this study, the displacement-force curve was considered as input dataset and the stress-strain curve as output dataset, i.e., the main purpose is to predict the stress-strain curve from a displacement-force curve obtained through of an indentation test. The total sample space evaluated was 1000 curves and for such a database, 80% was considered for the training dataset and 20% for the testing dataset. The use of a larger (2500 curves) dataset did not result in better predictions.

After the establishment of the surrogate FE model, designed to be employed during the training phase, four different datasets have been produced. They have been selected to cover non-ferrous and ferrous materials, at elastic and inelastic loading conditions (the Poisson ratio of the flat counterparts is set to 0.30 for all simulations performed). A tungsten carbine spherical indenter is kept, and variations of material properties is only applied to the flat counterpart. The total range of the parameters that has been used for the training procedure are given in Table 5.8.

Table 5.8: Range of properties and parameters employed in each ML strategy for predicting the stress-strain curve.

Strategy	E(GPa)	σ_0(MPa)	K(MPa)	n	F(N)	r(mm)
Dataset A	147-273	200-800	150-1000	0.1-1.0	200-2000	2.25-15
Dataset B	147-273	200-800	150-1000	0.1-1.0	2000	2.25-15
Dataset C	147-273	200-800	150-1000	0.1-1.0	2000	7.5
Dataset D	147-273	200-800	150-300 300-450 450-600 600-850 850-1000	0.1-1.0	2000	7.5

It is important to emphasize that all datasets are composed of 1000 stress-strain curves, so that the comparison between the models can be performed. Each curve is obtained by combination of the mechanical properties indicated in Table 5.8. The dataset A covers the full spectrum of variations, meaning changes in material properties, compression force, and indenter radius. The dataset B covers variations in material properties and indenter radius at a constant compression force. In the dataset C and dataset D, only the material properties are varied. Furthermore, the dataset D has its range of strength coefficients segregated in five groups (1/5 of the original size) which makes it the dataset with narrowest spectrum. The reason for such considerations being implemented will be better clarified in item 6.1.1.

Four different artificial neural network models were implemented using the datasets

presented in tab. 5.8: ANN-A, ANN-B, ANN-C, and ANN-D. For all cases, the Adams optimizer (based on back-propagation algorithm and the Gradient Descent optimizer) has been used. Different mathematical models for the description of the neurons were evaluated. Linear neurons were selected as they have shown the best response. Regarding to the other basic parameters for the implementation of regression models, after several evaluations it was defined the use of: (1) Adams' optimizer with an initial learning rate equal to 0.01, (2) Mean Squared Error as Loss Function and (3) Early stopping, to avoid the occurrence of overfitting.

All models contain two layers (each one composed of 8 neurons) and in both layers a Softplus activation is used. Figure 5.12 presents the configuration of the layers used for the ANN model. It is noteworthy that this same layout is adopted in all studies aiming the prediction of the stress-strain curve from the displacement-force curve for indentation tests on metals.
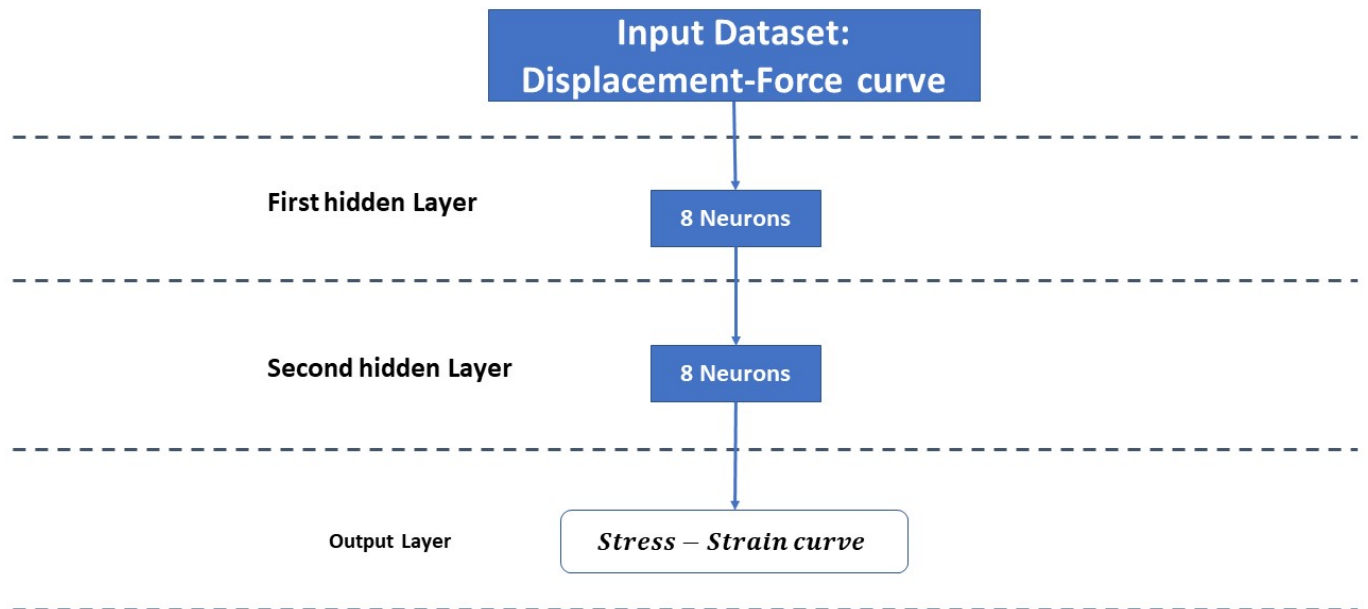
Figure 5.12: ANN layout for the prediction of the stress-strain curve through displacement-force curve for indentation tests.

5.2.2.2 Artificial Deep Neural Network Applied to the prediction of the Displacement-Force Curve and Contact Pressure from Material properties

The prediction of the displacement-force and contact pressure curve was obtained by a neural network with different layout and characteristics from those employed for the prediction of the stress-strain curve. The neural network is represented in 5.13, and as can

be seen, it has two hidden layers, each with 128 and 64 neurons. The Softmax activation function was adopted in both layers.
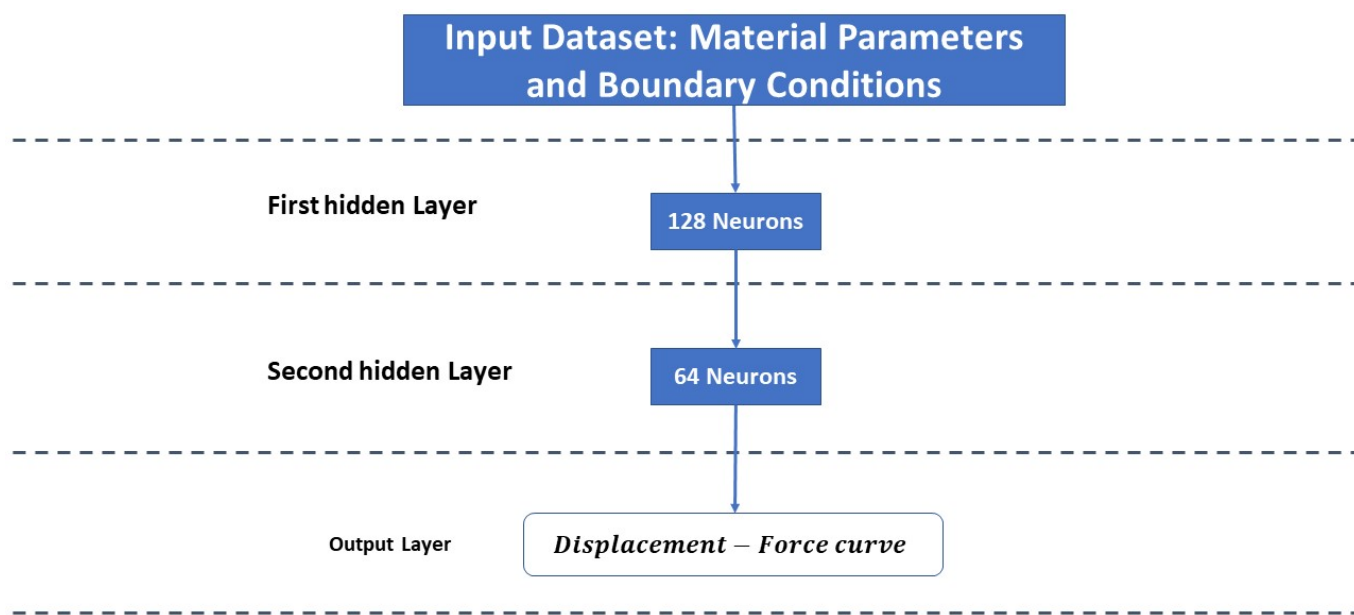
Figure 5.13: ANN layout for the prediction of the displacement-force curve through material properties for indentation tests.

The other parameters of the ANN model remained the same, i.e., use of Adams as an optimizer, initial learning rate equal to 0.01, Mean Square Error as Loss Function and Early stopping to avoid the occurrence of overfitting.

Given the use of other considerations in its construction, the dataset used for this study is different from the one used to predict the stress-strain curve. This other consideration was taken into account because a significant improvement in the predictions of the displacement-force curve was identified. The same observation was not seen in the studies conducted to predict the stress-strain curve, and as a result, their dataset is smaller. 3900 curves made up the dataset used to predict the displacement-force curve, of which 15% served as the testing dataset and 85% as the training dataset. Four alternative indentation radii were considered when building the dataset: 2.5mm, 5.0mm, 10.0mm, and 15.0mm. The compression force applied to the indenter was determined for each simulation from a random process according to a rectangular distribution, with lower and upper limits following table 5.9. The adoption of different ranges of forces for each indenter radius was carried out in order to adapt to the magnitudes adopted in experimental evaluations.

Table 5.9: Dataset construction: range of applied forces for different indentation radii.

Radius (mm)	Lower Limit (N)	Upper Limit (N)
2.5	100	1000
5.0	500	1500
10	500	2500
15	500	3000

As can be seen, for the prediction of the displacement-force curve, there was no segregation of the curves in different datasets as performed in the study of the prediction of the stress-strain curve and presented in the table 5.8. The methodology used to predict the displacement-force curve, in contrast to the study conducted for the prediction of the stress-strain curve, can encompass a range of indenter radii, variations in the magnitude of the applied force, and variations in the properties of the materials while still providing good accuracy.

Chapter 6

Results and Discussions

This chapter aims to present the results for all evaluated cases: (1) prediction of the material parameters of the modified Mulliken-Boyce rheological model from the experimental stress-strain curve, (2) prediction of the stress-strain curve from the material parameters of the modified Mulliken-Boyce rheological model, (3) prediction of the stress-strain curve for the study of indentation in metals from the displacement-force curve, (4) prediction of the displacement-force curve and contact pressure obtained through indentation tests on metals from the mechanical properties of the material. In all results presented, the alpha network is represented by subindex 1.

A conclusion is presented at the end of this chapter and summarizes the main results obtained regarding the use of neural networks for predicting the desired information.

6.0.1 ANN applied for predicting the parameters of the modified Mulliken-Boyce model

Using data from simulations of uniaxial compression (performed via FEM), the AAN model was trained up to a maximum of 50000 epochs. It was identified, because a rate learning and batch descent algorithm optimizer was used, that the trained model shows improvement in the prediction until the last training epoch, however, the Loss Function does not present significant improvements that make it worthwhile to continue training for an epoch number over 50000.

Figures 6.1 to 6.6 present the results for the predictions made regarding the training dataset. The figure on the right shows the correlation between prediction and target. In this graph, the closer the data are to the line, the better the predictions, i.e., the smaller the dispersion and the closer the predictions are to the actual values. The graph on the left represents the relative percentage errors between prediction and target, such a graph facilitates the evaluation of the occurrence of greater errors in certain prediction ranges.
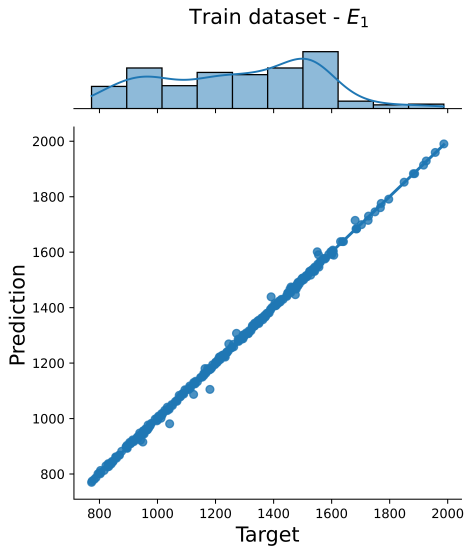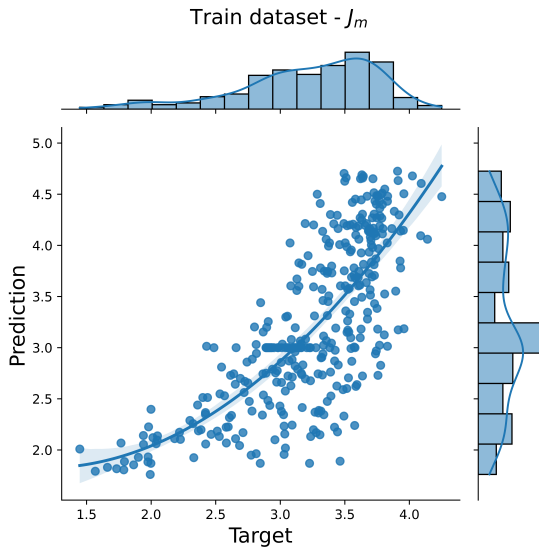
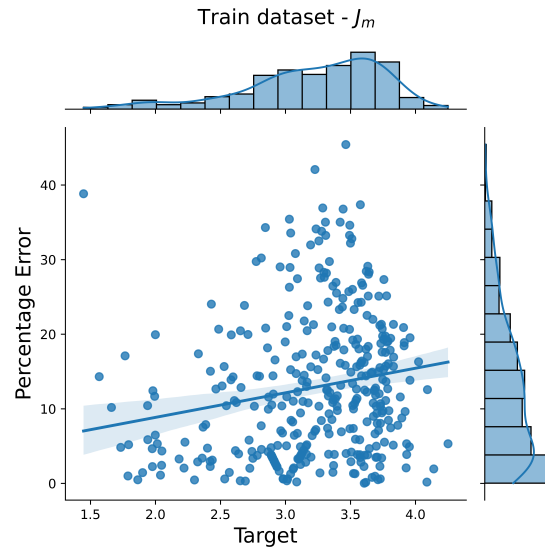(a) Comparative view between predicted and target data for the training dataset - E_1.
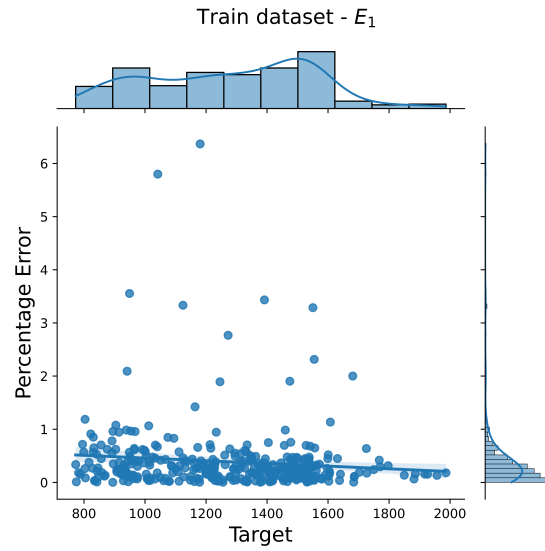
(b) Error between predicted and target data for the training dataset - E_1.

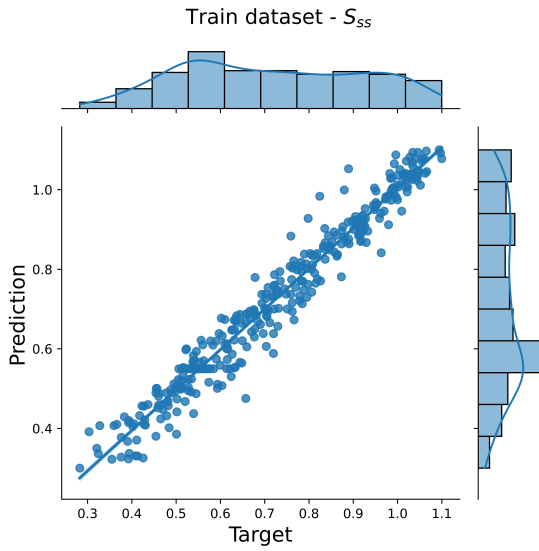Figure 6.1: Comparison between prediction and target for training dataset - E_1.

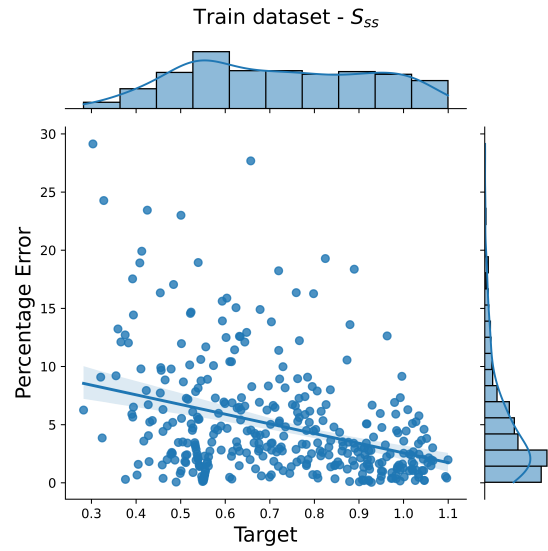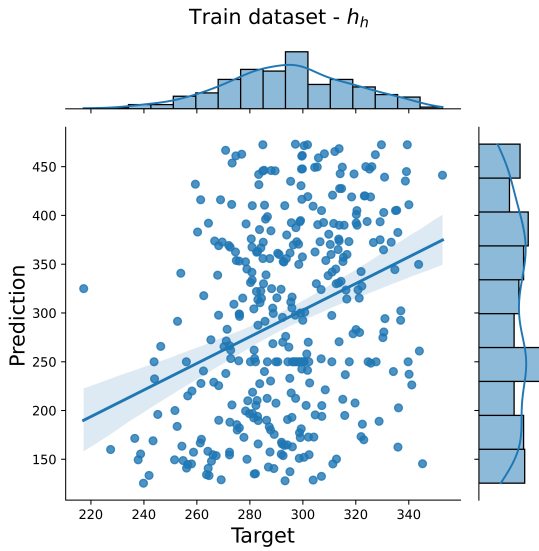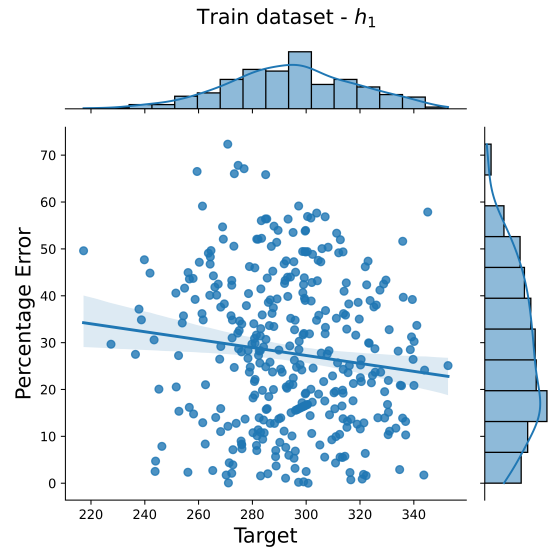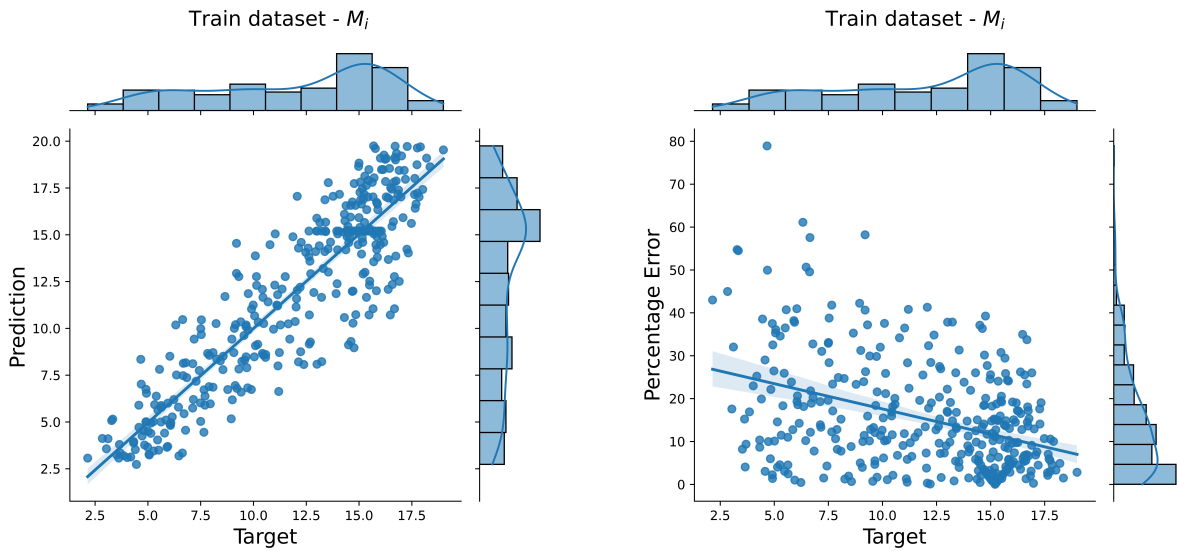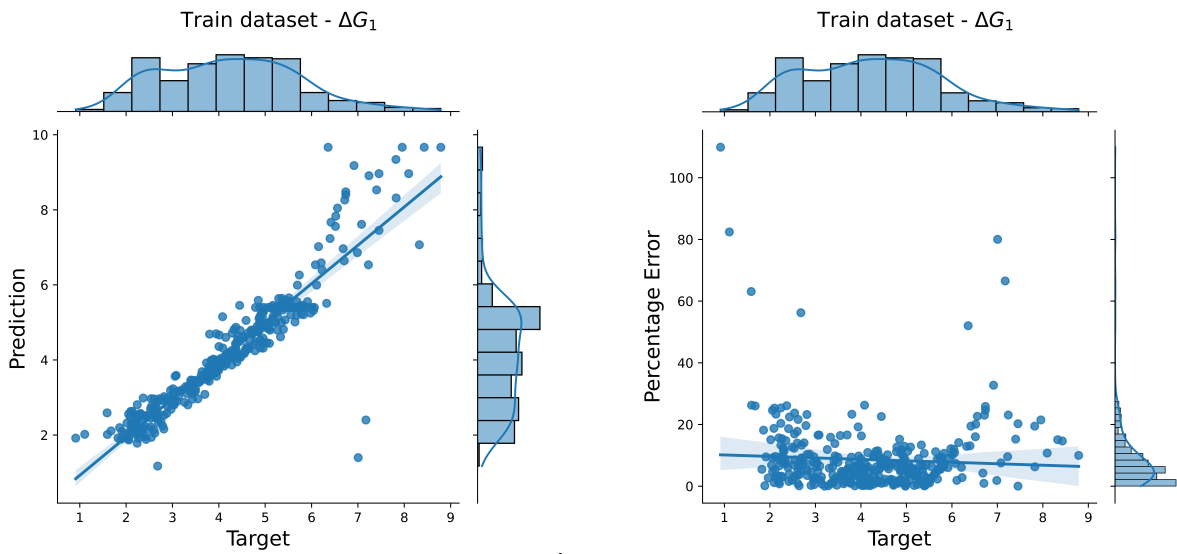(a) Comparative view between predicted and target data for the training dataset - J_m.

(b) Error between predicted and target data for the training dataset -J_m.

Figure 6.2: Comparison between prediction and target for training dataset - J_m.

(a) Comparative view between predicted and target data for the training dataset - S_{ss}.

(b) Error between predicted and target data for the training dataset - S_{ss}.

Figure 6.3: Comparison between prediction and target for training dataset - S_{ss}.

(a) Comparative view between predicted and target data for the training dataset - h_1.

(b) Error between predicted and target data for the training dataset - h_1.

Figure 6.4: Comparison between prediction and target for training dataset - h_1.

(a) Comparative view between predicted and target data for the training dataset - M_i.

(b) Error between predicted and target data for the training dataset - M_i.

Figure 6.5: Comparison between prediction and target for training dataset - M_i.

(a) Comparative view between predicted and target data for the training dataset - ΔG_1.

(b) Error between predicted and target data for the training dataset - ΔG_1.

Figure 6.6: Comparison between prediction and target for training dataset - ΔG_1.

Table 6.2 summarizes the main statistical parameters for each of the parameters considered in the prediction study, in order to facilitate the considerations presented below.

Table 6.1: Main statistical information of the predictions of the modified Mulliken-Boyce material parameters using the training dataset.

	mae	Max (%)	Mean (%)	Min (%)	mse	r^2
E_1	4.76	6.37	0.39	0.00	80.75	0.99
M_i	1.61	78.92	15.35	0.01	4.25	0.79
J_m	0.42	45.43	12.85	0.02	0.29	-
S_{ss}	0.03	29.14	4.92	0.04	0.00	0.95
h_1	105.95	194.01	35.62	0	16864.42	-
ΔG_1	0.35	109.89	8.58	0.02	0.39	0.82

From figures 6.1 to 6.6 and table 6.2 we can identify that the predictions made for E_1 are sufficiently accurate for the entire spectrum of evaluated simulations. For this parameter, the average error was 0.39% and the presence of larger errors happens sporadically, not occurring more frequently in a certain range of values.

The predictions made for parameter J_m have a different behavior than that found for E_1. In this second case, it is verified that the correlation between the prediction and the target can be better approximated by a quadratic function and as the parameter J_m grows, the accuracy of the prediction decreases. The mean error in this second case was 12.85%, however, high error magnitudes can be found, especially if J_m is greater than 3.0.

Predictions for S_{ss} behave similarly to the one found for E_1, where the correlation between prediction and target does not present a large dispersion. However, differently, the percentage error between prediction and target tends to decrease as S_{ss} increases. For this parameter, the average percentage error was 4.92%, a value close to that obtained for J_m.

The predictions made for h_1 had a much lower accuracy than the other parameters, as can be specifically identified in fig. 6.4. It can be seen from this figure that the data dispersion is much higher than that identified in the other parameters and that this does not occur specially in some range, but within the entire considered spectrum. As shown in tab. 6.2, the average percentage error was 35.62% and the maximum error reached 194.01%. Later, it will be better understood about the impact of such magnitude of errors for the description of the mechanical behavior.

Evaluating the results for M_i, the predictions are not as good as those obtained for E_1 and for S_{ss}, but also not as bad as those obtained for h_1. For such parameters, it is identified that the percentage error decreases as it approaches the maximum evaluated limit. The mean percentage error for M_i was 15.35%.

Finally, for the last evaluated parameter, the ΔG_1, it is also identified that the predictions have good accuracy, without large dispersion. For this parameter, the largest errors obtained occur exceptionally, in situations where ΔG_1 is very small or relatively high. The mean percentage error for ΔG_1 was equal to 8.58%.

As it is possible to identify by the distribution of the percentage errors for each of the evaluated parameters, for all cases, except for h_1, the data can be represented by a lognormal distribution, where the errors tend to be concentrated in a region close to 0. This fact is very evident for $E1$ and ΔG_1. With regard to h_1, the distribution is more similar to a rectangular distribution, that is, if a prediction is made, the probability of the error obtained being too high or too low is practically the same.

Given the data presented, it is possible to identify an acceptable prediction for the parameters of the modified Mulliken-Boyce numerical model of the training database. In all evaluated cases, the best predictions occurred within the composition range of the PC, ABS, and blends of the two materials. In general, the predictions that showed less accuracy are related to stress-strain curves very different from those of these materials. Among the evaluated parameters, those responsible for describing the linear phase are predicted with better accuracy than the others. For the parameters belonging to the yielding and non-linear hardening phase, a direct relationship was not observed. For the two predominant parameters in yielding phase, one of them showed good prediction accuracy (S_{ss}), while the other showed low prediction accuracy (h_1). For the prediction of the predominant parameters in the non-linear hardening phase, both present similar prediction accuracy, however the prediction accuracy in relation to the magnitude of the parameter presents different behavior.

Similarly, the comparative curves between the prediction and the target for the testing dataset are presented, a common practice in Machine Learning, which aims to verify the application of the ANN model for datasets different from those that the model was previously trained on. Such practice is presented as a confirmation of the effectiveness of the applied model, in addition to allowing, for example, the identification of possible overfitting.

Table 6.2: Main statistical information of the predictions of the modified Mulliken-Boyce material parameters using the testing dataset.

	mae	Max (%)	Mean (%)	Min (%)	mse	r^2
E_1	4.79	6.49	0.39	8.58	87.21	0.99
M_i	1.59	104.65	17.23	0.10	4.22	0.77
J_m	0.45	45.55	13.91	0.25	0.33	-
S_{ss}	0.03	24.99	5.34	0.00	0.00	0.95
h_1	96.11	125.87	32.10	0.57	14368.77	-
ΔG_1	0.37	53.51	8.67	0.10	0.37	0.81
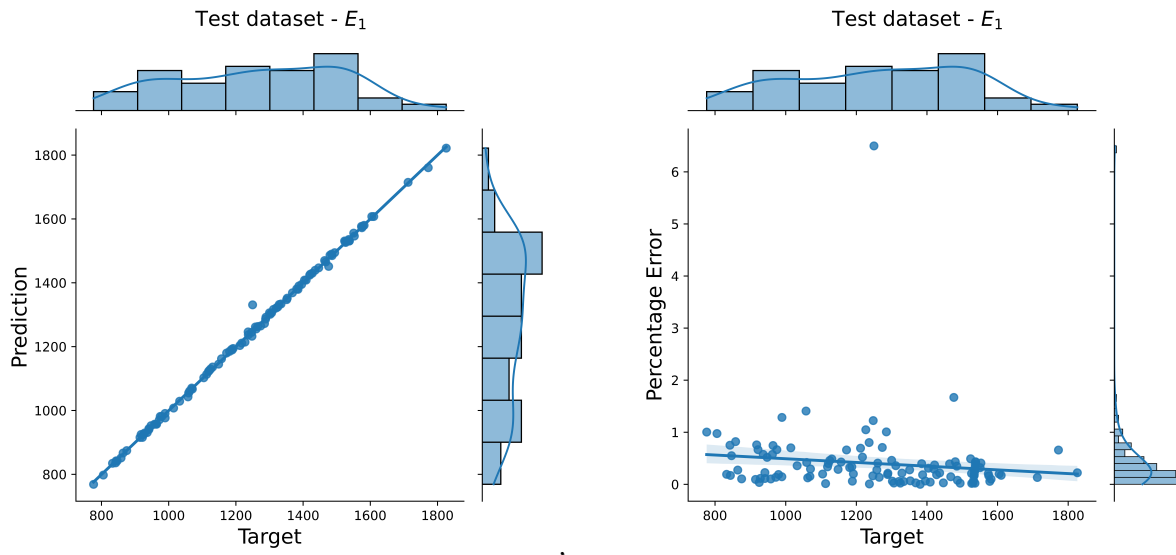
(a) Comparative view between predicted and target data for the testing dataset - E_1.

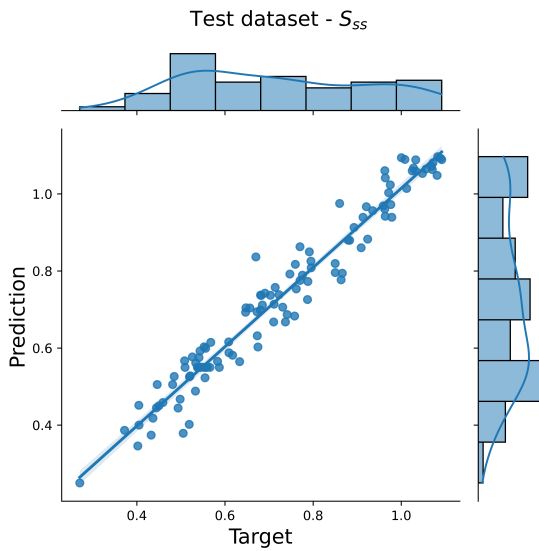(b) Error between predicted and target data for the testing dataset - E_1.

Figure 6.7: Comparison between prediction and target for testing dataset - E_1.
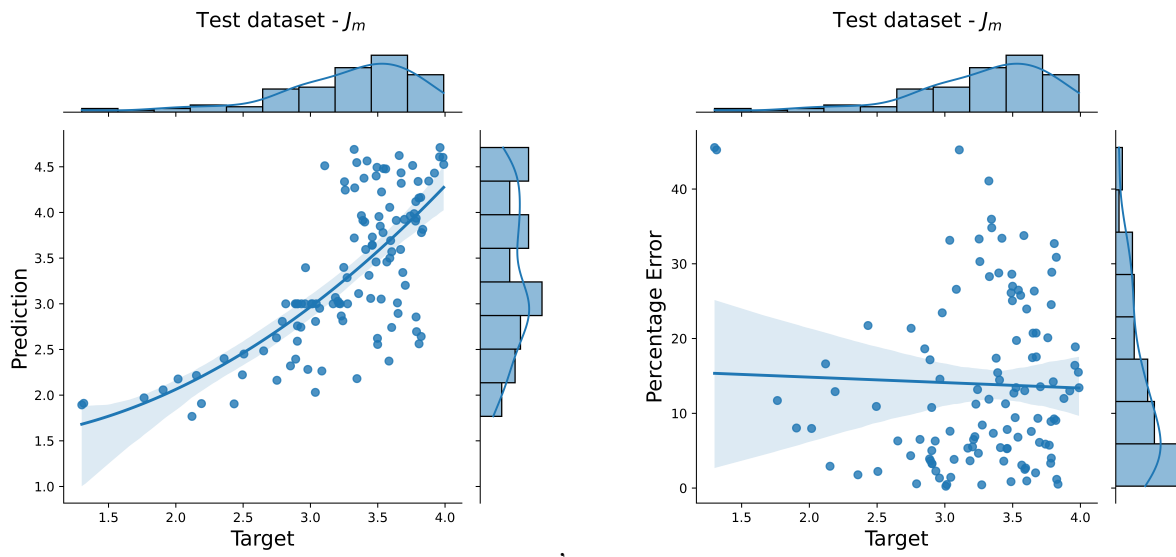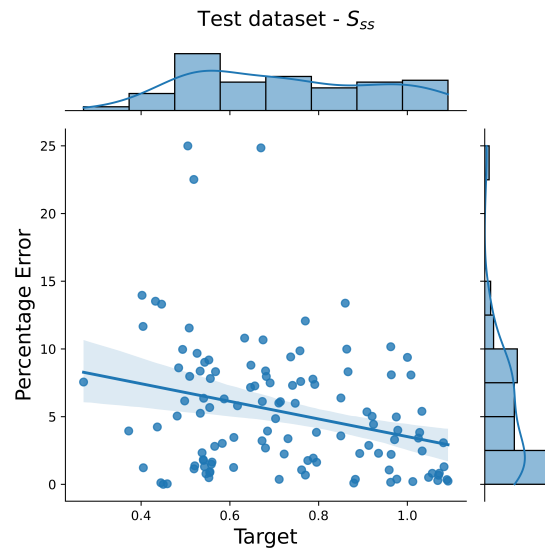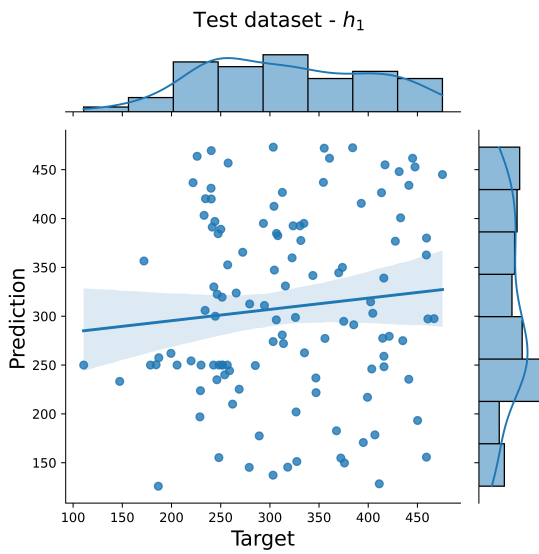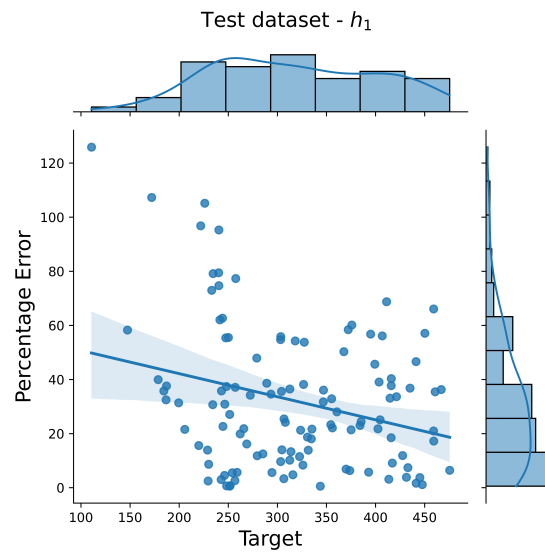

(a) Comparative view between predicted and target data for the testing dataset - J_m.

(b) Error between predicted and target data for the testing dataset -J_m.

Figure 6.8: Comparison between prediction and target for testing dataset - J_m.

(a) Comparative view between predicted and target data for the testing dataset - S_{ss}.

(b) Error between predicted and target data for the testing dataset -S_{ss}.

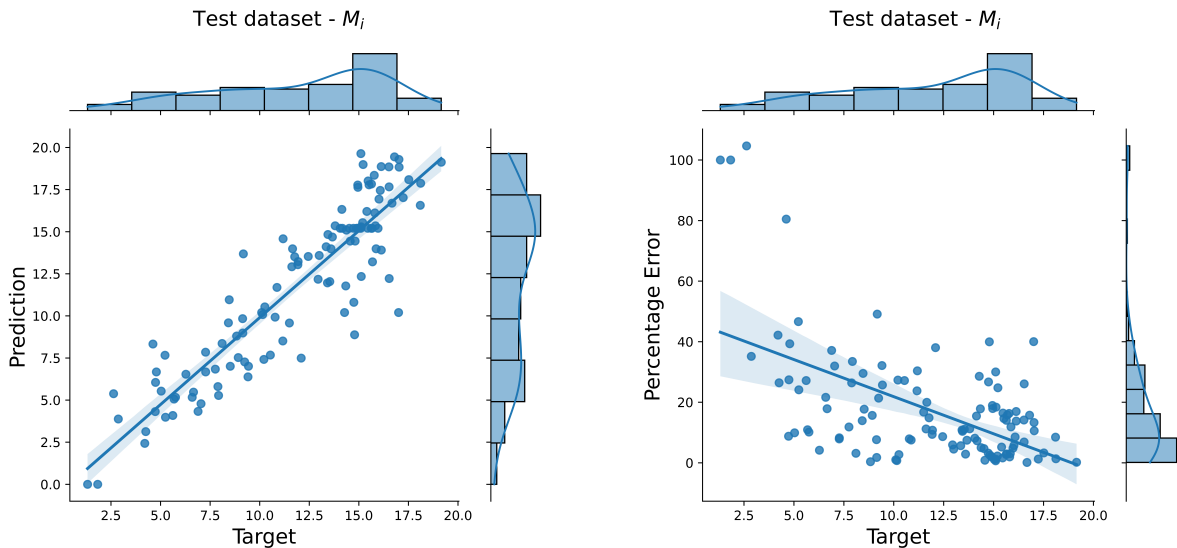Figure 6.9: Comparison between prediction and target for testing dataset - S_{ss}.

(a) Comparative view between testing and target data for the training dataset - h_1.

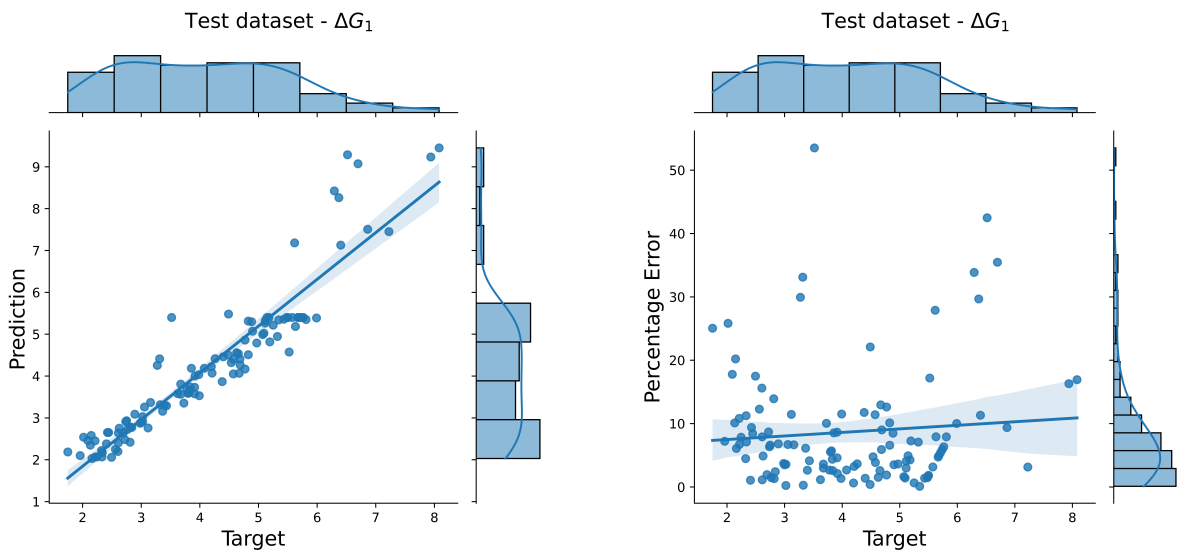(b) Error between predicted and target data for the testing dataset -h_1.

Figure 6.10: Comparison between prediction and target for testing dataset - h_1.

(a) Comparative view between predicted and target data for the testing dataset - M_i.

(b) Error between predicted and target data for the testing dataset -M_i.

Figure 6.11: Comparison between prediction and target for testing dataset - M_i.

(a) Comparative view between predicted and target data for the testing dataset - ΔG_1.

(b) Error between predicted and target data for the testing dataset -ΔG_1.

Figure 6.12: Comparison between prediction and target for testing dataset - ΔG_1.

When evaluating the predictions made for the testing dataset (fig.6.7 to 6.12), we can see that the results are in agreement with the results obtained for the training dataset, all metrics are quite similar. The biggest divergences observed is that in the training dataset, the prediction errors of J_m tend to be greater the greater its value, whereas in the testing dataset this fact is not observed. Another characteristic observed is that the greater the J_m, the more dispersed are the percentage errors between prediction and target.

In order to evaluate the performance of the ANN model for predicting the material parameters of the modified Mulliken-Boyce model, four different materials were tested: PC, ABS PC/ABS 60:40 and PC/ABS 80:20. It should be noted that the numerical stress-strain curves of these materials were not considered during the training phase of the ANN model, in order not to bias the results. To carry out this evaluation, the experimental stress-strain curve for such materials was imputed in the neural network, thus generating predictions of the relevant material parameters. Subsequently, the commercial software ABAQUS® was used to generate the stress-strain curve from the predicted material parameters. Thus, the curve called prediction in figure 6.13 represent the curves obtained via FEM from the material parameters predicted by the neural network.

The methodology presented above makes it possible to assess how satisfactory the predictions of the material parameters are. If the stress-strain curves from the obtained material parameters present satisfactory accuracy, it is possible to state that the use of the neural network can be used as a computational tool that helps or replaces the calibration procedure of numerical models, a step that generally requires a lot of time processing due to the recursive process to obtain the ideal parameters.
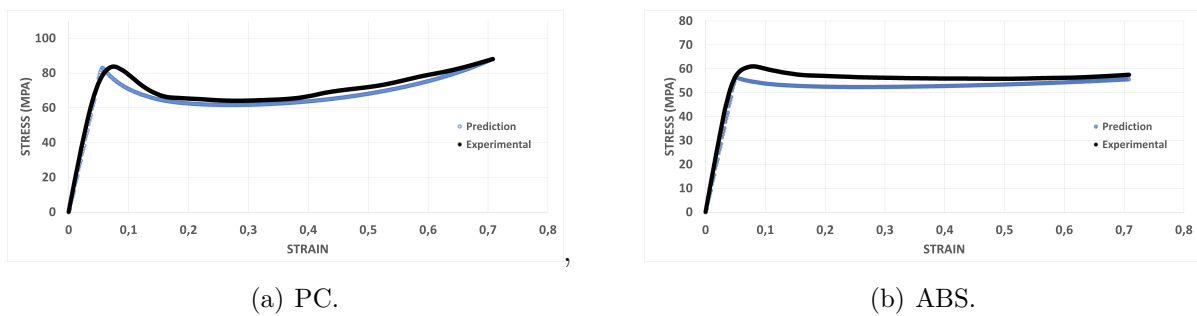

(a) PC.   (b) ABS.

Figure 6.13: Comparison between: stress-strain curve obtained via material parameters predicted by ANN and experimental curve.

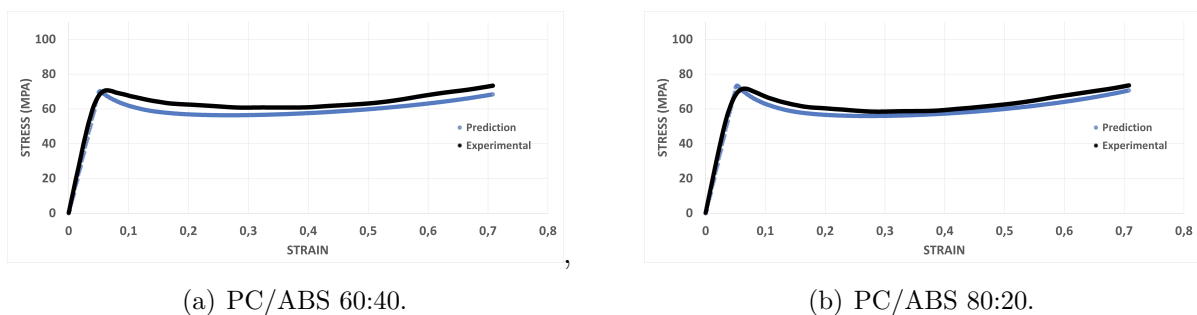(a) PC/ABS 60:40.   (b) PC/ABS 80:20.

Figure 6.14: Comparison between: stress-strain curve obtained via material parameters predicted by ANN and experimental curve - Blends.

The predictions of the material parameters via the ANN model for PC, ABS, PC/ABS 60:40 and PC/ABS 80:20 satisfactorily represent the experimental results (6.13 and 6.14).

In all evaluated cases, the predictions of all points on the stress-strain curve are similar to the targets. By tab. 6.3, it is identified that the mean difference in MPa between the predicted curve and the experimental curve was equal to 3.46 for PC, 3.41 for ABS, 4.56 for PC/ABS 60:40 and 3.18 for PC/ABS 80.20. In all evaluated cases, the greatest difference occurred in PC and was equal to 8.64 MPa. For all predicted curves, it is identified that the greatest dissimilarity between prediction and target occurred at the beginning of the yield phase and this fact is more evident for PC and ABS than for the other materials. The explanation for the largest errors being present in such a region is because the largest prediction errors occurred for the material parameter h_1, which is mainly responsible for the description of the yield phase. The explanation for the ABS presenting the largest errors in the yielding phase than the others is because the parameter h_1 has a greater magnitude than the other evaluated materials and due to this, this parameter has a greater impact on the description of the entire stress-stress curve.

Table 6.3: Percentage errors between the curve obtained through the prediction of the material parameters and the experimental curve.

	Mean Error (MPa)	Max Error (MPa)	r^2
PC	3.46	8.64	0.98
ABS	3.41	7.00	0.97
PC/ABS 60:40	4.56	8.60	0.98
PC/ABS 80:20	3.18	7.97	0.98

When comparing the manual calibration process presented in item 5.1.1.2 and the calibration process carried out through the proposed neural network, we can see that the results are equivalent. Taking the value of r^2 as a parameter, the curves obtained through the calibration process with the aid of neural networks presented inferior performance only for the ABS, where the manual calibration process presented r^2 equals 0.99 and the through the neural network 0.97. For the blends PC/ABS 60:40 and 60:20 the values of r^2 were identical and for the PC there was an improvement in the r^2 of 0.02.

Given the results presented, it is possible to identify the contribution of the use of neural networks to help the calibration process of the modified Mulliken-Boyce model. The calibration process of this numerical model is an arduous process that requires a lot of processing time, each analysis takes approximately 6h (in the machine used to perform the simulations) and must be repeated several times until the error is small enough (requirement). The use of the proposed methodology, based on the implementation of neural networks, makes the calibration process more agile (after generating the neural network, it only takes a few seconds for the predictions to be carried out) and with good performance. It should be noted that the variation obtained between the predicted and experimental stress-strain curves was lower than the variations verified during the experimental tests for

the description of the mechanical behavior of the evaluated materials due to variations in polymer properties between different specimens.

6.0.2 ANN applied for predicting the stress-strain curve of the modified Mulliken-Boyce model

As previously mentioned in Chapter 5, for the prediction of the stress-strain curve, instead of using the material parameters of the modified Mulliken-Boyce model as output, the stress-strain curve is considered. So, material parameters are used as input. The modification of the layout (present in 5.2.1.2) and the maximum amount of epoch allowed, in this case equal to 10^5, are the main modifications regarding the neural network adopted for the prediction of the stress-strain curve.

The main consideration taken for the prediction of the stress-strain curve is that the prediction is performed for all ordered stress-strain pairs that make up the curve. This second proposed neural network aims to identify the possibility of using neural networks to reproduce the results obtained by well-established techniques, such as the FEM.
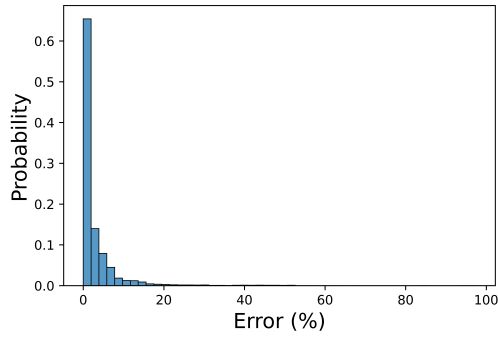
As the percentage error between the prediction and the target can be evaluated for each ordered pair of the stress-strain curve, the figures below show the distribution of these errors for all stress-strain curves considered during the evaluation, it allows the evaluation of the distribution of these errors for several curves in parallel. The three datasets considered are: training dataset, training dataset 1 and training dataset 2. The difference between testing dataset 1 and testing dataset 2 lies in the fact that the first one is used to check the accuracy of the model during the model training and the second one is not considered. In order to make the distribution of errors more visible, the distribution of the logarithm of errors is also verified.
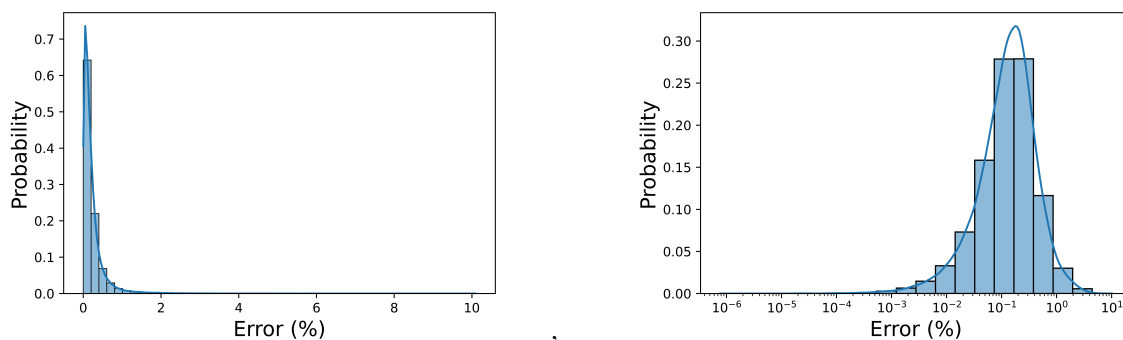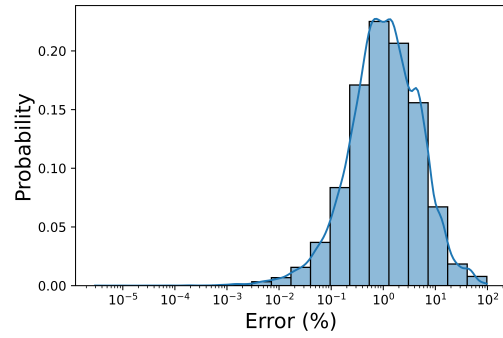

(a) Distribution of percentage errors between prediction and target.

(b) Distribution of the logarithm of percentage errors between prediction and target.

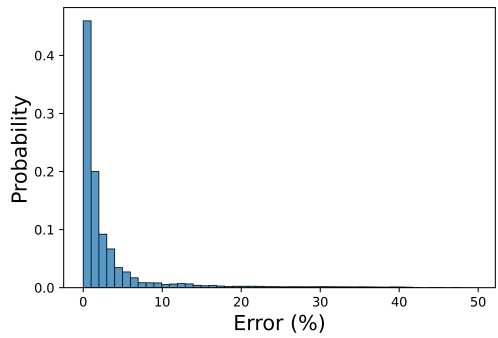Figure 6.15: Percentage errors between prediction and target - Training dataset.

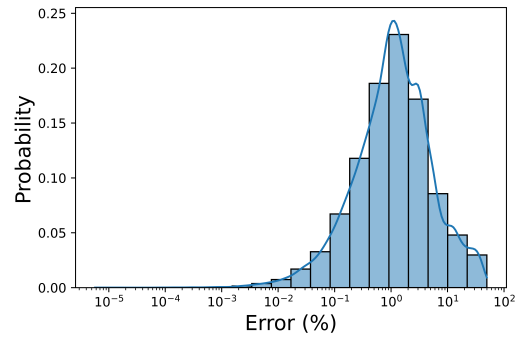(a) Distribution of percentage errors between prediction and target.

(b) Distribution of the logarithm of percentage errors between prediction and target.

Figure 6.16: Percentage errors between prediction and target - Testing dataset 1.

(a) Distribution of percentage errors between prediction and target.

(b) Distribution of the logarithm of percentage errors between prediction and target.

Figure 6.17: Percentage errors between prediction and target - Testing dataset 2.

From the figures 6.15, 6.16 and 6.17 it can be seen that for the three datasets considered, the average percentage errors are concentrated on the left end, i.e., values closest to zero and that the distribution has characteristics similar to an exponential distribution with a very sharp drop. These figures also show that the training dataset is the one with the smallest outliers, the maximum errors are close to 10 %. For testing dataset 1 and 2, the outliers are of greater magnitude, around 100% and 50%, respectively. In view of such observations, there is a prior idea that there is a drop in the performance of the ANN model when predictions are made for cases not considered during the training phase, something expected.

In order to further evaluate the agent that generates such outliers, it was separately evaluated whether there is any relationship between the value of the material parameter considered and the average percentage error (average value per stress-strain curve). Thus, figure 6.18 presents the mean percentage error for each of the studied parameters. In this

figure, the evaluation is performed only for training dataset 2, since it is the dataset defined to evaluate the performance of the proposed neural network. It should be noted that all subsequent evaluations will also be performed solely for that dataset.
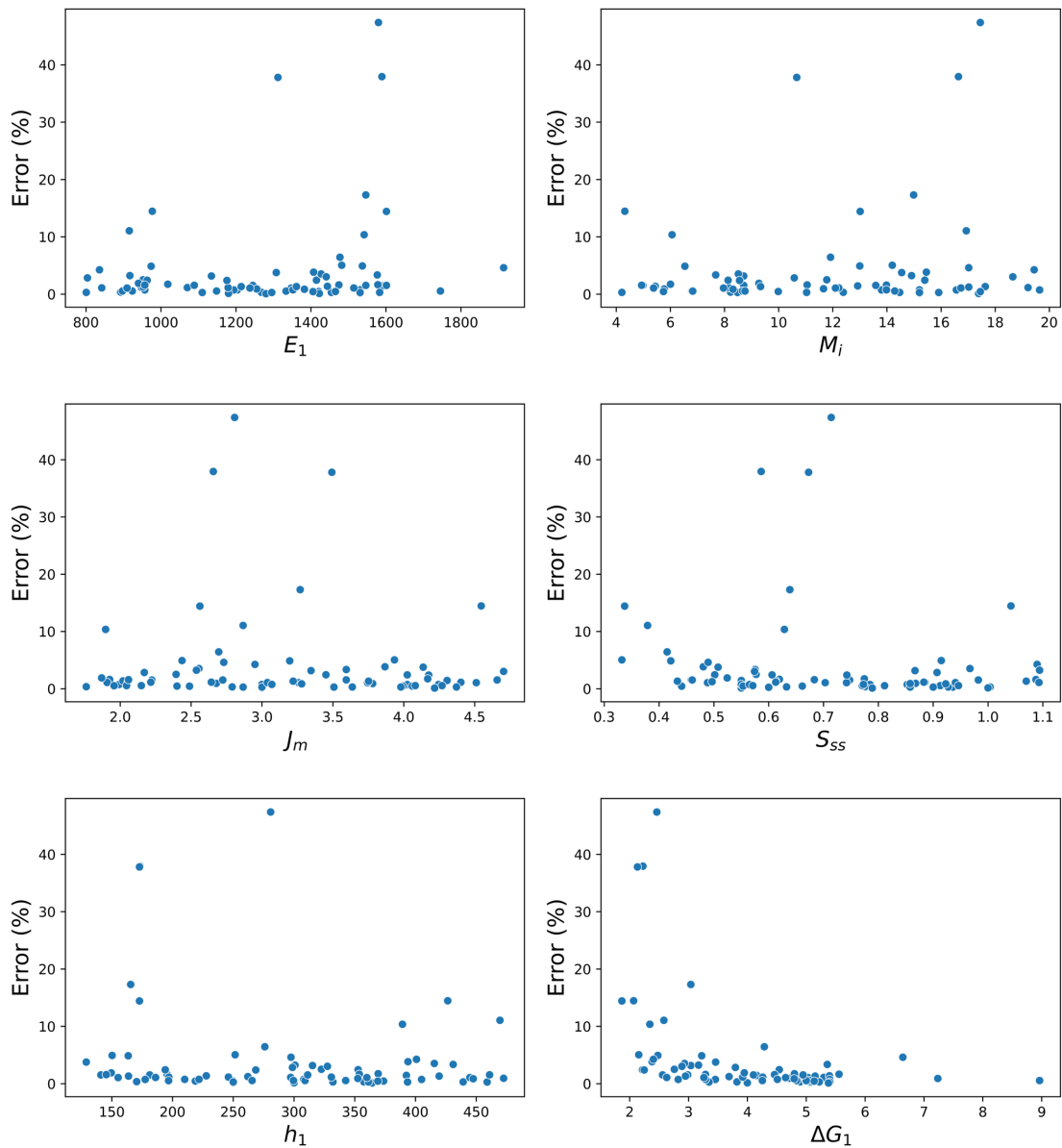

Figure 6.18: Correlation between average percentage error and magnitude of the material parameter.

From the figure 6.18 it is possible to identify that the largest percentage errors occur mainly in the following situations: (1) low magnitudes of ΔG_1 and (2) E_1 close to 1600 MPa. Furthermore, it is also possible to identify that the average percentage error tends to decrease the higher the ΔG_1 is. For the other parameters, the presence of large errors concentrated in certain regions of the graphs was not identified. The fact that both ΔG_1 and E_1 show errors of greater magnitude concentrated in certain intervals is possibly because

both describe at the same time the behavior of the linear phase of the material. In this way, both are not necessarily the causative agent of the errors of greater magnitude, there is the possibility of being only one of them.

Deeper analyzes made it possible to identify that the real agent causing the high average percentage errors in some predictions was the parameter ΔG_1, a fact that was clearly identified when investigating the behavior of the predictions of the stress-strain curve obtained by the neural network. When evaluating the stress-strain curves for the worst predictions, it was identified that in all cases the yield stress was quite low (few representative cases in the training and test datasets). It should be remembered that the parameter ΔG_1 is mainly responsible for defining the yield stress in the modified Mulliken-Boyce model.

According to the observation presented above, it is possible to state that the proposed neural network for predicting the stress-strain curve is suitable for values of ΔG_1 greater than 3×10^{-19}.

In order to evaluate the performance of the proposed neural network, the following figures (Fig. 6.19 to 6.21) show a comparative graph between the stress-strain curve predicted by the neural network and the stress-strain curve obtained via FEM (for each graph, the comparison between the prediction and the curve via FEM are obtained by the same material parameters). The graphs show three different situations. Figure 6.19 shows the two worst predictions and represents cases where $\Delta G_1 < 3 \times 10^{-19}$. Figure 6.20 presents the worst predictions excluding outliers ($\Delta G_1 > 3 \times 10^{-19}$) and figure 6.21) presents the best predictions obtained by the neural network.
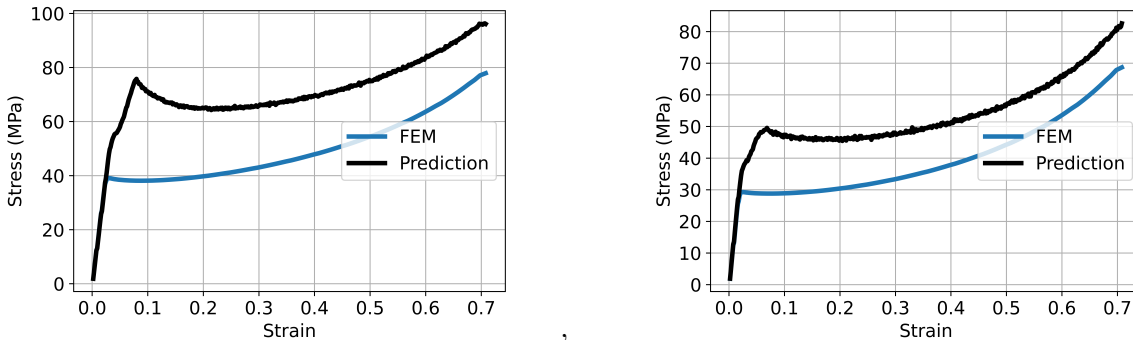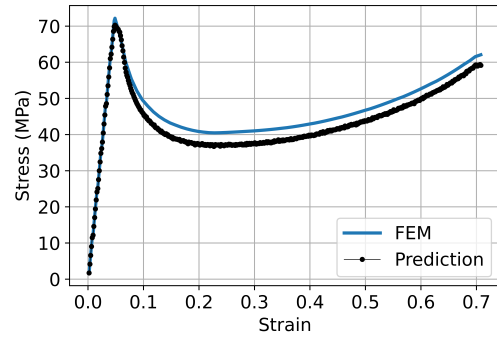

(a) Worst stress-strain curve prediction.   (b) Second worst stress-strain curve prediction.

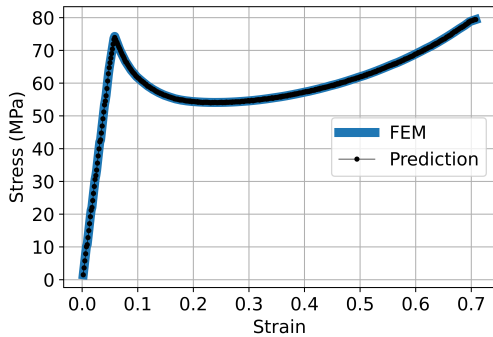Figure 6.19: Worst stress-strain curves predictions by ANN - outliers.
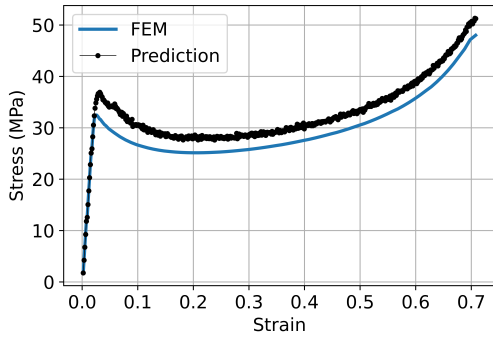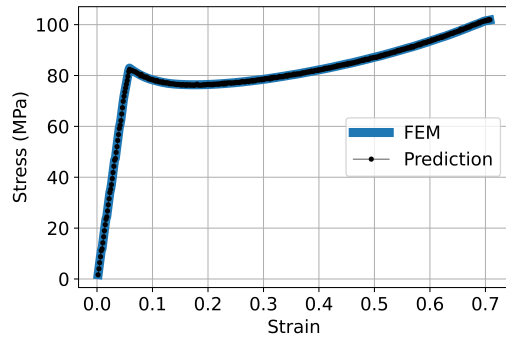
(a) Worst stress-strain curve prediction.

(b) Second worst stress-strain curve prediction.

Figure 6.20: Worst stress-strain curves predictions by ANN - excluding outliers.

(a) Best stress-strain curve prediction.

(b) Second best stress-strain curve prediction.

Figure 6.21: Best stress-strain curves predictions by ANN.

Table 6.4: Mean and maximum error for stress-strain curve prediction.

	Max Error (%)	Mean Error (%)
Training Dataset	1.46	0.23
Testing Dataset 1	7.64	2.89
Testing Dataset 2	9.05	3.82

Table 6.4 presents a summary of some statistical parameters for the training and testing datasets. the Mean Error (%) represents the average of the average percentage error obtained in each predicted stress-strain curve and the Max Error (%) represents the average of the maximum percentage error found for each predicted stress-strain curve. By these parameters there is an increase both in the Mean Error (%) and in the Max Error (%) if the training and testing dataset are compared. However, it is identified that the Mean Error (%) observed for testing dataset 2 is relatively low, i.e., the neural network can reproduce the data obtained via FEM with good accuracy. In most of the evaluated cases, the mean

percentage difference between the two methods (FEM and ANN) is less than 5% (variations in experimental tests can present greater errors than those identified using a surrogate model).

6.1   Indentation in Metals

6.1.1   Prediction of the Stress-Strain curve from Displacement-Force Curve

The prediction of the stress-strain curve using displacement-force data can be performed using different methods. One method is the prediction of material parameters (strength coefficient, hardening exponent, modulus of elasticity and yield stress) followed by the determination of the stress-strain curve with a chosen rheological model. Another method is the direct prediction of the stress-strain data points through a rheological model. Preliminary studies were carried out (with 300 points for each curve) to access the best alternative. In view of this comparative analysis between the two mentioned methods, the first one had a much higher error than the second: in some cases, the errors reached levels above 200%. Thus, the second method (use of stress-strain curve) is employed in all ANN models and predictions reported here.

As can be identified in the items that follow, results are presented for four different cases, and for each case, different considerations are taken into account. Each different configuration encompasses the consideration taken in the previous model, that is, the ANN-C model necessarily encompasses the considerations of the ANN-B model, and the ANN-D model necessarily encompasses the considerations of the ANN-C and ANN-B model. The idealization of the models was carried out chronologically, so it is possible to identify the impact on predictions if such consideration is taken. The identification and discussion of the error observed in the four proposed ANN models will be discussed.

Fig. 6.22 shows, for each strategy, the error distributions in relation to the strain. In the following items, the stress-strain curve predictions obtained using the four ANN models are discussed and compared. As can be seen during the results, with each consideration made, the better predictions will be made, however, the more restricted the application of the neural network becomes.
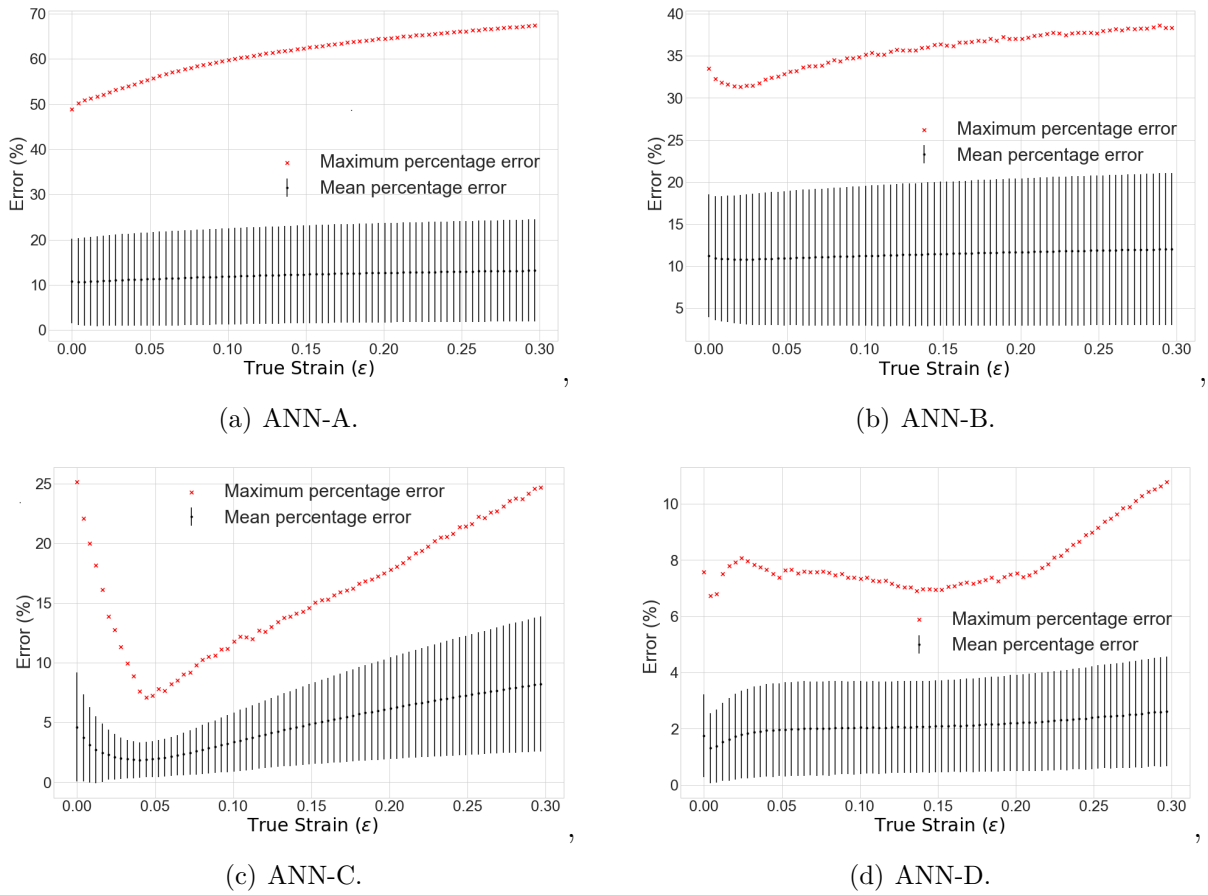
(a) ANN-A.

(b) ANN-B.

(c) ANN-C.

(d) ANN-D.

Figure 6.22: Mean and maximum percentage error for all ML prediction points.

6.1.1.1 ANN-A predictions

The mean percentage error, the standard deviation and the maximum error for each prediction point of the stress-strain curve employing ANN-A are shown in Fig. 6.22(a). A large percentage error is observed in all data points. Moreover, as the strain increases so does the maximum percentage error between prediction and target. The maximum errors are presented as outliers that reach percentage errors close to 68%, which might be considered as unacceptable for most engineering applications. Nevertheless, the ANN-A showed a mean percentage error and a standard deviation of approximately 10%, meaning that when it works (which happens in approximately 32% of the cases) it does with a reasonable precision.

6.1.1.2 ANN-B predictions

In the ANN-B strategy, as previously mentioned, the applied compressive load is kept constant at the maximum value of the range chosen for that parameter. The mechanical properties and the indenter's radii are kept as variables. As expected, due to the reduction

of variables, an improvement in the predictions is observed. However, a high value of maximum percentage error remains. As can be identified in Fig. 6.22(b), the main aspect that differentiates it from the ANN-A is that the predictions have smaller outliers. In this case, the maximum errors reached values close to 40%. This model also shows a different behavior when compared to the ANN-A: It initially presents a slight decrease in the maximum percentage error, but soon after there is an increase as the true strain increases. An evaluation of the mean percentage error shows an improvement when compared to the ANN-A (same standard deviation of approximately 10%, but standard deviations of 5%).

6.1.1.3 ANN-C predictions

In the ANN-C, the material properties are the only variables. Fig. 6.22(c) shows the results for this third model. The values obtained for the mean and maximum errors, as well as the standard deviations, show a contrasting behavior when compared to the two previous models. The errors and deviations decrease considerably until the strain point close to 5%, when a somewhat linear increase of both parameters is noted. When evaluating the predicted stress-strain curves and comparing them to the targets, such an inflection point occurs near the beginning of the material's inelastic zone. This model presents significant improvement in the prediction mainly due to the presence of fewer variables since it does not consider variations in the indenter and in the magnitude of applied force. The average errors are in the range of 2-8%, the maximum standard deviation obtained is approximately 6% and the maximum error is between 8-25%. Therefore, this model is suitable for the small strains analysis of most metallic materials.

6.1.1.4 ANN-D predictions

The ANN-D can be interpreted as an extended version of ANN-C. As seen in Fig. 6.22(d), this strategy leads to a significant overall improvement of all error indicators. From the results obtained, it is possible to point out a significant improvement in the obtained predictions, with a considerable drop in both the average error, maximum error, and standard deviation. The biggest error obtained was approximately 21% at the beginning of the description of the stress-strain curve. Since the magnitude is negligible in such a region if compared to the other levels during the description of the curve, this value can be considered as less relevant. Considering the plastic zone of the material, the maximum error in the prediction was approximately 15.5%. When evaluating the maximum mean error, it occurred at the end of the description of the stress-strain curve, with a value close to 3.5%, with a standard deviation of approximately 2.5%.

The proposition of a model composed of different neural networks, each one used for a certain range of material properties, was defined after evaluating the impact of the ma-

terial property on the errors obtained by the prediction (considering the 75th percentile). Moreover, as the increase in errors is verified in the inelastic zone, the evaluation considered only the parameters pertinent to the inelastic behavior: strength coefficient, K, and hardening exponent, n. Fig. 6.23 presents the magnitude of the average error in relation to the magnitude of the strain hardening exponent, n, and the strength coefficient, K. Based on the correlations, the occurrence of greater magnitude of average error is found primarily in situations of: (1) low strength coefficient and (2) high strength coefficient and high strain hardening exponent. The smallest errors were found primarily outside these testing extremes.
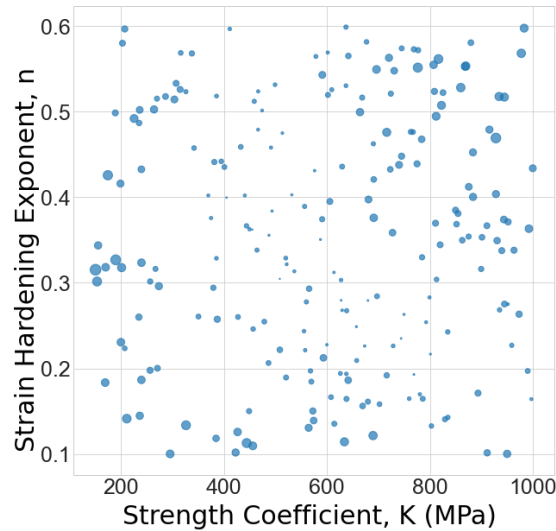

Figure 6.23: Correlation between mean percentage prediction error, strain hardening exponent and strength coefficient.

A separate evaluation of the prediction error and magnitude of the parameter K and n was also carried out. Fig. 6.24(a) and Fig. 6.24(b) were obtained from the implementation of a clustering analysis, each color represents a different cluster. The aim of such implementation was to identify the presence of groups within the data. For this purpose, a K-means clustering coupled with an unsupervised learning technique was implemented. This technique consists of an iterative process to assign each data point to a group where data points are grouped based on the similarity of position of the geometric representation space. Herein, five different groups within the sample space are defined.

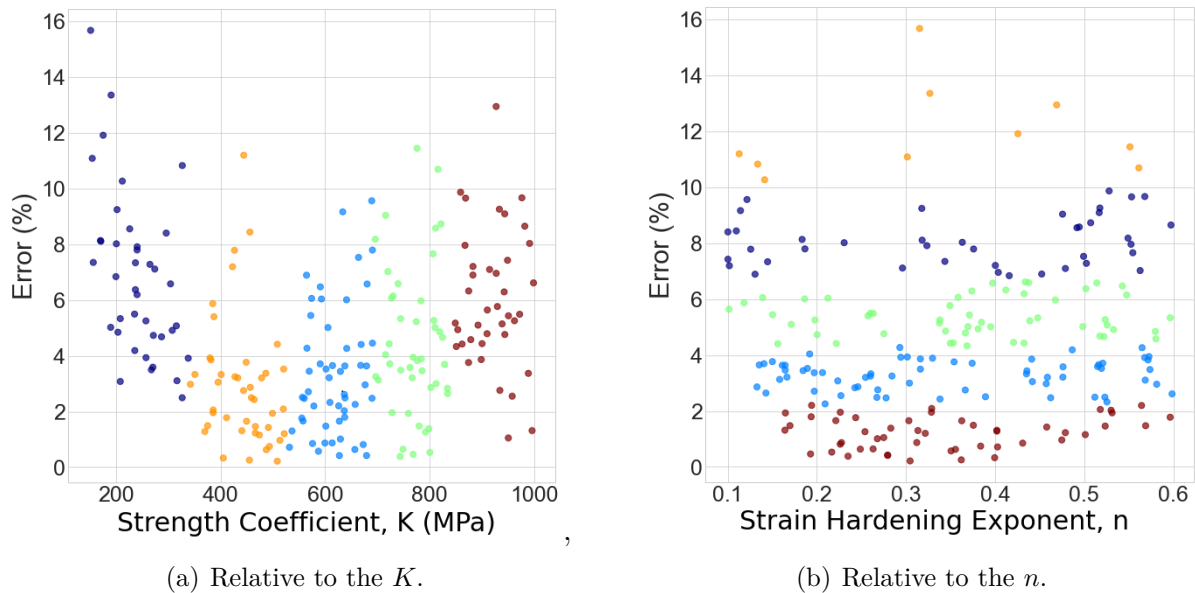(a) Relative to the K.   (b) Relative to the n.

Figure 6.24: Clustering errors.

Fig. 6.24(a) and Fig. 6.24(b), clearly shows that there are groups of average percentage errors in relation to different magnitudes of strength coefficient. Therefore, the errors obtained must have a relationship with the range of parameter K. In opposition, when evaluating the results obtained for n, it is not possible to identify a clear correlation. As can see in Fig. 6.24(b), the presence of groups occurs horizontally (i.e. for the same interval of such parameter, different groups of mean percentage errors were obtained). Therefore, the ANN-D has been implemented using five different strength coefficient ranges: 150-300 MPa, 300-450 MPa, 450-600 MPa, 650-850 MPa and 850-1000 MPa. Nevertheless, to ensure a consistent performance evaluation, it should be noted that all other parameters relevant to the ML training are identical to the other models.

Since the ANN-D shows the best results, an additional performance analysis (using displacement-force curves not considered during the training of the ANN model) was carried-out. The best and worst predictions, for each range of K, are illustrated in Fig. 6.25. It should be noted that each dataset is composed solely of curves referring to the relevant strength coefficient range and that the best and worst prediction for each range necessarily uses the same neural network for different displacement-force curves present in the considered dataset. The best predictions for all K ranges are almost identical to the target. The worst predictions showed no specific trend, they could occur at higher or lower stress levels than the ones observed in the target. For instance, a still good prediction is seen in Fig. 6.25(b), while in Fig. 6.25(c) the prediction is slightly shifted and in Fig. 6.25(d) a reasonable description is provided up until a certain strain level is reached.
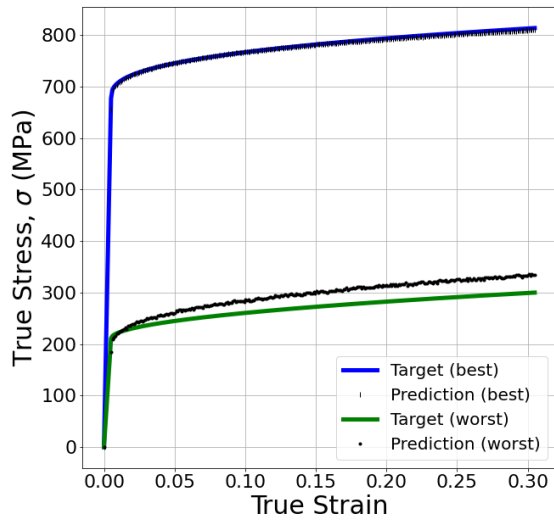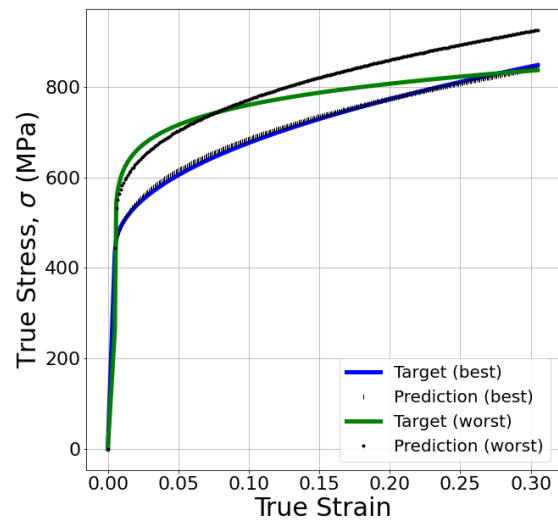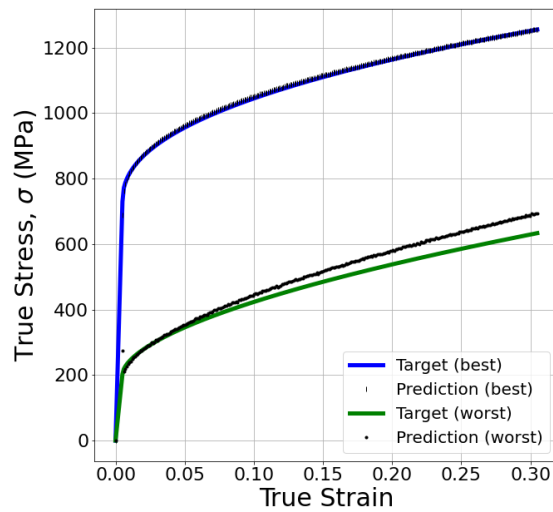
(a) 150-300 MPa range.
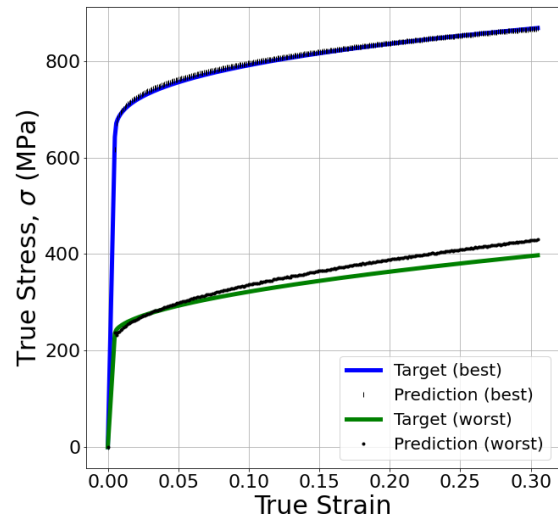
(b) 300-450 MPa range.
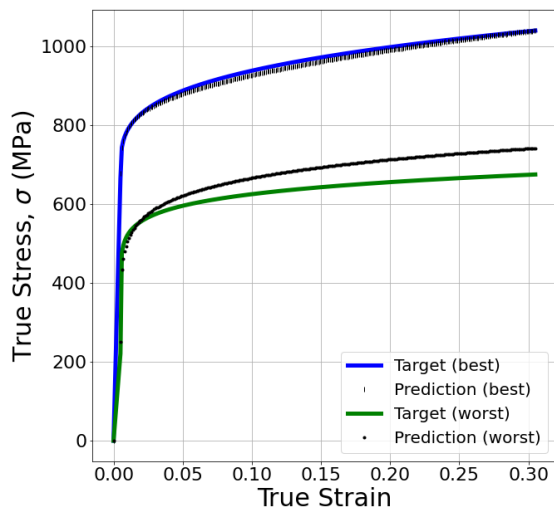
(c) 450-600 MPa range.

(d) 650-850 MPa range.

(e) 850-1000 MPa range.

Figure 6.25: Best and Worst ANN-D stress-strain predictions for each range of K.

Table 6.5 summarizes the data related to the mean, maximum and standard deviation for the plasticity zone of the stress-strain curve for each of the models presented.

Table 6.5: Errors observed at the inelastic zone of each ANN model.

Model	Mean Error (%)	Maximum Error (%)	Standard Deviation
ANN-A	13.20	67.49	11.30
ANN-B	12.02	38.45	9.05
ANN-C	8.24	24.80	5.67
ANN-D	2.87	15.90	2.41

6.1.2 Prediction of the Displacement-Force Curve and Contact Pressure from the Material Properties and Boundary Conditions

As shown in 5.2.2, the Young's modulus, yield stress, strength coefficient, and hardening exponent of the material, as well as the boundary conditions (force and indenter radius), were used to predict the displacement-force curve and contact pressure for indentation tests. It should be noted that the input dataset was not the same one used to predict the stress-strain curve because, in accordance with a pre-established rule also presented in item 5.2.2, the neural network used to predict the displacement-force curve takes variations in force and indenter radius into account.

In order to evaluate the performance, a random dataset not considered during training was studied on the ANN model for predicting the displacement-force curve. Figure 6.26 shows the largest prediction errors obtained by each predicted curve in relation to the considered parameter. As can be seen, the largest percentage errors are exceptions, and the maximum error is relatively low (close to 16%).

(a) Yield Stress.

(b) Young's Modulus.

(c) Hardening Exponent.

(d) Strength Coefficent.

(e) Force

(f) Identer Radius.
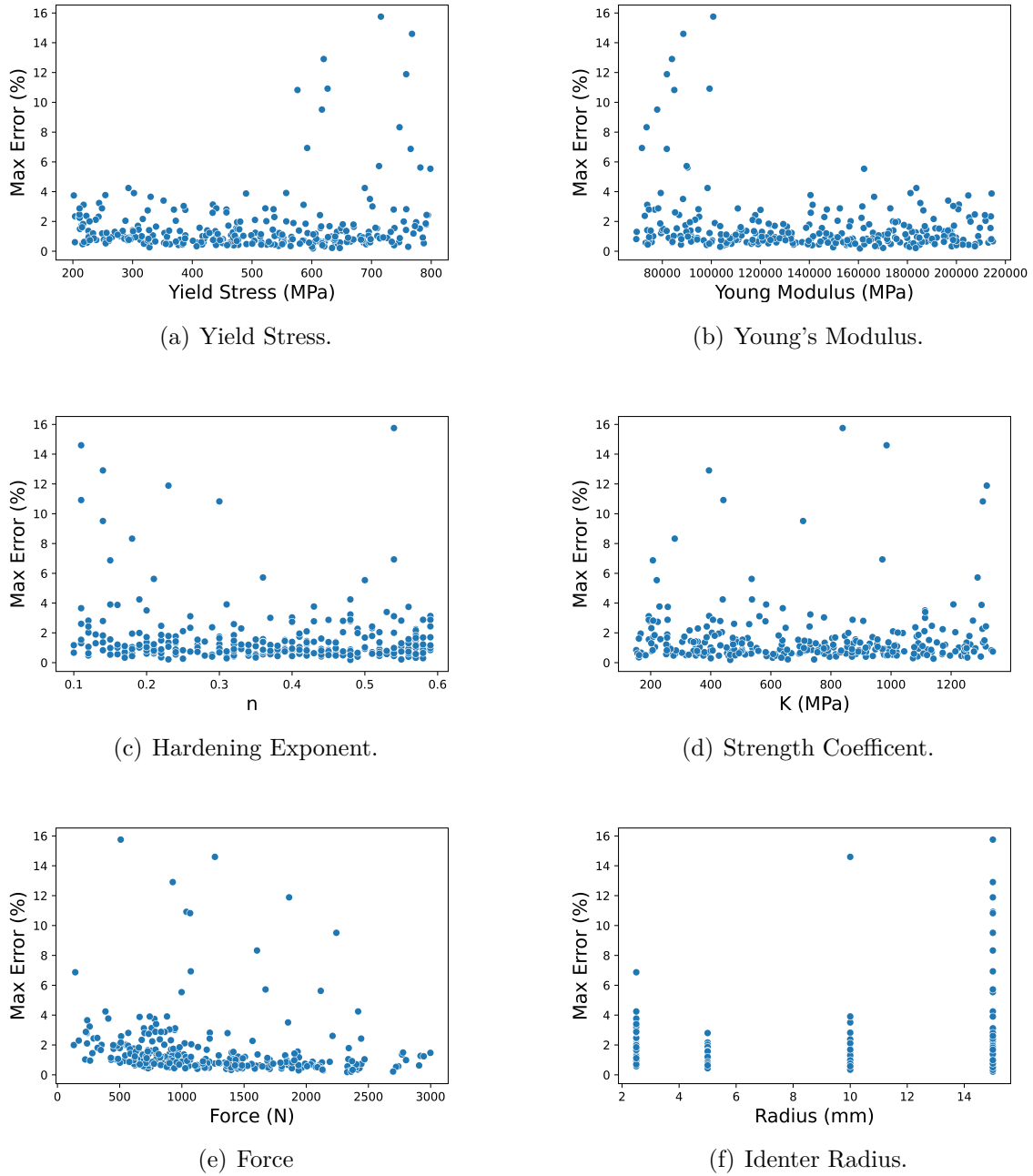
Figure 6.26: Correlation between maximum percentage error and magnitude of the material parameter.

When evaluating the presence of any correlation between the occurrence of the largest errors with the considered parameters, it is verified that the largest errors occur in: (1) high magnitudes of yield stress, (2) low magnitudes of Young's modulus and (3) high magnitudes of indenter radius. No correlations were identified in: (1) hardening exponent, (2) strength Coefficient, and (3) force.

In order to evaluate the performance of the proposed neural network, figure 6.27 presents

two predictions obtained, the worst prediction is shown on the left and the best prediction on the right. As it is possible to identify, for the best prediction, there are almost no differences between the target and the predicted curve, both overlap. For the worst predicted curve, the prediction of displacements greater than the target is verified for practically all ordered pairs. When evaluating other predictions made by the same ANN, it is identified that this is not a general rule, in other situations there is the prediction of displacements lower than the target.
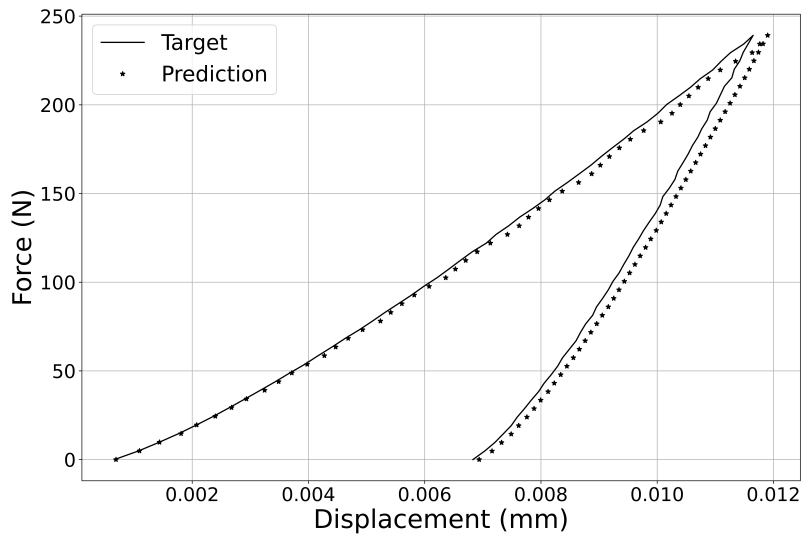
(a) Worst prediction.
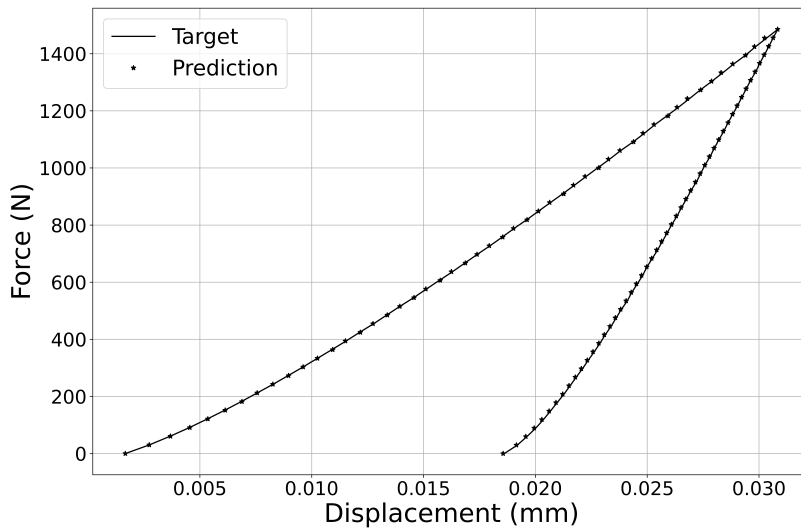
(b) Best prediction.

Figure 6.27: Displacement-force curve prediction for an indentation test using mechanical properties and boundary conditions.

From the displacement-force curve it is possible to obtain the residual and the maximum indentation (from these parameters it is possible to calculate the indentation area). Figure 6.28 shows a comparison of maximum and residual indentation between target and prediction for all predictions performed. An average error of 1.87% was found for the residual indentation predictions and 0.32% for the maximum indentation.

(a) Maximun indentation.
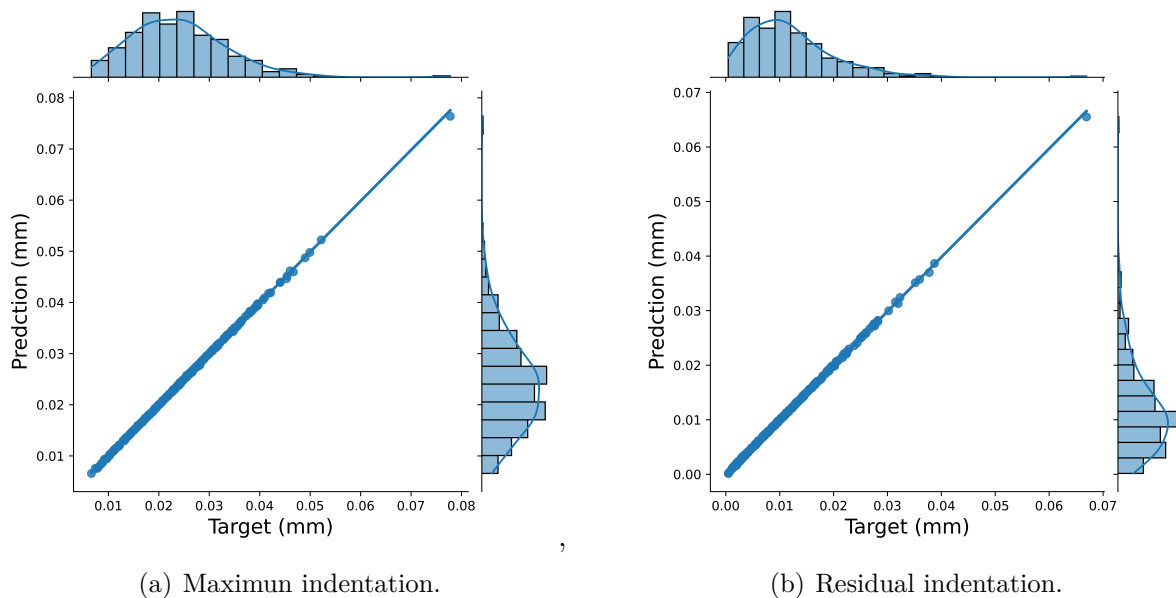
(b) Residual indentation.

Figure 6.28: Comparative view between prediction and target.

The general mean error of predictions for the displacement-force curve was 0.42%, i.e., the performance of the adopted neural network presents good accuracy when compared to the results obtained via FEM. The neural network adopted for predicting the displacement-force curve based on material properties and boundary conditions provides better performance, even covering more variables, than the neural network for predicting the stress-strain curve. It should be noted that the same neural network and the same dataset adopted for the prediction of the displacement-force curve were tested for the prediction of the stress-strain curve, with some adjustments, but the performance was not superior to the networks presented in item 6.1.1. In general, the results presented in this item make it clear that the use of ANN to predict the displacement-force curve based on material properties and boundary conditions for the study of residual indentation presents itself as a viable and powerful alternative to FEM.

Finally, the same neural network layout adopted for predicting the displacement-force curve was used to predict the contact pressure. The comparison between the predictions and the target is shown in figure 6.29. For such predictions, a mean error equal to 0.38% and a maximum error equal to 3.51% was obtained.
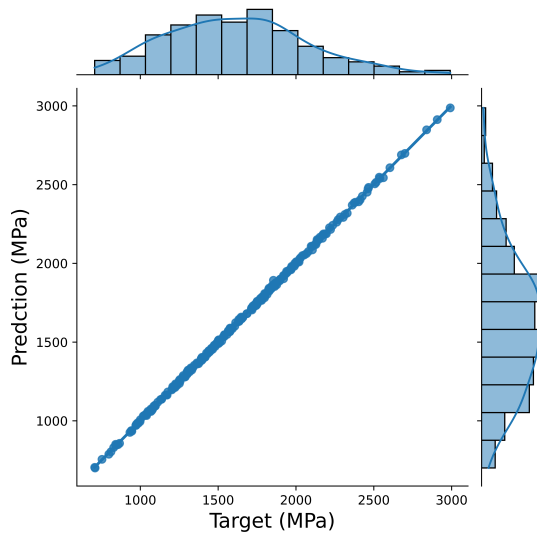
Figure 6.29: Comparative view between prediction and target for contact pressure.

6.2 Conclusion

The goal of this work, as previously stated, is to identify the possibility of using Neural Networks to predict the behavior and properties of metallic and polymeric material (rigid thermoplastic polymers) under inelastic strains. In order to validate the applicability of neural networks for this purpose, four different applications were evaluated.

Two evaluations were performed for the study in rigid thermoplastic polymers: (1) prediction of the material parameters of the proposed rheological model (modified Mulliken-Boyce model) from stress-strain curves obtained through experimental and/or numerical tests, and (2) prediction of the stress-strain curve from material properties. The first evaluation verifies the applicability of neural networks in assisting with the numerical calibration procedure of constitutive models, which can be time-consuming. The second evaluation determines the suitability of neural networks for predicting material behavior (stress-strain curve) based on material properties. Once such applicability is identified, the use of neural networks can help or even replace commonly used numerical tools, such as the FEM.

The best predictions for the first evaluation case, predicting material parameters from the stress-strain curve, occurred for E_1, S_{ss}, M_i, and ΔG_1. Lower prediction accuracy was obtained for J_m and h_1. Four evaluations were performed to determine the impact of material parameter predictions on the description of the stress-strain curve: PC, PC/ABS 60:40, PC/ABS 80:20, and ABS. The results obtained show good performance, the worst adaptation occurred for the ABS, where the r^2 was equal to 0.97.

The results of the second case studied, predicting the stress-strain curve from material properties, were also satisfactory. The mean error and maximum error in the predictions

of the stress-strain curve were 3.82% and 9.05%, respectively. The largest errors occurred primarily when low magnitudes of ΔG_1 were considered.

In summary, when evaluating the results obtained for the evaluation of rigid thermoplastic polymers, it is possible to state that the use of neural networks is a viable tool for predicting the material properties of the adopted constitutive model as well as the material's behavior. Once the database is created, predictions can be made in a matter of seconds, much less time than it takes to run a simulation in the commercial software ABAQUS® using VUMAT (approximately 6 hours on the same machine).

Two evaluations were performed for the metals study: (1) prediction of the stress-strain curve from the displacement-force curve and (2) prediction of the displacement-force curve and contact pressure from the material properties. The first hypothesis evaluates the applicability of neural networks for the identification of material behavior, in this case the stress-strain curve, from the displacement-force curve typically obtained through experimental indentation tests (the stress-strain curve is not a generated output for such testing). The second hypothesis identifies the ability of neural networks to assist or even replace commonly used numerical tools, such as the FEM, for such applications.

For the first case, it was identified that, the observed results revealed that the number of variables and the ML strategy adopt for the training have a significant impact in an ANN prediction. the ANN-A (a model with fully variable material properties, compression force and indenter radius) has shown an overall precise representation of the expected (target) stress-strain relationship, but with an occasional high error. From this observation, a model (ANN-B) trained using a dataset with a constant compressive force is also analyzed. In this case, better predictions are identified when compared to the ANN-A model, however, the relatively high errors in some predictions remained. The ANN-C model, implemented considering only variations in the material properties, show significant improvements in the predictions, but, when evaluating the behavior of the predictions, it was found that the strength coefficient has the greatest influence on the errors observed. This led to the understanding that possibly a model to predict the stress-strain curve for the entire range of metallic material it is not the most effective solution. A segregation of the strength coefficient in smaller subsets for the training of the ANN-D produced the lowest mean errors (approx. 2.5%) and a mitigation of the maximum error. Moreover, this strategy does not really require a large dataset for training the neural networks considered. The amount of data used for each of the neural networks used (pertaining to each strength coefficient range) was approximately 80% lower than that used for the others, but even so, with good accuracy.

The second case, prediction of the displacement-force curve, showed better accuracy in predictions when compared to predictions of the stress-strain curve, with a mean error of about 1.7%. The maximum error obtained was 16%, but large errors in predictions were

exceptions. When the residual indentation is evaluated, a parameter that allows obtaining the dimensions of the indentation marks, the errors obtained by the predictions are even smaller (maximum error equal to 1.87% mean 0.32%). The maximum contact pressure predictions are also accurate, with an average and maximum error of 0.38% and 3.51%, respectively.

The results of the second study show that the use of neural networks provides satisfactory performance. The prediction errors are significantly low in all cases evaluated, and the results obtained allow inference that the use of neural networks is a suitable method for studying the behavior of metals under the conditions considered.

Both the polymer and metal results show that the use of neural networks is a powerful tool for that can be used to predict the mechanical behavior of solids. Such a tool can be used as an auxiliary tool or even as a substitute method for well-established numerical and/or experimental methods. The only requirement, however, is to have a dataset beforehand so that the training and construction of the networks can be carried out.

Chapter 7

Future Works

As demonstrated throughout this work, the use of neural networks to predict the material behavior for the study of rigid thermoplastic polymers under uniaxial compression and the study of residual indentation in metals produced good results. Thus, the primary goal is to apply the same methodology presented and used for the study of indentation in polymers.

Initial studies were started, in which the modified Mulliken-Boyce model was used to evaluate indentation in polymers. The first evaluations were carried out for ABS and it was identified that the adopted model was able to accurately reproduce the mechanical behavior of the material (the values obtained numerically were very close to the experimental ones). In the case of PC, the model generally reproduces the experimental results, but not as well as in the case of ABS. As the magnitude of force increases, the model's accuracy decreases, and the error can reach approximately 50% of the average of the experimental results.

Preliminary results show that the modified Mulliken-Boyce model is a viable model for studying indentation in polymers and it is expected that the methodology adopted for metals can also be applied to polymers with good prediction accuracy. In this way, the continuation of this study takes place as follows:

1. Implementation of a 2D model in FEM, in order to reduce computational costs;

2. Check the validity of applying the Modified Mulliken-Boyce model in a two-dimensional configuration for the study of indentation in polymeric materials through experimental tests (the VUMAT algorithm developed in this thesis can be applied to two-dimensional evaluations);

3. Creation of a database (input and output) through the FE model;

4. Application of the methodology adopted in this thesis through Neural Networks for the prediction of the desired parameters for residual indentation tests in polymeric

materials.

References

[1] R.K. Al-Rub, A.H Tehrani, and M.K. Darabi. constitutive model to polymers and their composites application of a large deformation nonlinear-viscoelastic viscoplastic viscodamage. *International Journal of Damage Mechanics*, 0:1–47, 2014.

[2] R.K.A. Al-Rub and A. Tehrani. Viscodamage model for polymers and polymer composites. *52nd Structural Dynamics and Materials Conference*, 2011. doi: 10.2514/6. 2011-2173.

[3] G. Antoine and R. C Batra. Low speed impact of laminated polymethylmethacrylate/adhesive/polycarbonate plates. *Composite Structures*, 116:193–210, 2014. doi: 10.1016/j.compstruct.2014.04.006.

[4] E.A. Arruda and M.C. Boyce. A three-dimensional constitutive model for the large stretch behavior of rubber elastic materials. *Journal of the Mechanics and Physics of Solids*, 41:389–412, 1993. doi: 10.1016/0022-5096(93)90013-6.

[5] H. Baaser. The pade approximation for matrix exponentials applied to an integration algorithm preserving plastic incompressibility. *Computational Mechanics*, 2004.

[6] N. Belayachi, N. Benseddiq, and M. Nait-Abdelaziz. On cavitation and macroscopic behaviour of amorphous polymer-rubber blends. *SCIENCE AND TECHNOLOGY OF ADVANCEDMATERIALS*, 9, 2008. doi: 10.1088/1468-6996/9/2/025008.

[7] N. Belayachi, N. Benseddiq, M. Nait-Abdelaziz, and A. Hamdi. On cavitation and macroscopic behaviour of amorphous polymer-rubber blends. *Science and Technology of Advanced Materials*, 9, 2008.

[8] Y. Bengio, A. Courville, and P. Vincent. Representation learning: A review and new perspectives. *IEEE Transactions on Pattern Analysis and Machine Intelligence*, 35(8), 2013.

[9] J. Bergstrom. *Mechanics of Solid Polymers: Theory and Computational Modeling.* William Andrew, 2015.

[10] J.S. Bergstrom and M.C Boyce. Constitutive modeling of the large strain time-dependent behavior of elastomers. *Journal of the Mechanics and Physics of Solids*, 46:931–954, 1998. doi: 10.1016/S0022-5096(97)00075-6.

[11] J.S. Bergstrom, C.M Rimmac, and S.M. Kurtz. Prediction of multiaxial mechanical behavior for conventional and highly crosslinked uhmwpe using a hybrid constitutive model. *Biomaterials*, 24:1365–1380, 2003. doi: 10.1016/S0142-9612(02)00514-8.

[12] M.J Boussinesq. *Application des Potentiels à l'étude de l'équilibre et du mouvement des solides élastiques.* Gauthier-Villars, 1885.

[13] M.C. Boyce, E.M. Arruda, and R. Jayachandram. The large strain compression, tension, and simple shear of polycarbonate. *Polymer Engineering and Science*, 34, 1994. doi: doi.org/10.1002/pen.760340904.

[14] S. Canevarolo. *Ciencia dos Polimeros.* Artliber, 2010.

[15] D.S. Chadrasekharaiah and L. Debnath. *Continuum Mechanics.* Academic Press, 1943.

[16] E.W.V. Chaves. *Solving Problems by means of Continuum Mechanics.* University of Castilla - La Mancha, 2019.

[17] H. Chen and L. Cai. An elastic-plastic indentation model for different geometric indenters and its applications. *Materials Today Communications*, 2020.

[18] F. Chollet. *Deep Learning with Python.* Manning Publications Co., 2018.

[19] T. Doca. Numerical frameworks for the wear modelling of key engineering materials. In *Wear in Advanced Engineering Applications and Materials*, pages 71–91. World Scientific Publishing Co Pte Ltd, 2022.

[20] T. Doca, F.M. Loyola, and E.L. Albuquerque. Numerical frameworks for fretting fatigue life analysis: Modeling, validation and experimental comparison. *Theor Appl Fract Mech*, 121, 2022.

[21] Y. Duan, A. Saigal, R. Greif, and M.A. Zimmerman. A uniform phenomenological constitutive model for glassy and semicrystalline polymers. *Polymer Engineering and Science*, 41(8):1322–1328, 2001. doi: 10.1002/pen.10832.

[22] J. Furmanski, E.N. Brown, G.T. Gray, C. Trujillo, D.T. Martinez, S. Bilyk, and R. Becker. Extreme tensile damage and failure in glassy polymers via dynamic-tensile-extrusion. *Dynamic Behavior of Materials*, 1:107–112, 2013. doi: 10.1007/978-3-319-00771-7_13.

[23] Z. George and Y. Mohammadreza. *Size Effects in Plasticity.* Elsevier Inc., 2020.

[24] A. Geron. *Hands-On Machine Learning with Scikit-Learn and TensorFlow: Concepts, tools, and techniques to buid intelligent systems.* O'Reilly Media, 2017.

[25] A. Gianfrancesco. *Materials for Ultra-Supercritical and Advanced Ultra-Supercritical Power Plants.* Woodhead Publishing, 2017.

[26] I. Goodfellow, Y. Bengio, and A. Courville. *Deep Learning.* MIT Press, 2016. `http://www.deeplearningbook.org`.

[27] C. G'Sell and J.J Jonas. Yield and transient effects during the plastic deformation od solid polymers. *Journal of Materials Science*, 16:1956–1974, 1981.

[28] G. Gu, C. Chen, and M. Buehler. De novo composite design based on machine learning algorithm. *Extreme Mechanics Letters*, 18, 2017.

[29] H. Hencky. The law of elasticity for isotropic and quasi-isotropic substances by finite deformations. *J. Rheology*, 2:169–176, 1931.

[30] H. Hertz. Über die berührung fester elastischer körper (on contact between elastic bodies). *Journal für die Reine und Angewandte Mathematik*, 29: 156–171, 1882.

[31] C.O Horgan and G. Saccomandi. Constitutive modelling of rubber-like and biological materials with limiting chain extensibility. *Mathematics and Mechanics of Solids*, 7: 353–371, 2002. doi: 10.1177/108128028477.

[32] F. Irgens. *Continuum Mechanics.* Springer, 2008.

[33] K. Jeong, H. Lee, O. Kwon, J. Jung, D. Kwon, and H. Han. Prediction of uniaxial tensile flow using finite element-based indentation and optimized artificial neural networks. *Materials and Design*, 196, 2020.

[34] S.K. Jeong and H.M Anastasia. A time-integration method for the viscoelastic-viscoplastic analyses of polymers and finite element implementation. *International Journal for Numerical Methods in Engineering*, 79:550–575, 2009. doi: doi.org/10.1002/nme.2569.

[35] J. Johnsen, A.H. Clausen, and A. Benallal. A thermo-elasto-viscoplastic constitutive model for polymers. *Journal of the Mechanics and Physics of Solids*, 124:681–701, 2019. doi: 10.1016/j.jmps.2018.11.018.

[36] K. L. Johnson. *Contact Mechanics.* Cambridge University Press, 1985.

[37] B. Jordan, M. Gorji, and D. Mohr. Neural network model describing the temperature and rate-depedent stress-strain response of polypropylene. *International Journal of Plasticity*, 135, 2020.

[38] J.L. Jordan, J.R. Foley, and C.R. Siviour. Mechanical properties of epon 826/dea epoxy. *Mechanics of Time-Dependent Materials*, 12:249–272, 2008. doi: 0.1007/s11043-008-9061-x.

[39] M. Kaliske and G. Heinrich. An extended tube-model for rubber elasticity: Statistical-mechanical theory and finite element implementation. *Rubber Chemistry and Technology*, 72(4):602–632, 1999. doi: 10.5254/1.3538822.

[40] G. Kermouche, N. Aleksy, and J.M. Bergheau. Viscoelastic-viscoplastic modelling of the scratch response of pmma. *Advances in Materials Science and Engineering*, 2013, 2013. doi: 10.1155/2013/289698.

[41] D. Kingma and J. Ba. Adam: A method for stochastic optimization. *Proceedings of the 3rd International Conference on Learning Representations*, 2014.

[42] E. Kroner. Allgemeine kontinuumstheorie der versetzungen und eigenspannungen. *Archive for Rational Mechanics and Analysis*, 4, 1959.

[43] J. Kudela and R. Matousek. Recent advances and applications of surrogate models for finite element method computations: a review. *Application of soft computing*, 2022.

[44] W. Kuhn and F. Grun. Beziehungen zwischen elastischen konstanten und dehnungs-doppelbrechung hochelastischer stoffe. *Kolloid-Zeitschrift*, 1942.

[45] E. Lee. Elastic plastic deformation at finite strain. *Journal of Applied Mechanics*, 54, 1969.

[46] L. Lu, M. Dao, P. Kumar, U. Ramamurty, G. Farniadakis, and S. Suresh. Extraction of mechanical properties of materials through deep learning from instrumented indentation. *Proceedings of the National Academy of Sciences*, 13, 2020.

[47] A. Mangal. Applied machine learning to predict stress hotspots in materials, 2018.

[48] H.T. Mase, R.E. Smelser, and G. E. Mase. *Continuum Mechanics for Enginners*. Taylor and Francis Group, 2009.

[49] N. Mccrum, Buckley C., and C. Bucknall. *Principle of Polymer Engineering*. Oxford University Press, 1988.

[50] Y. Miyazawa, F. Briffod, T. Shiraiwa, and M. Enoki. Prediction of cyclic stress-strain property od steels by crystal plasticity simulations and machine learning. *Materials*, 12, 2019.

[51] A.D. Mulliken and M.C. Boyce. Mechanics of the rate-dependent elastic-plastic deformation of glassy polymers from low to high strain rates. *International Journal of Solids and Structures*, 43:1331–1356, 2006. doi: 10.1016/j.ijsolstr.2005.04.016.

[52] E.A.S. Neto, D. Teric, and D.R.J. Owen. *Computational Methods for Plasticity.* John Wiley and Sons, 2008.

[53] V.D Nguyen, F. Lani, T. Pardoen, X.P. Morelle, and L. Noels. A large strain hyperelastic viscoelastic-viscoplastic-damage constitutive model based on a multi-mechanism non-local damage continuum for amorphous glassy polymers. *International Journal of Solids and Structures*, 96:192–216, 2016. doi: 10.1016/j.ijsolstr.2016.06.008.

[54] R.W Ogden. *Non-linear Elastic Deformations.* John Wiley and Sons Ltd., 1985. doi: 10.1002/zamm.19850650903.

[55] T. Padim, T. Doca, A.R. Figueiredo, and F.M. Andrade Pires. Torsional fretting wear experimental analysis of a r3 offshore steel against a pc/abs blend, 2019.

[56] G. Peng, F. Xu, J. Chen, H. Wang, J. Hu, and T. Zhang. Evaluation of non-equibiaxial residual stresses in metallic materials via instrumented spherical indentation. *Metals - Open Access Metallurgy Journal*, 10(4):440–457, 2020.

[57] P. Perzyna. Fundamental problems in viscoplasticity. *Advances in Applied Mechanics*, 9:243–377, 1966.

[58] T. Pham and S. Kim. Determination of equi-biaxial residual stress and plastic properties in structural steel using instrumented indentation. *Materials Science and Engineering*, 688:352–363, 2017.

[59] M. Polanco-Loria, A.H. Clausen, T. Berstad, and O.S. Hopperstad. Constitutive model for thermoplastics with structural applications. *International Journal of Impact Engineering*, 37:1207–1219, 2010. doi: 10.1016/j.ijimpeng.2010.06.006.

[60] K.H. Safari, J. Zamani, R.M. Guedes, and F.J. Ferreira. The effect of heat developed during high strain rate deformation on the constitutive modeling of amorphous polymers. *Mechanics of Time-Dependent Materials*, 20:45–64, 2016. doi: 10.1007/s11043-015-9283-7.

[61] S. Sarva, A.D. Mulliken, and M.C. Boyce. Mechanics of taylor impact testing of polycarbonate. *International Journal of Solids and Structures*, 44:2381–2400, 2007.

[62] J.C Simo and T.J.R Hughes. *Computational Inelasticity.* Springer, 1997.

[63] D. K. Singh. *Strength of Materials.* CRC Press; 3rd edition, 2021.

[64] P. Smith. *The Fundamental od Piping Design.* Gulf Publishing Company, 2007.

[65] C. Suchocki. An internal-state-variable based viscoelastic-plastic model for polymers. *Journal of Theoretical and Applied Mechanics*, 53(3):593–604, 2015. doi: 10.15632/jtam-pl.53.3.593.

[66] F. Sun and E.K. Gamstedt. Experimental and numerical investigation on shear banding during nanomachining of an amorphous glassy polymer. *International Journal of Mechanical Sciences*, 151:13–21, 2019. doi: 10.1016/j.ijmecsci.2018.11.004.

[67] D. Tkalich, M. Fourmeau, A. Kane, C.C. Li, and G. Cailletaud. Experimental and numerical study of kuru granite under confined compression and indentation. *International Journal of Rock Mechanics and Mining Sciences*, 87:55–68, 2016. doi: 10.1016/j.ijrmms.2016.05.012.

[68] I. Tomas, A.P. Cisilino, and P.M. Frontini. Accurate, efficient and robust explicit and implicit integration schemes for the arruda-boyce vicoplastic model. *Mecanica Computacional*, 27:1003–1042, 2008.

[69] I. Tomas, A.P. Cisilino, and P.M. Frontini. An implicit implementation of the arruda-boyce viscoplastic model. *Revista Internacional de Metodos Numericos para Calculo y Diseno de Ingeniaria*, 31, 2015. doi: 10.1016/j.rimni.2014.06.001.

[70] J.P. Torres and P.M. Frontini. Mechanics of polycarbonate in biaxial impact loading. *Journal of Solids and Structures*, 85-86:125–133, 2016. doi: 10.1016/j.ijsolstr.2016.02.010.

[71] L. Treloar. The elasticity of a network of long-chain molecules. *Transactions of the Faraday Society*, 1946.

[72] A. Trivedi and C. Siviour. Predicting the high strain rate response of plasticised poly(vinyl chloride) using a fractional derivative model. *12th International Conference on the Mechanical and Physical Behaviour of Materials under Dynamic Loading*, 183, 2018. doi: 10.1051/epjconf/201818301013.

[73] C. Truesdell and W. Noll. *The nonlinear field theories of mechanics.* Springer, 1965.

[74] A.G Varghese and R.C. Batra. Constitutive equations for thermomechanical deformations of glassy polymers. *International Journal of Solids and Structures*, 46:4079–4094, 2009.

[75] T. Vergard. Implementantion of arruda-boyce material model for polymers in abaqus, 2014.

[76] H. Wang, Y. Zhang, H. Zhou, and Z. Huang. Constitutive modelling of polycarbonate at low, moderate and high strain rates. *Conference: Materials Science and Engineering*, 187, 2017. doi: 10.1088/1757-899X/187/1/012023.

[77] H. Wang, Y. Zhang, Z. Huang, Z. Tang, Y. Wang, and H. Zhou. Establishment and comparison of four constitutive relationships of pc/abs from low to high uniaxial

strain rates. *Mechanics of Time-Dependent Materials*, 22:457–481, 2018. doi: 10.1007/s11043-017-9367-7.

[78] M. Wang and E. Guth. statistical theory od networks of non-gaussian flexible chains. *The Journal of Chemical Physics*, 1952.

[79] M. Wang, J. Wu, Y. Hui, Z. Zhang, X Zhan, and R. Guo. Identification of elastic-plastic properties of metal materials by using the residual imprint of spherical indentation. *Materials Science and Engineering*, 679:143–154, 2017.

[80] Z. Wang, L. Deng, and J. Zhao. Estimation of residual stress of metal material without plastic plateau by using continuous spherical indentation. *International Journal of Pressure Vessels and Piping*, 172:373–378, 2019.

[81] J. Weng, R. Lindvall, K. Zhuang, J. Stahl, H. Ding, and J. Zhou. A machine learning based approach for determining the stress-strain raltion of grey cast iron from nanoindentation. *Mechanical of Materials*, 148, 2020.

[82] H. Xiao and L.S Chen. Hencky's elasticity model and linear stress-strain relations in isotropic finite hyperelasticity. *Acta Mechanica*, 157:51–60, 2002.

[83] C. Yang, Y. Kim, S. Ryu, and G. Gu. Prediction of composite microstructure stress-strain curves using convolutional neural networks. *Materials and Desing*, 189, 2020.

[84] S. Zhong, K. Zhang, M. Bagheri, A. Gu, and B. Li. Machine learning: New ideas and tools in environmental science and engineering. *Environmental Science and Technology*, 2021.

[85] N. Zobeiry, J. Reiner, and R. Vaziri. Theory-guided machine learning for damage characterization of composites. *Composite Structures*, 246, 2020.

119